

國立交通大學
光電工程學系暨研究所
博士論文

實驗及理論探討奈米結構之氧化鋅光學性質研究

Experimental and theoretical study on the
influence of finite crystallize optical
properties in ZnO nanostructures



研究生：林國峰

指導教授：謝文峰 教授

中華民國九十七年十月

實驗及理論探討奈米結構之氧化鋅光學性質研究

Experimental and theoretical study on the influence of finite crystallize optical properties in ZnO nanostructures

研究生：林國峰

Student : Kuo-Feng Lin

指導教授：謝文峰教授

Advisor : Dr. Wen-Feng Hsieh



A Dissertation

Submitted to Department of Photonics and Institute of Electro-Optical Engineering

College of Electrical Engineering and Computer Science

National Chiao Tung University

In Partial Fulfillment of the Requirements

for the Degree of

Doctor of Philosophy

in

Electro-Optical Engineering

October 2008

Hsinchu, Taiwan, Republic of China

中華民國九十七年十月

國立交通大學

論文口試委員會審定書

本校光電工程研究所博士班 林國峰 君

所提論文 實驗及理論探討奈米結構之氧化鋅光學性質研究

合於博士資格標準、業經本委員會評審認可。

口試委員：王興宗

張振雄

果尚志

彭仰璋

周武瑋

指導教授：謝文峰

所長：張振雄 教授

系主任：黃中堯 教授

Institute of Electro-Optical Engineering
National Chiao Tung University
Hsinchu, Taiwan, R.O.C.

Date : 2008/10/20

We have carefully read the dissertation entitled Experimental and theoretical study on the influence of finite crystallize optical properties in ZnO nanostructures

submitted by Kuo-Feng Lin in partial fulfillment of the requirements of the degree of DOCTOR OF PHILOSOPHY and recommend its acceptance.

Shyng Wang

C. S. Chang

Way-Bo Pong

Shyng Wang

Wu-ching chon

Wen-Jeng Hsieh

Thesis Advisor :

Director of Institute of Electro-Optical Engineering :

Chang, Chen-Shian

Chairman of Department of Photonics :

Tung Y. Iduang

誌謝

時間的流逝真是快速，轉眼間我即將離開這個具有充滿回憶的地方。回想過去這幾年，在我腦海裡不斷的浮現出我所經歷的人事物，感覺到所有一切的事都才剛剛發生而已，沒想到我即將要畢業了要進入我人生的另一段旅程了。

學習的過程是痛苦的，但是學習結果是甜美的。在這幾年裡，我特別要感謝的指導老師謝文峰教授在我課業、實驗以及待人處世上的指導及教誨，以及實驗室的學長們的指導使得我在學習過程中可以輕鬆自在。在我印象中，老師對教導學生相當的具有有耐心，並且訓練學生養成具有邏輯思考的處事能力。在我的感覺上老師就像是一位大家的好老爹!!!（雖然我曾被老爹定在黑板上近 2h 左右）他總是跟我們這群調皮的學生聊一些天南地北的事情。另外，我要感謝口試委員們對於論文上的指導及建議，使得論文更佳完整與周詳。在來要感謝雷射診斷實驗室裡曾經陪伴我走過這幾年以來的夥伴們。政哥、信民學長當初在實驗上的指導，也要感謝黃董、維仁、楊松精神及技術性上的指導。還有實驗室內可愛的學弟妹們，使得我在這幾年內的生活多采多姿，真是太感謝你們了。還有那些曾經跟我共存亡的同儕們，我們是共同經歷生死關卡的好同學、好朋友。在此我祝福你們鵬程萬里、事事如意。

最後我要感謝我的父母親偉大的奉獻與支持，使得我在求學的路程中可以無後顧之憂。還有感謝在我背後支持我的”那個人”，謝謝你一直在我的背後這麼的支持我!!!

實驗及理論探討奈米結構之氧化鋅光學性質研究

研究生：林國峰

指導教授：謝文峰 教授

國立交通大學光電工程學系暨研究所

摘要

我們運用實驗及理論探討在有限結構下的氧化鋅的光學性質特性。首先在實驗部份，我們利用溶膠-凝膠法製備氧化鋅量子點，由拉曼散射與光激發光實驗研究氧化鋅量子點的晶格動力學、激子相關特性在不同量子點尺寸的變化情形。我們藉由高解析度穿透顯微鏡與 X-光繞射估計在調配不同溶液濃度下的氧化鋅奈米晶粒尺寸。而在具有量子尺寸的材料中，電子與電洞的交互影響會隨著尺寸變小變得越顯著；而電子與聲子的耦合作用亦會隨著尺寸而變化。在拉曼光譜中，我們發現隨著氧化鋅奈米晶粒尺寸變小 E₂ (high) mode 有明顯的紅位移與不對稱光譜，再由 modified spatial correlation model 探討在不同奈米晶粒尺寸下的拉曼光譜隨尺寸變化的形為；而此理論模型概念考慮聲子受到奈米晶粒的邊界與尺寸分布的影響。我們發現在拉曼光譜的紅位移與不對稱光譜都是來自於 optical phonon 在空間中被局限所造成的結果。經由共振拉曼量測，發現電子與聲子耦合作用亦隨著奈米晶粒尺寸變小而有減緩的趨勢，而其中 Fröhlich

interaction 在電子與聲子交互作用中具有決定性的影響能力。另外，在光吸收光譜與光激發光譜中發現氧化鋅奈米晶粒有明顯的藍位移現象，再利用有效質量模型可粗略估計其量子侷限效應在不同氧化鋅奈米晶粒尺寸下的結果。經由低溫光激發光譜探討激子束縛能、激子與縱模聲子的耦合作用在氧化鋅量子點下所受到的影響，我們發現隨著氧化鋅量子點變小直接影響到激子波爾半徑變小而使得激子的極化現象變弱，進而導致激子與縱模聲子的 Fröhlich interaction 作用能力變小。經由上面的實驗，有效質量模型雖可以初步斷定光譜的藍位移現象來自於量子侷限效應；而有效質量模型在量子點尺寸越小時，過分地計算晶體週遭的位能，而且也無法得知在具有量子尺寸下詳細的電子行為。因此，我們利用 sp^3 緊束縛理論計算氧化鋅在奈米尺寸下的電子結構與其表面能量。

首先，我們計算氧化鎂鋅在不同鎂含量下的電子結構與電子態密度。發現隨著鎂含量變高能隙寬度與電子有效質量皆會有效的提升，這現象與實驗量測到得趨勢相當吻合。由電子態密度計算結果發現額外鎂的 $3s$ 與 $3p$ 電子軌域造成陽離子間波函數耦合作用增加，使得電子有效質量變大。另外，我們亦由計算電子軌域的波函數權重發現氧原子的 $2p$ 電子軌域侷限在氧原子的現象趨緩，因此減弱了氧原子本身的負電性；而陽離子電子軌域的波函數則有輕微的侷限現象產生。最後，我們利用 sp^3 緊束縛理論計算氧化鋅在奈米尺寸下延著極化面 $\langle 0001 \rangle$ 與非極化面 $\langle 1-100 \rangle$ 的電子結構與其表面能量。在表面上的 dangling bonds 會在電子結構中形成各自的表面能帶，而其波函數有明顯侷限在表面的趨勢。另外，

延著 $\langle 1-100 \rangle$ 方向的非極化面，發現表面的 dangling bonds 的波函數會隨著尺寸變小而有增大的趨勢，進而導致其表面能帶的 energy splitting 增大。在我們的計算當中亦發覺到延著極化面的量子侷限效應比其他方向較為明顯。



Experimental and theoretical study on the influence of finite crystallize optical properties in ZnO nanostructures

Student: Kuo-Feng Lin

Advisor: Dr. Wen-Feng Hsieh

Department of Photonics & Institute of Electro-Optical Engineering

National Chiao Tung University



We studied optical properties in finite crystallize ZnO nanostructures with Experimental and theoretical method. In experimental part, ZnO quantum dots were successfully synthesized from 3.5 to 12 nm via a simple sol-gel method. The average size of quantum dots can be tailored using well-controlled concentration of zinc precursor. In the lattice dynamics, the measured Raman spectral shift and asymmetry for the E_2 (high) mode caused by localization of optical phonons agree well with that calculated by using the modified spatial correlation model. From the resonant Raman scattering, the coupling strength between electron and longitudinal optical phonon, deduced from the ratio of the second- to the first-order Raman

scattering intensity, diminishes with reducing the ZnO QD diameter. The size dependence of electron-phonon coupling is principally a result of the Fröhlich interaction. Size-dependent blue shifts of photoluminescence and absorption spectra revealed the quantum confinement effect. Additionally, the exciton-longitudinal-optical-phonon (LO-phonon) interaction was observed to decrease with reducing ZnO particle size to its exciton Bohr radius (a_B). The unapparent LO-phonon replicas of free exciton (FX) emission and the smaller FX energy difference between 13 and 300 K reveal decreasing weighting of exciton-LO phonon coupling strength. The diminished Fröhlich interaction mainly results from the reducing a_B with size due to the quantum confinement effect that makes the exciton less polar. According to the above experiment data, the effective-mass approximation apparently gives a good understanding of the blue shift of the optical absorption threshold. However, this approach fails for the smallest crystallite sizes because of the oversimplified description of the crystal potential as a spherical well of infinite depth. A better description of the band structure can be obtained from a tight-binding (TB) framework. Since the atomic structure is implicitly considered, this method is more adequate for small crystallites. In our theoretical part, we used sp^3 TB model to calculate the electronic structure and surface states in ZnO finite crystallize.

Firstly, calculating the electronic structure and the density of states in the wurtzite structure of $Zn_{1-x}Mg_xO$ (ZMO) alloys using sp^3 semi-empirical tight-binding model, we observed increases of both band gap and electron effective mass that agree with the experimental results as increasing Mg composition up to $x = 0.3$. From the calculated total density of states, the increasing electron effective mass is a result of localized orbital overlap of cation sites due to extra density of modes coming from Mg3s and Mg3p orbitals as introducing more Mg composition. Additionally, reducing electronegative characteristic of oxygen was caused by the O2p was less localized around the oxygen atom. Finally, the electronic band structures and surface states were investigated for ZnO finite wells or slabs grown along $\langle 0001 \rangle$ and $\langle 1-100 \rangle$ directions using tight binding representation. The dangling bonds on two end-surfaces caused surface bands for different directions grown slabs, of which the wavefunctions tend to localize at the end surfaces. The increasing splitting of the degenerate surface bands at the Γ point was observed decreasing with the thickness of the nonpolar $[1-100]$ slab. And, we also found that the enhancing the band gap along $[0001]$ polar due to more effective carrier confinement in c-axis.

Contents

Abstract in Chinese.....	I
Abstract in English	IV
Contents.....	VI
List of Figures.....	IX
List of Tables.....	XII
Chapter 1 Introduction.....	1
1.1 Significance of the dissertation.....	1
1.2 Basic properties of ZnO and general review of ZnO nanostructure.....	2
1.3 Motivations.....	7
1.4 Organization of the dissertation.....	9
References.....	10
Chapter 2 Theoretical background.....	15
2.1 Crystal structures and Lattice dynamics.....	15
2.2 Excitons-related emissions.....	26
2.3 Quantum size effect.....	39
2.4 Tight Binding Method.....	45
References.....	53
Chapter 3 Experiment detail and analysis techniques.....	58
3.1 Experiment detail.....	58
3.2 Microstructure and lattice dynamics analysis.....	65

3.3 Characterization of optical properties.....	68
References.....	71
Chapter 4 Crystal structures and Lattice dynamics in ZnO quantum dots.....	72
4.1 Morphology and crystal structures.....	74
4.2 Spatial confinement of optical phonon in ZnO quantum dots.....	77
4.3 Electron-phonon coupling in ZnO quantum dots.....	82
4.4 Summary.....	86
References.....	88
Chapter 5 Reducing exciton-longitudinal-optical phonon interaction with shrinking ZnO quantum dots.....	91
5.1 Band gap variation of size-controlled ZnO quantum dots.....	92
5.2 Exciton-longitudinal phonon interaction with shrinking ZnO quantum dots.....	97
5.3 Summary.....	103
References.....	106
Chapter 6 Calculations of electronic structure and density of states in the wurtzite structure of Zn_{1-x}Mg_xO alloys using <i>sp</i>³ semi-empirical tight-binding model.....	109
6.1 Theoretical details.....	111
6.2 Band structures of Zn _{1-x} Mg _x O.....	112
6.3 Energy gaps and effective masses.....	114
6.4 Density of states.....	117
6.5 Summary.....	120
References.....	121

Chapter 7 Electronic band structures and surface states of ZnO finite well structures.....	124
7.1 Computation method details and parameters.....	126
7.2 Transfer matrix technique and surface states.....	131
7.3 Surface states of nanowire with identical lateral facets.....	136
7.4 Band structures for $\langle 0001 \rangle$ and $\langle 1-100 \rangle$ directions.....	140
7.5 Wave function and quantum effect for ZnO finite well.....	143
7.6 Summary.....	147
References.....	149
 Chapter 8 Conclusions and Prospective.....	 152
8.1 Conclusions.....	152
8.2 Prospective.....	154
 Resume	
 Publication list	



List of Figures

Fig. 1-1 The wurtzite structure model of ZnO.....	4
Fig. 1.2 Representative scanning electron microscopy images of various ZnO nanostructure morphologies.....	6
Fig. 2-1 Stick and ball representation of ZnO crystal structures.....	16
Fig. 2-2 Schematic representation of a wurtzitic ZnO structure.....	17
Fig. 2-3 Phonon dispersion curves for ZnO crystal of wurtzite structure.....	24
Fig. 2-4 Displacement vectors of the phonon modes in ZnO wurtzite structure.....	25
Fig. 2-5 Bound-excitonic region of the 10 K PL spectrum for the forming gas annealed ZnO substrate.....	27
Fig. 2-6 Room-temperature PL spectra of various nanostructures in the UV range.....	33
Fig. 2-7 Illustration of the calculated defect energy levels in ZnO.....	35
Fig. 2-8 Room-temperature PL spectra of different nanostructures.....	36
Fig. 2-9 Hexagonal close-packed structure and the reciprocal lattice.....	46
Fig. 2-10 Inter-atomic matrix elements.....	52
Fig. 3-1 Schematic of the routes that one could follow within the scope of sol-gel processing.....	60
Fig. 3-2 XRD ω - 2θ scans geometry for ZnO nanoparticles.....	65
Fig. 3-3 Raman detection systems.....	68
Fig. 3-4 PL detection systems.....	69
Fig. 3-5 Optical absorption systems.....	70
Fig. 4-1 HRTEM image and size distribution.....	75
Fig. 4-2 XRD profiles of the ZnO QDs.....	76

Fig. 4-3 Typical Raman spectra of different sizes of ZnO QDs.....	77
Fig. 4-4 Fitting of the modified spatial correlation model.....	80
Fig. 4-5 Raman shift and asymmetric broadening of E_2 (high) phonon.....	81
Fig. 4-6 Resonant Raman scatterings of ZnO QDs.....	83
Fig. 4-7 Ratio between the second- and the first-order Raman scattering cross section as a function of ZnO diameter.....	85
Fig. 5-1 PL and absorption spectra near the band edge of various ZnO QD size.....	92
Fig. 5-2 Room temperature PL spectra of ZnO QDs with various sizes.....	94
Fig. 5-3 PL spectra of ZnO QDs as a function of excitation laser intensity.....	95
Fig. 5-4 The dependence of the band gap enlargement versus the ZnO QDs diameter as calculated from the effective mass model.....	96
Fig. 5-5 PL spectra of different ZnO particle sizes at 13K.....	98
Fig. 5-6 Temperature-dependence PL spectra of 7.4 nm of ZnO QDs.....	99
Fig. 5-7 Experimental and calculated exciton energies plotted against inverse temperature for different ZnO particle sizes.....	101
Fig. 5-8 The relation of $\alpha_{0\ QD}/\alpha_{0\ Powders}$ and $a_{B\ QD}/a_{B\ Powders}$ with different dot sizes.....	102
Fig. 6-1 Calculated band structure using semi-empirical tight-binding model.....	113
Fig. 6-2 The energy gaps of wurtzite $Zn_{1-x}Mg_xO$ alloys as a function of Mg.....	115
Fig. 6-3 Composition dependence of the electron effective masses.....	116
Fig. 6-4 Total density of states of various Mg concentrations in the wurtzite $Zn_{1-x}Mg_xO$ alloys.....	118
Fig. 7-1 Finite well structures of wurtzite material.....	128
Fig. 7-2 Projected band structure of the ideal [0001] and [000-1] surfaces of ZnO.....	133

Fig. 7-3 Projected band structure of the ideal surfaces [1-100] of ZnO.....	135
Fig. 7-4 Wurtzite nanowire with identical lateral facets wrapped by a cylinder of radius R equal to the radius of nanowire.....	137
Fig. 7-5 (Color online) Surface spectrum of GaN nanowire surrounded by identical [1-100] lateral facets.....	139
Fig. 7-6 The band structures of the ZnO slabs with five layers.....	142
Fig. 7-7 The wave functions of the six bands closest to the middle of the band gap away from Γ point for the slabs of two, five, and ten layers.....	144
Fig. 7-8 Variations of the band gap as a function of the well thickness.....	147



List of Tables

Table 2-1 Phonon mode frequencies of wurtzite ZnO.....	26
Table 3-1 Shows that chemical reagent was used with sol-gel experiment process.....	63
Table 3.2 A flow chart of fabricates ZnO quantum dots (QDS) by sol-gel method.....	64
Table 6-1 Anion-atom <i>p-orbitals</i> wave function for top valence band at Γ point.....	119
Table 6-2 Cation-atom <i>s-orbitals</i> wave function for lowest conduction band at Γ point.....	120
Table 7.1 Tight-binding parameters and lattice parameters for bulk ZnO.....	127



Chapter 1 Introduction

1.1 Significance of the dissertation

The synthesis of semiconductor nanomaterials has aroused worldwide interest in the last few years. Given their large surface area to volume ratios, size effects and possible quantum confinement effects, nanomaterials are predicted to exhibit new and enhanced properties relative to those of the corresponding bulk materials and offer routes to fabricating novel nanodevices. The wide band gap (3.4 eV at 5K), large exciton binding energy (60 meV), and radiation hardness of ZnO make it an excellent candidate UV light-emitter [1,2] for use in lasers, light-emitting diodes (LEDs), and other UV light-emitting devices. Under the right preparation conditions, pure excitonic emission from ZnO can be achieved, and UV lasing in bulk and nanowire ZnO have been observed. The size-tunable optical properties of quantum confined semiconductor nanocrystals have motivated further investigations into the luminescence of ZnO nanocrystals (quantum dots). The synthesis of other semiconductors as colloidal nanocrystals has opened up possibilities for their uses in many new applications. For example, CdSe quantum dots (QDs) have been prepared showing band-edge emission at a range of wavelengths in the visible with high quantum yields, given proper surface passivation. Strongly emitting CdSe QDs and related materials have been tested for use in biolabelings [50], in LEDs, or as quantum dot lasers [51]. ZnO is particularly attractive for similar applications because of the current interest in UV emitters, but the luminescence of colloidal ZnO QDs is usually dominated by visible emission from a trap state [52]. High UV emission quantum yields have not yet been observed in ZnO nanocrystals, limiting their potential

uses. In this dissertation, we fabricated high-quality ZnO QDs by a simple sol-gel method to solve above problem and discussed the optical features of crystal structures and lattice dynamics, Raman vibrational properties, and exciton-LO-phonon coupling in order to completely apply in photonic devices. Furthermore, we theoretically studied the influence of electronic behavior in ZnO finite structures using semi-empirical tight binding (SETB).

1.2 Basic properties of ZnO and general review of ZnO nanostructures

1.2.1 Basic properties of ZnO

Zinc oxide (ZnO) is a material with great potential for a variety of practical applications, such as piezoelectric transducers [53], optical waveguides [54], surface acoustic wave devices [55], varistors [56], phosphors [57], transparent conductive oxides [58], chemical and gas sensors [59], spin functional devices [60], and UV-light emitters [1,2]. The interest in ZnO is fueled and fanned by its prospects in optoelectronics applications owing to its direct wide band gap ($E_g \sim 3.3$ eV at 300 K). Some optoelectronic applications of ZnO overlap with that of GaN, another wide-gap semiconductor, which is widely used for production of green, blue-ultraviolet, and white light-emitting devices. However, ZnO has some advantages over GaN among which are the availability of fairly high-quality ZnO bulk single crystals and a large exciton binding energy (60 meV). ZnO also has much simpler crystal-growth technology, resulting in a potentially lower cost for ZnO-based devices. The basic materials parameters of ZnO were also shown in Table 1 [3]. To realize any type of device technology, these parameters were important to have control over the concentration of intentionally

introduced impurities (dopants), which are responsible for the electrical properties of ZnO. The dopants determine whether the current (and, ultimately, the information processed by the device) is carried by electrons or holes.

Table 1 Properties of wurtzite ZnO.	
Property	Value
Lattice parameters at 300 K:	
a_0	0.32495 nm
c_0	0.52069 nm
a_0/c_0	1.602 (1.633 for ideal hexagonal structure)
u	0.345
Density	5.606 g/cm ³
Stable phase at 300 K	wurtzite
Melting point	1975°C
Thermal conductivity	0.6, 1-1.2
Linear expansion coefficient (/°C)	a_0 : 6.5×10^{-6} , c_0 : 3.0×10^{-6}
Static dielectric constant	8.656
Refractive index	2.008, 2.029
Energy gap	3.4 eV (direct)
Intrinsic carrier concentration	$<10^6$ /cm ³
Exciton binding energy	60 meV
Electron effective mass	0.24
Electron Hall mobility at 300 K for low n -type conductivity	200 cm ² /V·s
Hole effective mass	0.59
Hole Hall mobility at 300 K for low p -type conductivity	5-50 cm ² /V·s

Wurtzite zinc oxide has a hexagonal structure (space group $C6mc$) with lattice parameters $a = 0.3296$ nm and $c = 0.52065$ nm. The structure of ZnO can be simply described as a number of alternating planes composed of tetrahedrally coordinated O^{2-} and Zn^{2+} ions, stacked alternately along the c -axis as shown in Fig. 1-1, in which a_1 , a_2 , and c are the unit vectors in a unit cell, the open and closed circles show the cation and

anion atoms, respectively. The tetrahedral coordination in ZnO results in non-central symmetric structure and consequently possesses piezoelectricity and pyroelectricity.

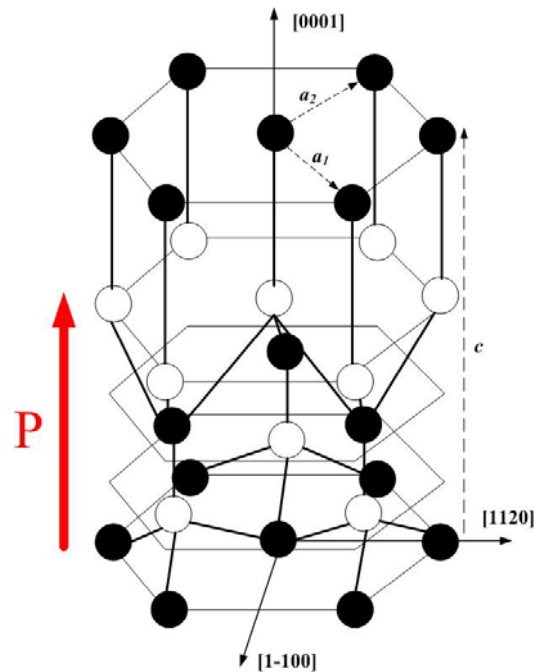


Fig. 1-1 The wurtzite structure model of ZnO.

Another important characteristic of ZnO is containing polar surfaces. The most common polar surface is the basal plane. The oppositely charged ions produce positively charged Zn-[0001] and negatively charged O-[000-1] surfaces, resulting in a normal dipole moment and spontaneous polarization along the c -axis as well as a divergence in surface energy. To maintain a stable structure, the polar surfaces generally have facets or exhibit massive surface reconstructions, but ZnO $\pm[0001]$ are exceptions: They are atomically flat, stable and without reconstruction [4, 5]. Efforts to understand the superior stability of the ZnO $\pm[0001]$ polar surfaces are at the forefront of research in today's surface physics [6-9]. The other two most commonly observed facets for ZnO are [1120] and [1-100], which are non-polar surfaces and have lower energy than the [0001] facets.

1.2.2 General review of ZnO nanostructures

Nanostructured ZnO materials have received broad attention due to their distinguished performance in electronics, optics and photonics. From the 1960s, synthesis of ZnO thin films has been an active field because of their applications as sensors, transducers and catalysts [58]. In the last few decades, a variety of ZnO nanostructure morphologies, such as nanowires [10-12], nanorods [13-16], tetrapods [17-19], nanoribbons/belts [20-22], and nanoparticles [23, 24] have been reported. ZnO nanostructures have been fabricated by various methods, such as thermal evaporation [16-21], metal-organic vapor phase epitaxy (MOVPE) [15], laser ablation [16], hydrothermal synthesis [13, 14], sol-gel method [23, 24] and template-based synthesis [12]. Recently, novel morphologies such as hierarchical nanostructures [25], bridge-/nail-like nanostructures [26], tubular nanostructures [27], nanosheets [28], nanopropeller arrays [29, 30], nanohelices [29, 31], and nanorings [29, 31] have, amongst others, been demonstrated. Some of the possible ZnO nanostructure morphologies are shown in Fig. 1.2. Several recent review articles have summarized progress in the growth and applications of ZnO nanostructures [32-34].

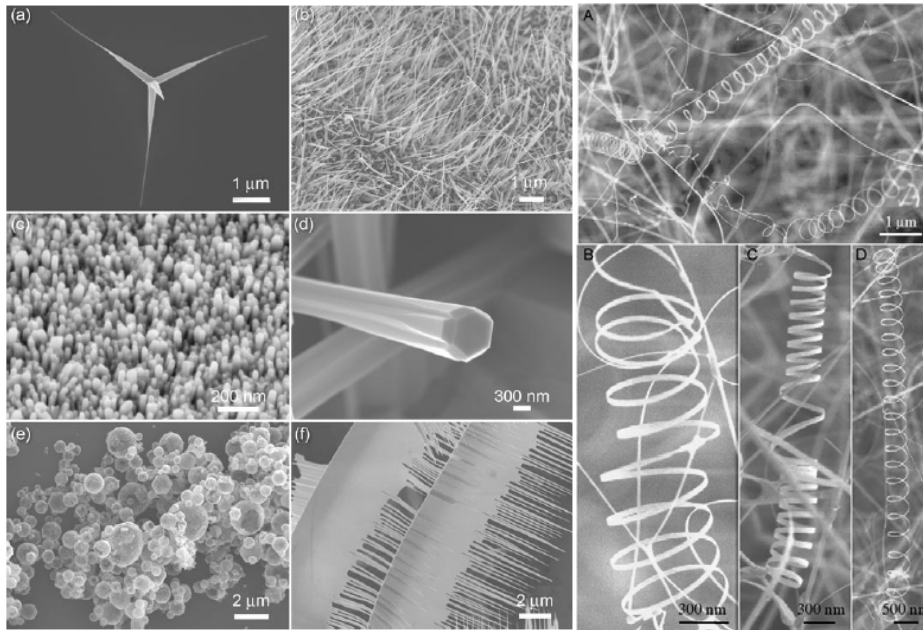


Fig. 1.2 Representative scanning electron microscopy images of various ZnO nanostructure morphologies [32-34].

Additionally, as the dimensions of semiconductors are reduced to the nanometer scale, the optical properties of these are much different from their bulk materials [35-37]. There are two incompatible physical mechanisms in modifying the energy band structure of nanostructures, i.e., the quantum confinement effect (QCE) and surface states [38]. These two mechanisms compete with each other to influence PL spectra. For nanodots or nanostructures in ZnO system with diameters less than 10 nm, the QCE plays a dominant role as has been much reported [39, 40]. On the other hand, the surface-to-volume ratio also brings much influence on the system's Hamiltonian when the material size is reduced to the nanometer scale [41, 42]. The predominance of surface states is responsible for many novel physical features of nanomaterials [43, 44]. Recently, Guo *et al.* [45] exhibited significantly enhanced UV luminescence, diminished visible luminescence and excellent third-order nonlinear optical response with poly (vinyl

pyrrolidone) (PVP) modified surface of ZnO nanoparticles. Norberg and Gamelin [46] observed that changes in nanocrystal size, shape, and luminescence intensities have been measured for nanocrystals capped by dodecylamine (DDA) and trioctylphosphine oxide after different growth times. They explained the green trap emission intensities show a direct correlation with surface hydroxide concentrations. Contrary to expectations, there is no direct correlation between excitonic emission quenching and surface hydroxide concentrations. The nearly pure excitonic emission observed after heating in DDA is attributed to the removal of surface defects from the ZnO nanocrystal surfaces and to the relatively high packing density of DDA on the ZnO surfaces. Furthermore, Shaish *et al.* [47] showed that intensity relations of below-band-gap and band-edge luminescence in ZnO nanowires depend on the wire radius. The weight of this surface luminescence increases as the wire radius decreases at the expense of the band-edge emission. Pan *et al.* [48] also predicated a significant increase in the intensity ratio of the deep level to the near band edge emission is observed with ever-increasing nanorod surface-aspect ratio. Thus, in quantum-size nanostructures, surface-recombination may entirely quench band-to-band recombination, presenting an efficient sink for charge carriers that unless deactivated may be detrimental for electronic devices. Although there were many experiments to describe the influence of surface states and electronic behavior in ZnO nanostructure, it is still lack of experimental and theoretical studies [61, 62] of the influences of crystalline size on electronic structure and surface states in ZnO.

1.3 Motives

In this dissertation, we experimentally and theoretically study the influences of finite crystallize on optical properties and electronic behavior of ZnO quantum structures. In experiment, we first show how to grow high-quality ZnO QDs by a simple sol-gel method. The average size of nanoparticles can be tailored by the appropriate concentration of zinc precursor. For optical properties analysis, Raman scattering can yield important information about the nature of the solid on a scale of the order of a few lattice constants, it can be used to study the microscopic nature of structural and/or topological disorder. Raman scattering thus has been widely used to study the influence of phonon demeanor in finite size of ZnO crystalline. Furthermore, PL measurement is a suitable tool to determine the crystalline quality and the presence of impurities in the material as well as exciton fine structures. It is imperative to fully characterize the excitons in ZnO since not only are excitons a sensitive indicator of material quality but also they play an important role in the stimulated emission and gain processes in real device structures. Especially, the exciton-phonon interaction has significant influence on the optical properties of nanostructure semiconductors. The influence of crystal structure and morphology were studied in detail recently in ZnO nanostructure system, but the effects on the optical properties of fabricated nanostructures are still unknown. Since, we will investigate the interesting optical features of crystal structures and lattice dynamics, Raman vibrational properties, and exciton-LO-phonon coupling in use of Raman and PL spectroscopy.

In theoretical, we present the electronic band structure and total density of states (DOS) of ZnO and ZMO compound crystallization using the nearest- and the

next-nearest-neighbor SETB approach sp^3 model. We limit the number of nonzero tight-binding parameters to one-center on-site integrals and the nearest neighbor two-center integrals, as discussed by Slater and Koster [49]. We also used SETB method to investigate the electronic structure and surface states of ZnO finite well structure considering non-relaxed and non-reconstructed surfaces with growth different directions.

1.4 Organization of the dissertation

This dissertation is organized as follows. Chapter 2 presents a general concept of crystal structures, lattice dynamics, fundamental optical transitions, and tight binding method. In Chapter 3, we demonstrated the synthesis of the ZnO QDs and show the brief illustrations of characterization techniques. In Chapter 4, the morphology, crystal structures, and lattice dynamics were discussed with different crystallize size of ZnO QDs. Chapter 5 elucidates the increase of exciton binding energy may result from the decrease of exciton Bohr radius making the exciton less polar thereby reducing the coupling to LO phonons. Chapter 6 and Chapter 7 we calculated the electronic structure and surface states in the wurtzite structure of ZnO from bulk to nanostructures using sp^3 semi-empirical tight-binding model. Finally, in Chapter 8, we conclude the studies on the ZnO finite structures and propose several topics of the future works.

References

1. D. EzgFr, Ya. I. Alivov, C. Liu, A. Teke, M. A. Reshchikov, S. Dogan, V. Avrutin, S. J. Cho, H. MorkoA, J. Appl. Phys **98**, 041301 (2005).
2. R. Triboulet, J. Perriere, Prog. Cryst. Growth Charact. Mater **47**, 65 (2003).
3. D. P. Norton, Y. W. Heo, M. P. Ivill, K. Ip, S. J. Pearton, M. F. Chisholm, and T. Steiner, Materials Today **7**, 34 (2004).
4. O. Dulub, L. A. Boatner and U. Diebold, Surf. Sci **519**, 201 (2002).
5. B. Meyer and D. Marx, Phys. Rev. B **67**, 035403 (2003).
6. P. W. Tasker, J. Phys. C: Solid State Phys **12**, 4977 (1979).
7. O. Dulub, U. Diebold and G. Kresse, Phys. Rev. Lett **90**, 016102 (2003).
8. A. Wander, F. Schedin, P. Steadman, A. Norris, R. McGrath, T. S. Turner, G. Thornton and N. M. Harrison, Phys. Rev. Lett **86**, 3811 (2001).
9. V. Staemmler, K. Fink, B. Meyer, D. Marx, M. Kunat, G. S. Gil, U. Burghaus and C. Woll, Phys. Rev. Lett **90**, 106102 (2003).
10. M. H. Huang, S. Mao, H. Feick, H. Yan, Y. Wu, H. Kind, E. Weber, R. Russo, P. Yang, Science **292**, 1897 (2001).
11. M. H. Huang, Y. Wu, H. Feick, N. Tran, E. Weber, P. Yang, Adv. Mater **13**, 113 (2001).

12. C. Liu, J. A. Zapien, Y. Yao, X. Meng, C. S. Lee, S. Fan, Y. Lifshitz, S. T. Lee, *Adv. Mater* **15**, 838 (2003).
13. B. Liu, H. C. Zeng, *J. Am. Chem. Soc* **125**, 4430 (2003).
14. M. Guo, P. Diao, S. Cai, *J. Solid State Chem* **178**, 1864 (2005).
15. W. I. Park, Y. H. Jun, S.W. Jung, G.-C. Yi, *Appl. Phys. Lett* **82**, 964 (2003).
16. A. B. Hartanto, X. Ning, Y. Nakata, T. Okada, *Appl. Phys. A* **78**, 299 (2003).
17. Y. Dai, Y. Zhang, Z. L. Wang, *Solid State Commun* **126**, 629 (2003).
18. V. A. L. Roy, A. B. Djuricic, W. K. Chan, J. Gao, H. F. Lui, C. Surya, *Appl. Phys. Lett* **83**, 141 (2003).
19. H. Yan, R. He, J. Pham, P. Yang, *Adv. Mater* **15**, 402 (2003).
20. Z.W. Pan, Z. R. Dai, Z. L. Wang, *Science* **291**, 1947 (2001).
21. H. Yan, J. Johnson, M. Law, R. He, K. Knutsen, J. R. McKinney, J. Pham, R. Saykally, P. Yang, *Adv. Mater* **15**, 1907 (2003).
22. Y. B. Li, Y. Bando, T. Sato, K. Kurashima, *Appl. Phys. Lett* **81**, 144 (2002).
23. K. F. Lin, H. M. Cheng, H. C. Hsu, L. J. Lin, and W. F. Hsieh, *Chem. Phys. Lett* **409**, 208 (2005).
24. C. J. Pan, K. F. Lin, W. T. Hsu, and W. F. Hsieh, *J. Appl. Phys* **102**, 123504 (2007).
25. J. Y. Lao, J. G. Wen, Z. F. Ren, *Nano Lett* **2**, 1287 (2002).

26. J. Y. Lao, J. Y. Huang, D. Z. Wang, Z. F. Ren, *Nano Lett* **3**, 235 (2003).
27. Y. J. Xing, Z. H. Xi, X. D. Zhang, J. H. Song, R. M. Wang, J. Xu, Z. Q. Xue, D. P. Yu, *Solid State Commun* **129**, 671 (2004).
28. J.-H. Park, H.-J. Choi, Y.-J. Choi, S.-H. Sohn, J.-G. Park, *J. Mater. Chem* **14**, 35 (2004).
29. Z. L. Wang, X. Y. Kong, Y. Ding, P. Gao, W. L. Hughes, R. Yang, Y. Zhang, *Adv. Funct. Mater* **14**, 943 (2004).
30. P. X. Gao, Z. L. Wang, *Appl. Phys. Lett* **84**, 2883 (2004).
31. X. Y. Kong, Z. L. Wang, *Nano Lett* **3**, 1625 (2003).
32. Z. Y. Fan, J. G. Lu, *J. Nanosci. Nanotechnol* **5**, 1561 (2005).
33. G. C. Yi, C. R. Wang, W. I. Park, *Semicond. Sci. Technol* **20**, S22 (2005).
34. Y.W. Heo, D. P. Norton, L. C. Tien, Y. Kwon, B. S. Kang, F. Ren, S. J. Pearton, J. R. LaRoche, *Mater. Sci. Eng* **47**, 1 (2004).
35. X.Y. Kong, Y. Ding, R. Yang and Z. L. Wang, *Science* **303**, 1348 (2004).
36. S. Nakamura, M. Senoh, N. Iwasa, T. Yamada, T. Matsushita, Y. Sugimoto, H. Kiyoku, *Appl. Phys. Lett* **69**, 1568 (1996).
37. L. Bergman, X.B. Chen, J.L. Morrison, J. Huso, A.P. Purdy, *J. Appl. Phys* **96**, 675 (2004).

38. L.T. Canham, Appl. Phys. Lett **57**, 1046 (1990).
39. Y. Kayanuma, Phys. Rev. B **38**, 9797 (1988).
40. M.D. Mason, G.M. Credo, K.D. Weston, S.K. Buratto, Phys. Rev. Lett **80**, 5405 (1998).
41. F. Koch, V. Petrova-Koch, T. Muschit, J. Lumin **57**, 271 (1993).
42. J.B. Xia, K.W. Cheah, Phys. Rev. B **59**, 14876 (2003).
43. J.C. Tsang, M.A. Tischler, R.T. Collins, Appl. Phys. Lett **60**, 2279 (1992).
44. I. Shalish, H. Temhin, V. Narayanamurti, Phys. Rev. B **69**, 245401 (2004).
45. L. Guo, S. Yang, C. Yang, P. Yu, J. Wang, W. Ge, and G. K. L. Wong, Appl. Phys. Lett **76**, 2901 (2000).
46. N. S. Norberg and D. R. Gamelin, J. Phys. Chem. B **109**, 20810 (2005).
47. I. Shalish, H. Temkin, and V. Narayanamurti, Phys. Rev. B **69**, 245401 (2004).
48. N. Pan, X. Wang, M. Li, F. Li, and J. G. Hou, J. Phys. Chem. C **111**, 17265 (2007).
49. J. C. Slater and G. F. Koster, Phys. Rev **94**, 1498 (1954).
50. K. Boldt, O. T. Bruns, N. Gaponik, and A. Eychmuller, J. Phys. Chem. B **110**, 1959 (2007).
51. A. Nemchinov, M. Kirsanova, and N. N. Hewa-Kasakarage, J. Phys. Chem. C **112**, 9301 (2008).

52. A. B. Djurisic and Y. H. Leung, *small*, **2**, 944 (2006).
53. Z. L. Wang, *Appl. Phys. A*, **88**, 7 (2007).
54. E. Hutter, and J. H. Fendler, *Adv. Mater* **16**, 1685 (2004).
55. C. R. Gorla, N. W. Emanetoglu, and S. Liang, *J. Appl. Phys* **85**, 2595 (1999).
56. G. G. Zhao, R. P. Joshi, H. P. Hjalmarson, *Journal of the American Cermaic Society* **91**, 1188 (2008).
57. G. X. Hu, B. Kumar, H. Gong, E. F. Chor, and P. Wu, *Appl. Phys. Lett.* **88**, 101901 (2006).
58. R. Martins, P. Barquinha, I. Ferreira, L. Pereira, G. Goncalves, and E. Fortunato, *J. Appl. Phys* **101**, 044505 (2007).
59. Y. Sun, G. M. Fuge, N. A. Fox, D. J. Riley, and M. N. R. Ashfold, *Adv. Mater* **17**, 2477 (2005).
60. S. J. Pearton, D. P. Norton, K. Ip, Y. W. Heo, and T. Steiner, *Pross. Mater. Sci.* **50**, 293 (2005).
61. J. W. Chiou, J. C. Jan, H. M. Tsai, C. W. Bao, W. F. Pong, M. H. Tsai, I. H. Hong, R. Klauser, J. F. Lee, J. J. Wu, and S. C. Liu, *Appl. Phys. Lett.* **84**, 3462 (2004).
62. J. W. Chiou, H. M. Tsai, C. W. Bao, F. Z. Chien, W. F. Pong, C. W. Chen, M. H. Tsai, J. J. Wu, C. H. Ko, J. F. Lee, and J. H. Guo, *J. Appl. Phys* **104**, 013709 (2008).

Chapter 2 Theoretical background

In this chapter, we will discuss in detail the crystal structures, lattice dynamics, excitons-related emissions, quantum size effect and tight binding method. Lattice dynamics corresponding to the selection rules, lattice vibrational properties, and polar-optical phonon scattering mechanism are discussed. Optical transitions in ZnO have been studied by a variety of experimental techniques such as optical absorption, transmission, reflection, photoluminescence (PL), and cathodoluminescence spectroscopies, etc. In Section 2.2, we reviewed some fundamental issues related to the optical properties of ZnO single crystal by PL measurement. In Section 2.3, the quantum effect was described in nanostructures using effective mass model. Finally, we detail the SETB approach sp^3 model of wurtzite semiconductors.

2.1 Crystal structures and Lattice dynamics

2.1.1 Crystal structures [1]

Most of the group II-VI binary compound semiconductors crystallize in either cubic zinc-blende or hexagonal wurtzite structure in which each anion is surrounded by four cations at the corners of a tetrahedron, and vice versa. This tetrahedral coordination is

typical of sp^3 covalent bonding, but these materials also have a substantial ionic character.

ZnO is a II-VI compound semiconductor whose ionicity resides at the borderline between covalent and ionic semiconductor. The crystal structures shared by ZnO are wurtzite (B4), zinc blende (B3), and rocksalt (B1), as schematically shown in Fig. 2-1. At ambient conditions, the thermodynamically stable phase is wurtzite. The zinc-blende ZnO structure can be stabilized only by growing on cubic substrates, and the rocksalt structure may be obtained at relatively high pressures.

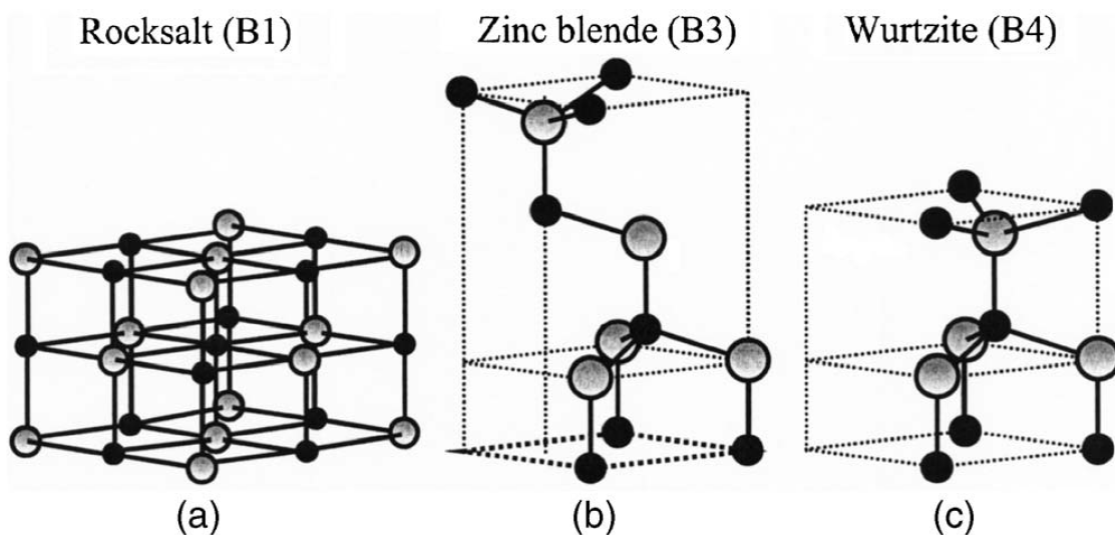


Fig. 2-1 Stick and ball representation of ZnO crystal structures: (a) cubic rocksalt (B1), (b) cubic zinc blende (B3), and (c) hexagonal wurtzite (B4). The shaded gray and black spheres denote Zn and O atoms, respectively.

The wurtzite structure has a hexagonal unit cell with two lattice parameters, a and c , in the ratio of $c/a = \sqrt{8/3} = 1.633$ and belongs to the space group of C_{6v}^4 or $P6_3mc$. A schematic representation of the wurtzitic ZnO structure is shown in Fig. 2-2. The structure is composed of two interpenetrating hexagonal-close-packed (hcp) sublattices, each of which consists of one type of atom displaced with respect to each other along the threefold c -axis by the amount of $u = 3/8 = 0.375$ in an ideal wurtzite structure. The fractional coordinate, the u parameter, is defined as the length of the bond parallel to the c axis in unit of c . Each sublattice includes four atoms per unit cell and every atom of one kind (group-II atom) is surrounded by four atoms of the other kind (group VI), or vice versa, which are coordinated at the edges of a tetrahedron.

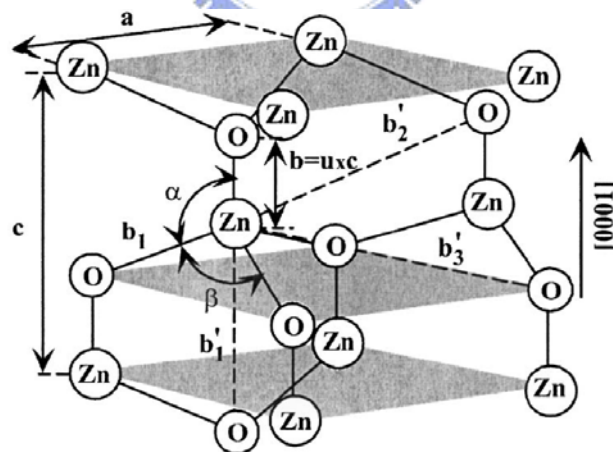


Fig. 2-2 Schematic representation of a wurtzitic ZnO structure having lattice constants a in the basal plane and c in the basal direction; u parameter is expressed as the bond length or the nearest-neighbor distance b divided by c , and α and β are the bond angles.

In a real ZnO crystal, the wurtzite structure deviates from the ideal arrangement, by changing the c/a ratio or the u value. It should be pointed out that a strong correlation exists between the c/a ratio and the u parameter when the c/a ratio decreases. The u parameter increases in such a way that those four tetrahedral distances remain nearly constant through a distortion of tetrahedral angles due to long-range polar interactions. The lattice parameters of a semiconductor usually depend on the following factors: (i) free-electron concentration acting via deformation potential of a conduction-band minimum occupied by these electrons; (ii) concentration of foreign atoms and defects and their difference of ionic radii with respect to the substituted matrix ion; (iii) external strains (for example, those induced by substrate); and (iv) temperature. The lattice parameters of any crystalline material are commonly and most accurately measured by high resolution x-ray diffraction (HRXRD). For the wurtzite ZnO, the lattice constants at room temperature determined by various experimental measurements and theoretical calculations are in good agreement. The lattice constants mostly range from 3.2475 to 3.2501 Å for the a parameter and from 5.2042 to 5.2075 Å for the c parameter. The c/a ratio and the u parameter vary in a slightly wider range, from 1.593 to 1.6035 and from 0.383 to 0.3856, respectively. The deviation from that of the ideal wurtzite crystal is probably due to lattice stability and ionicity. It has been reported that free charge is the

dominant factor responsible for expanding the lattice proportional to the deformation potential of the conduction-band minimum and inversely proportional to the carrier density and bulk modulus. The point defects such as zinc antisites, oxygen vacancies, and extended defects, such as threading dislocations, also increase the lattice constant, albeit to a lesser extent in the heteroepitaxial layers.

2.1.2 Symmetry properties and phonon modes of inelastic cross sections [2, 3]

The symmetry properties of the scattering cross sections are determined by the symmetry properties of second-order susceptibility for the excitation concerned. The spatial symmetry properties of the scattering medium lead to further connections between the cross section measured in different experiments on the same sample. The Stokes cross section for different polarization of the incident and scattered light are often related by the spatial symmetry, and the cross section is sometimes required to vanish for certain polarizations that depend on the nature of the excitation.

The spatial symmetry of the scattering medium is formally specified by its symmetry group, the group of all spatial transformations that leave the medium invariant. Individual atoms and molecules have spatial symmetries characterized by a point group consisting of rotations and reflections that leave the atom or molecule invariant. The

atomic arrangements in a regular crystal lattice are characterized by a space group that contains translations in addition to rotations and reflections. The effects of the translational invariance of a crystal are largely accounted for in the momentum conservation conditions, and the residual effects of the spatial symmetry derive from the crystal point group that remains on removal of translations from the space group. There are 32 different crystal point groups. The effects of spatial symmetry are particularly important for scattering by crystal samples, and the anisotropy of the cross section is generally different for the different crystal symmetries. We consider in the present section the restrictions imposed on the cross section by the point symmetry of a crystal.

The spatial properties of the excitations of the scatter are described by irreducible representations of its symmetry group. Let Γ_X be the irreducible representation appropriate to the excitation; we call Γ_X the excitation symmetry. In the microscopic theory with an initial state $|i\rangle$ of symmetry Γ_i and a final state $|f\rangle$ of symmetry Γ_f , the excitation symmetry is that of the operator $|f\rangle\langle i|$, which projects the initial state onto the final state. Thus

$$\Gamma_X = \Gamma_f \times \Gamma_i^*, \quad (2-1)$$

where the asterisk denotes complex conjugation. The transformation properties of the incident and scattered light are described by the three-dimensional polar-vector

representation Γ_{PV} of the point group considered, since the quantities incident field (E_I), Stokes field (E_S), and Stokes polarization (P_S), which characterize the light, are all polar vectors.

The relation between Stokes polarization, excitation amplitude, and incident field must be invariant under all the spatial transformations of the symmetry group of the scattering. This invariance condition (for detailed discussion, see Nye 1957 [4]) is common to all equations that relate properties of a system with given spatial symmetry. It has two main consequences for light scattering.

The first consequence is the existence of selection rules. In group theoretical language, only those Γ_X are allowed for which the direct product $\Gamma_X \times \Gamma_{PV}$ includes the polar vector representation Γ_{PV} (or an irreducible part of it) in its decomposition. An equivalent statement is that those Γ_X that occur in the decomposition of $\Gamma_{PV}^* \times \Gamma_{PV}$ are the allowed excitation symmetries. The scattering of light by all excitations whose symmetries do not satisfy this condition is a forbidden process.

The second consequence of the invariance condition is the imposition of restrictions on the components of the second-order susceptibility for those excitation symmetries that are allowed in light scattering. For each allowed Γ_X , some of the Cartesian components, i and j , are required to have related values. Nye (1957) gives details of similar

determinations of the symmetry properties of a wide range of tensor quantities in various crystal symmetries.

Poulet and Mathieu [5] give the fullest account of the calculation of selection rules and symmetry properties of second-order susceptibilities for inelastic light scattering. These calculations are not repeated here, but the main results for the 32 crystal point groups are set out in Ref. 5, which were divided into three parts, for crystals with biaxial, uniaxial, and isotropic dielectric properties. GaN-, AlN- and InN-based materials are highly stable in the hexagonal wurtzite structure (uniaxial) although they can be grown in the zinc blende phase and unintentional phase separation and coexistence may occur. The wurtzite crystal structure belongs to the space group C_{6v}^4 and group theory predicts zone-center optical modes are A_1 , $2B_1$, E_1 and $2E_2$. The A_1 and E_1 modes and the two E_2 modes are Raman active while the B modes are silent. The A and E modes are polar, resulting in a splitting of the LO and TO modes (Hayes and Loudon, 1978 [6]). The Raman tensors for the wurtzite structure are as follows:

$$\begin{pmatrix} a & 0 & 0 \\ 0 & a & 0 \\ 0 & 0 & b \end{pmatrix} \quad A_1 (z) \text{ mode,}$$

$$\begin{pmatrix} 0 & 0 & c \\ 0 & 0 & 0 \\ c & 0 & 0 \end{pmatrix} \quad E_1 (x) \text{ mode,}$$

$$\begin{pmatrix} 0 & 0 & 0 \\ 0 & 0 & c \\ 0 & c & 0 \end{pmatrix} \quad E_1 (y) \text{ mode,}$$

$$\begin{pmatrix} f & 0 & 0 \\ 0 & -f & 0 \\ 0 & 0 & 0 \end{pmatrix} \begin{pmatrix} 0 & -f & 0 \\ -f & 0 & 0 \\ 0 & 0 & 0 \end{pmatrix} \quad E_2 \text{ mode.}$$

Here x , y or z in brackets after an irreducible representation indicates that the vibration is also infra-red active and has the direction of polarization indicated. Such vibrations occur only in piezo-electric crystals (i.e. crystals with no center of inversion symmetry).

In crystals which do have a center of inversion symmetry, only even-parity vibrations, whose representations have a subscript g , can be Raman active and only odd-parity (subscript u) vibrations can be infrared active. This fact leads to the important complementary nature of infra-red absorption and Raman effects measurements.

Directly above each irreducible representation is a matrix, which gives the non-vanishing components of the Raman tensor, i.e., of $\alpha_{\rho\sigma,\mu}$ or $R_{\rho\sigma}^{\mu}$. The different elements of the matrices are the nine components of the tensor obtained by allowing both ρ and σ to take

on the values x , y and z . Here x , y , and z are the crystal principal axes chosen to be identical with the principal axes x_1 , x_2 and x_3 defined for all the crystal classes by Nye. The component μ of the phonon polarization for the case of infrared-active vibrations is the quantity given in brackets after the irreducible representation symbol.

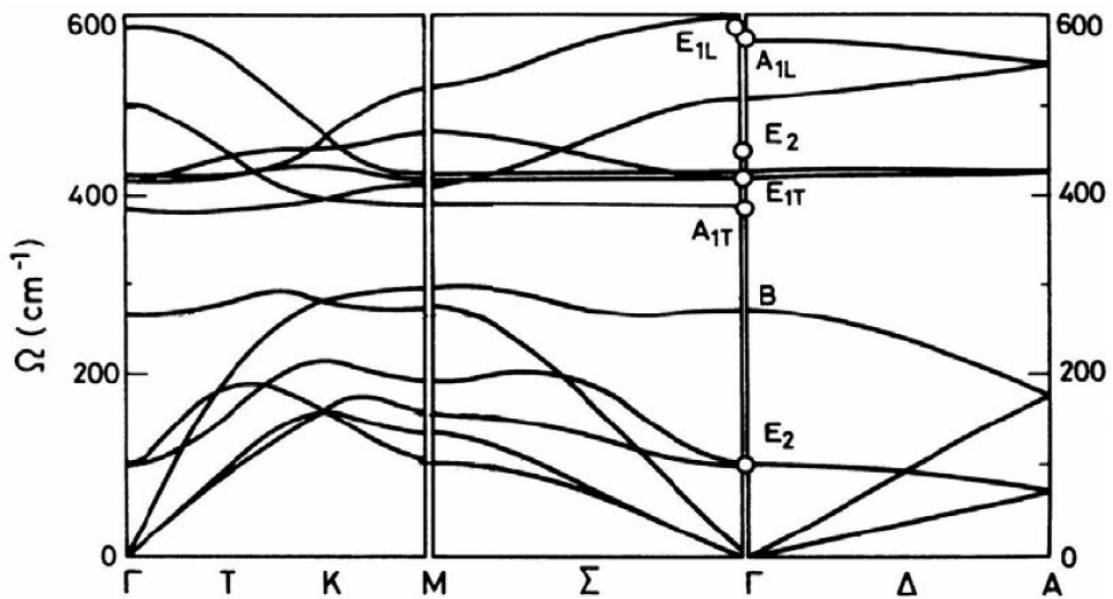


Fig. 2-3 Phonon dispersion curves for ZnO crystal of wurtzite structure. (after Calleja *et al.* [7])

The vibrational modes in ZnO wurtzite structures are given in Figure 2-3. At the Γ point of the Brillouin zone, it can be seen that the existence of the following optic phonon modes: $A_1+2B_1+E_1+2E_2$; A_1 and E_1 modes are both Raman and infrared active; and B_1 (*low*) and B_1 (*high*) modes are silent. For the lattice vibrations with A_1 and E_1

symmetries, the atoms move parallel and perpendicular to the c axis, respectively. The low-frequency E_2 mode is associated with the vibration of the heavy Zn sublattice, while the high-frequency E_2 mode involves only the oxygen atoms. The displacement vectors of the phonon normal modes are illustrated in Fig. 2-4. In the case of highly oriented ZnO films, if the incident light is exactly normal to the surface, only A_1 (LO) and E_2 modes are observed, and the other modes are forbidden according to the Raman selection rules. Table 2-1 gives a list of observed zonecenter optical-phonon wave numbers along with those calculated for wurtzite ZnO.

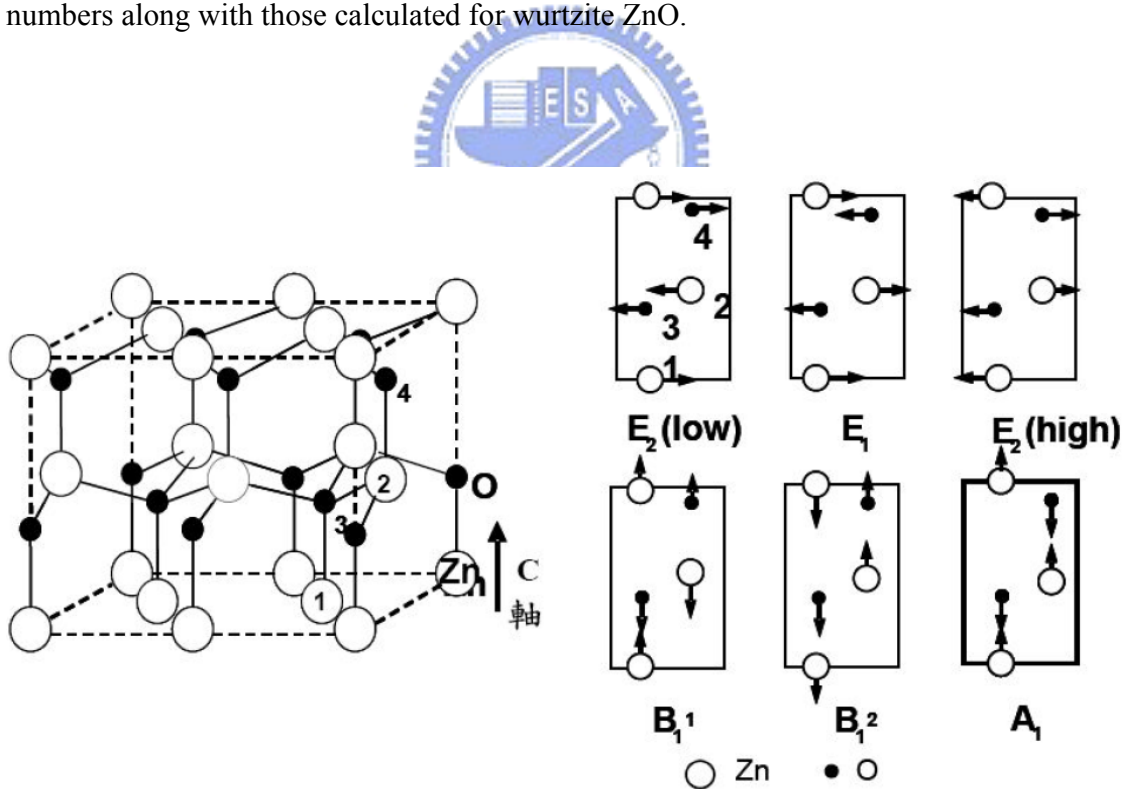


Fig. 2-4 Displacement vectors of the phonon modes in ZnO wurtzite structure. (after Jephcoat et al. [8])

Table 2-1 Phonon mode frequencies of wurtzite ZnO at the center of the Brillouin zone obtained from infrared spectroscopic ellipsometry and Raman scattering measurements in comparison with theoretical predictions [1].

Symmetry	Raman spectroscopy	Infrared spectroscopy	Theor. calc.
A_1 -TO	380(2), ^a 379(2), ^b 380, ^c 380, ^d 378, ^e 380 ^f	380 ^g	382, ^h 386 ⁱ
E_1 -TO	409(2), ^a 410(2), ^b 407, ^c 413, ^d 409.5 ^e	409.1(0.9), ^a 408.2(0.3), ^b 412 ^g	316, ^h 407 ⁱ
A_1 -LO	574, ^d 576, ^e 579, ^d 579 ^f	574.5(0.3), ^a 577.1(0.4), ^b 570 ^g	548 ^h
E_1 -LO	587(2), ^a 591(2), ^b 583, ^c 588, ^e 591 ^d	588.3(0.7), ^a 592.1(0.2), ^b 591 ^g	628 ^h
E_2 -low	102(1), ^a 102(1), ^b 101, ^c 101, ^d 98, ^e 99 ^f		126, ^h 98 ⁱ
E_2 -high	438(1), ^a 437(1), ^b 437, ^c 444, ^d 437.5, ^e 438 ^f		335, ^h 433 ⁱ
B_1 -low			240
B_2 -high			540

2.2 Excitons-related emissions

Optical properties of a variety of forms of ZnO, including ZnO nanostructures, have been studied by PL spectroscopy. The majority of the reported luminescence spectra of ZnO nanostructures have been measured at room temperature, although variable-temperature PL studies have been performed on some of the samples. Room-temperature PL spectra of ZnO typically consist of a UV emission and possibly

one or more visible bands due to defects and/or impurities.

2.2.1 UV Emission [1, 29]

Low-temperature PL measurements of different nanostructures, such as nanowire/nanowall systems, nanosheets, nanowalls, nanowires, nanorods, faceted nanorods, nanoparticles, nanoblades and nanoflowers have been reported [9-13]. Low temperature (4-10 K) PL spectra of ZnO typically exhibit several peaks (labeled I₀-I₁₁), which correspond to bound excitons [14]. An example of a low-temperature PL spectrum of a ZnO sample exhibiting a number of bound-exciton peaks is shown in Fig.

2-5.

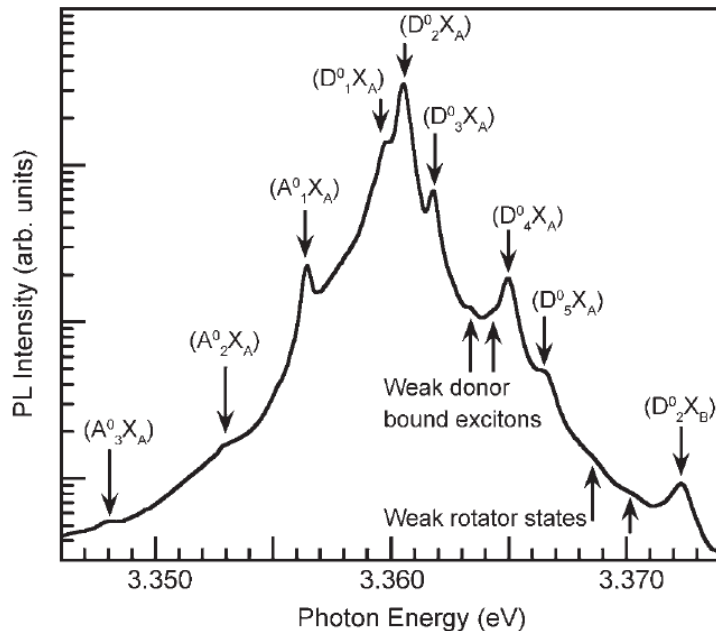


Fig. 2-5 Bound-excitonic region of the 10 K PL spectrum for the forming gas annealed ZnO substrate [15].

The number of observed bound-exciton peaks in ZnO nanostructures is typically lower than that in ZnO single crystals. An example of a low-temperature and their capture cross sections, [15] variable-temperature PL measurements can provide useful information about the optical and structural properties of ZnO. However, the assignment of the bound-exciton peaks in ZnO is, in general, controversial for all forms of the samples, namely, ZnO single crystals, epitaxial films, and nanostructures. For example, it was proposed that the emission lines I_5 to I_{11} in the lower part of the energy spectrum can be attributed to excitons bound to neutral acceptors [16]. However, other reports in the literature attributed some of these lines to donor bound excitons [15, 17]. The chemical identity of the donors and acceptors responsible for different bound-exciton lines still remains unclear (for a complete list of the bound-exciton peaks generally observed in ZnO, and a summary of the possible identification of the donors and acceptors, see Ref.1 and Ref.15]). One of the commonly observed bound-exciton lines in ZnO nanostructures is the I_4 line at near the 3.3628 eV [18]. This emission is typically attributed to the donor bound exciton, and the donor has been identified as hydrogen [14, 19]. Theoretical calculations predict hydrogen to be a shallow donor in ZnO and it is reasonable to expect that an unintentional incorporation of hydrogen could frequently happen in ZnO nanostructure synthesis. While in general there is a

consensus in assigning the I_4 line to hydrogen donors [14, 19], the chemical identity of donors responsible for other donor bound-exciton lines remains unclear.

For the acceptor bound excitons, the most commonly reported peak is located at 3.3564 eV. This peak is commonly attributed to excitons bound to Na or Li acceptors [1]. Alkali metals are predicted to produce shallow acceptors on the cation site, but the experimental results demonstrate that doping with group I ions produces complex results [20].

However, other acceptor levels have also been proposed, such as an acceptor complex involving a N impurity on an O site [21]. Some authors attribute this line to a donor bound exciton instead. Bound-exciton lines I_6 , I_8 , and I_9 have been assigned to excitons bound to Al, Ga, and In donors, respectively [14]. On the other hand, Thonke *et al.* [18] proposed that the weak 3.357 eV line corresponds to the acceptor bound exciton, while the I_8 line at 3.3597 eV was found to be a donor bound-exciton line.

In addition to commonly observed acceptor bound-exciton lines, emission at 3.332 eV (labeled as I_a) was recently observed in low-temperature PL spectra of ZnO epilayers grown on CaF₂(111) [22]. Since this peak occurs in the spectral region where two-electron satellites (TES) of donor bound-exciton peaks are expected to occur [18], careful examination of the peak position in respect to known bound-exciton positions and

expected TES peaks (see Ref. [14] for the positions of TES lines for different bound-exciton peaks) is necessary. In addition, the occurrence of peak near 3.333 eV may indicate excitons bound to structural defects [14]. Therefore, further work is needed for conclusive identification of the origin of different bound-exciton lines in ZnO. The assignment of several bound-exciton lines, especially I₉, is still controversial and conclusive chemical identification of the majority of donors and acceptors has not been accomplished.

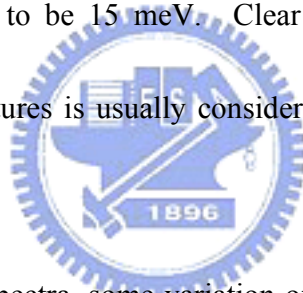
At low temperatures, in addition to bound-exciton peaks, TES transitions can be observed in the spectral region 3.32 – 3.34 eV [15]. These transitions correspond to a radiative recombination of donor bound excitons, which leaves the donor in an excited state. Thus, they are located at energy lower by an amount equal to the difference between the first excited and ground states of the donor, so that their position in respect to the donor bound-exciton peaks can be used to estimate donor-binding energies. Finally, low-temperature PL spectra can also contain donor-acceptor pair transitions and longitudinal optical (LO) phonon replicas. The first-, second-, and third-order LO phonon replicas can typically be observed. The LO phonon energy can be determined from the separation between the exciton peaks and their LO phonon replicas, and for ZnO it is 71-73 meV. Since donor-acceptor pair transitions and some of the LO phonon

replicas occur in the same spectral region (3.218-3.223 eV), care needs to be taken in assigning the peaks observed in this region.

With regard to the temperature dependence of the observed peaks, a red shift of the free-exciton emission with increasing temperature occurs. The intensity of the bound-exciton peaks and the LO phonon replicas decreases with increasing temperature, and only free-exciton emission can be observed at room temperature. In ZnO epilayers, free-exciton emission was found to dominate the spectra above ~80 K [23]. Similar behavior, with the disappearance of bound-exciton peaks above 150 K, was also observed in ZnO single-crystal samples. The bound-exciton line for ZnO nanoparticles embedded in alkali halide crystals also disappeared at ~125 K [24]. The exact temperature at which the bound-exciton line will disappear depends on the identity of the donors or acceptors, since different donors/acceptors will be thermally ionized at different temperatures. It should be noted that in the case of donor-acceptor pair transition, disappearance of this peak with increasing temperature can be accompanied by the appearance of acceptor bound-exciton peaks if the acceptors are thermally ionized at higher temperature than the donors [25].

However, what all ZnO samples (single crystals, films, and nanostructures) have in common is the disappearance of bound-exciton peaks at temperatures in the range 50-150

K, while at room temperature only free-exciton emission is observed. The presence of free-exciton emission at low temperatures, as well as a distinction between A and B exciton peaks, is usually considered to indicate high quality in ZnO samples. It should be noted that this criterion for sample quality is less arbitrary than the ratio between UV and defect emission, which is sometimes used to estimate sample quality, and which is dependent on excitation area and power. Additionally, biexciton emission was observed at ~ 77 K in high-quality epitaxial ZnO films and nanopowder [23, 26]. The biexciton binding energy was estimated to be 15 meV. Clear observation of free-exciton and biexciton lines at low temperatures is usually considered as an indication of very good sample quality.



In room-temperature PL spectra, some variation of the position of the PL peak can be observed for different nanostructures. This is illustrated in Fig. 2-6, where different UV peak positions (387 nm for tetrapods, 381 nm for needles, 397 nm for nanorods, 377 nm for shells, 379 nm for faceted rods, and 385.5 nm for ribbons/combs) can be observed. These differences in the peak positions of individual nanostructures, which are sufficiently large so that there could be no quantum confinement effects, indicate that there is likely a different explanation for the variation in the band-edge emission in ZnO nanostructures reported in different studies. Even though quantum confinement has

been proposed as a cause of the blue shift of the band-edge emission with decreasing size, any shift due to quantum confinement in nanocrystals with diameters of 57, 38, and 24 nm were not likely considering the fact that the Bohr radius of ZnO is 2.34 nm [27].

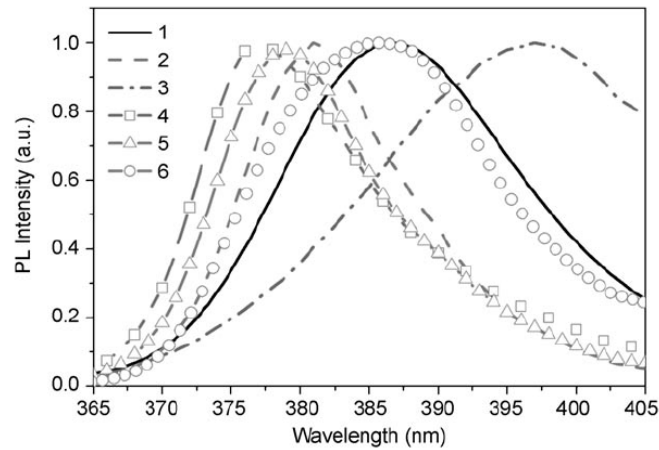


Fig. 2-6 Room-temperature PL spectra of various nanostructures in the UV range [29]: 1) Tetrapods, 2) needles, 3) nanorods, 4) shells, 5) highly faceted rods, 6) ribbons/combs.

One possible reason for the variations in the position of the band-edge emission in various ZnO nanostructures with relatively large dimension is different concentrations of native defects. Since the defect density on the surface is higher than in the bulk, spectral shifts due to different defect concentrations are expected to occur in nanostructures with different sizes due to different surface-to-volume ratios [28]. The fact that the decay times in time-resolved PL from ZnO nanorods are size dependent is in agreement with

the assumption of different defect levels/concentrations for structures with different surface-to-volume ratios. Thus, the defects could affect the position of the band-edge emission as well as the shape of the luminescence spectrum. Although there have been several reports with strong UV and weak defect emission in ZnO nanostructures, in some cases only defect emission is observed or the UV emission is much weaker compared to the defect emission. Therefore, clarifying the origins of different defect emissions is an important issue. However, it should be noted that the ratio of the intensity of UV and defect emission is dependent on the excitation density, as well as the excitation area. Thus, the ratios of these two emissions cannot be used as an absolute determining factor of the crystalline quality of ZnO, although they are useful in comparing the quality of different samples when the measurements are performed under identical excitation conditions.

2.2.2 Defect Emission [29]

Room-temperature PL spectra from ZnO can exhibit a number of different peaks in the visible spectral region, which have been attributed to the defect emission. Emission lines at 405, 420, 446, 466, 485, 510, 544, 583, and 640 nm have been reported. Several calculations of the native defect levels in ZnO have been reported [30, 31] as summarized

in Fig. 2-7. An example of defect emissions (normalized PL spectra) from different ZnO nanostructures is shown in Fig. 2-8.

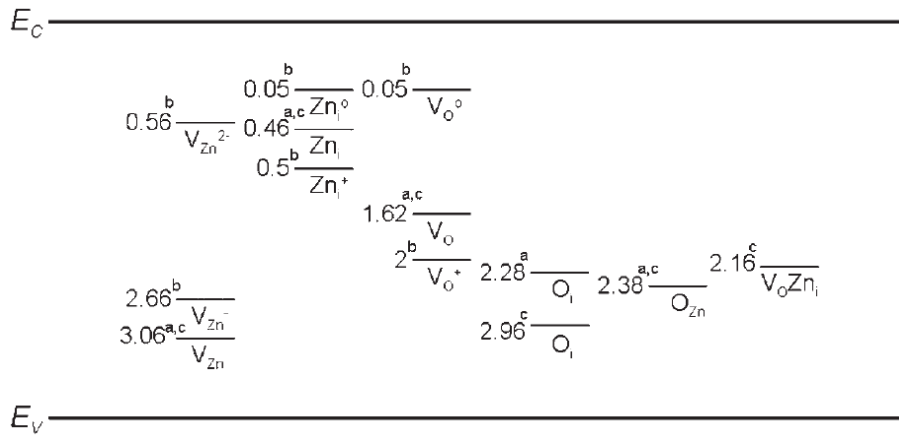


Fig. 2-7 Illustration of the calculated defect energy levels in ZnO [29].



Green emission is the most commonly observed defect emission in ZnO nanostructures, similar to other forms of ZnO. The intensity of the blue-green defect emission was found to be dependent on the nanowire diameter, [32, 33] but both increased [32] and decreased [33] defect emission intensity with decreased wire diameter were reported.

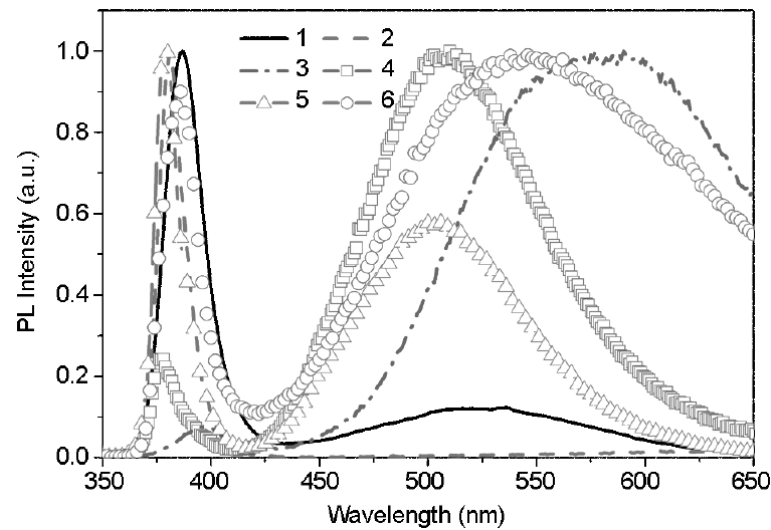


Fig. 2-8 Room-temperature PL spectra of different nanostructures [29]: 1) Tetrapods, 2) needles, 3) nanorods, 4) shells, 5) highly faceted rods, 6) ribbons/combs.



Several hypotheses have been proposed. Green emission is often attributed to singly ionized oxygen vacancies, although this assignment is highly controversial. Other hypotheses include antisite oxygen, which was proposed by Lin et al. [31] based on the band structure calculations. Green emission was also attributed to oxygen vacancies and zinc interstitials [34]. Cu impurities have been proposed as origin of the green emission in ZnO. Blue-green defect emission was also reported in Cu doped ZnO nanowires [35]. Although Cu was identified as a possible cause of green emission in ZnO, this cannot explain the defect emission in all ZnO nanostructure samples, especially those where defect emission exhibits strong dependence on annealing temperature and

atmosphere which would be more consistent with an intrinsic defect rather than Cu impurity. Other hypotheses include various transitions related to intrinsic defects, such as donor-acceptor transitions, recombination at Vo^{**} centers (where these centers are generated by surface trapping of photogenerated holes, followed by recombination with electron in an oxygen vacancy Vo^* [36]), zinc vacancy [37], and surface defects [38]. Although the singly ionized oxygen vacancy is a commonly cited hypothesis, which is supported by reports of the enhancement of the green defect by annealing at temperatures above 600°C (attributed to out-diffusion of O), this assignment has been questioned recently. On the other hand, while the Zn vacancy hypothesis is supported by the study of the effect of O and Zn implantation [39], a blue rather than green emission would be expected based purely on the theoretically predicted energy levels for Zn vacancy. Therefore, the origin of the green emission is still an open and controversial question and the identification of the exact origin of this emission requires further study. While the type of defect responsible for the green emission has not yet been conclusively identified, there is convincing evidence that it is located at the surface. It was shown that coating ZnO nanostructures with a surfactant suppressed green emission. Polarized luminescence experiments from aligned ZnO nanorods also indicated that green emission originated from the surface of the nanorods [40]. The surface recombination layer

responsible for visible emission in ZnO nanowires was estimated to be ~30 nm in thickness. Also, the possible presence of Zn(OH)₂ at the surface, especially for nanostructures prepared by solution methods, could affect the emission spectra from ZnO nanostructures.

Yellow defect emission is also commonly reported in ZnO nanostructures [41, 42], and it represents a common feature in samples prepared from aqueous solutions of zinc nitrate hydrate and hexamethylenetetramine. This emission is typically attributed to oxygen interstitial, although a Li impurity represents another possible candidate. The deep levels responsible for green and yellow emissions were found to be different; unlike the defect responsible for the green emission, the defect responsible for the yellow emission is not located at the surface.

In addition to green and yellow emissions, orange-red emissions are often also observed. Fan *et al.* [43] reported that the visible emission in ZnO dendritic wires and nanosheets consisted of two components centered at ~540 and ~610 nm. The intense visible emission in ZnO nanosheets was tentatively attributed to surface dislocations. Orange-red emission at ~626 nm in ZnO nanorods was attributed to oxygen interstitials. In addition, orange emission at ~640-650 nm in ZnO needles and nanowires [44] was proposed to be due to oxygen-rich samples, in agreement with a previous study on ZnO

films. This emission could be reduced by annealing under vacuum or in a H₂/Ar mixture [44]. In addition to identifying the origin of the defect emissions, an important question is the suppression of defect emission either by varying the fabrication conditions or by post-fabrication treatment. It was reported that the green emission from ZnO nanoparticles can be suppressed by embedding the nanoparticles into a synthetic opal whose photonic bandgap overlaps with the deep-level emission [45]. Another way to suppress green defect emission is by coating of the surface with surfactant [38]. Hydrogen plasma was also shown to enhance UV-to-defect emission intensity ratio for ZnO nanorods [103]. As for the yellow emission, it has been shown that it can be reduced by annealing in a reducing environment (hydrogen/argon mixture) [41].

2.3 Quantum size effect

During the last decade, the growth of low-dimensional semiconductor structures has made it possible to reduce the dimension from three (bulk material) to the quasi-zero dimensional semiconductor structures usually called QDs. In these nanostructures the quantum confinement effects become predominant and give rise to many interesting electronic and optical properties. The electron energy becomes quantized and depends on the dot size. The band gap and the density of states (DOS) associated with a

quantum-structure differ from that associated with bulk material, determined from the magnitude of the three-dimension wave vector.

2.3.1 Quantum confinement effect

Models explaining the confinement of charged particles in a three-dimensional potential well typically involve the solution of Schrodinger's wave equation using the Hamiltonian [46]

$$H = -\frac{\hbar^2}{2m_e} \nabla_e^2 - \frac{\hbar^2}{2m_h} \nabla_h^2 + V_0 + U. \quad (2-2)$$

Variation between treatments generally originates from differences in expressions assigned to V_0 for the confining potential well, which normally is accompanied by the Coulombic interaction term U . Boundary conditions are imposed forcing the wave functions describing the carriers to zero at the walls of the potential well. Two regimes of quantization are usually distinguished in which the crystallite radius R is compared with the Bohr radius of the excitons or related quantities: weak confinement for $R \geq a_B$ and strong confinement for $R < a_B$. In the first case crystallite radius is larger than the exciton, as a consequence, the motion of center of mass of the exciton is quantized while the relative motion of electron and hole given by the envelope function $\phi(r_e - r_h)$ is hardly affected. In the second case the Coulomb energy increases roughly

with R^{-1} , and the quantization energy with R^{-2} , so that for sufficiently small values of R one should reach a situation where the Coulomb term can be neglected.

2.3.1.1 Weak confinement [47]

Coulomb-related correlation between the charged particles handled through the use of variational approach involving higher-order wave function of the confined particles, and we can not neglect the electron hole Coulomb potential. The Schrödinger equation may be written as

$$\left(-\frac{\hbar^2}{2m_e} - \frac{\hbar^2}{2m_h}\right)\nabla^2\Psi + [V_0 + U(r_e - r_h)]\Psi = E_t\Psi. \quad (2-3)$$

We take $r = r_e - r_h$ and $R = \frac{m_e r_e + m_h r_h}{m_e m_h}$, then the equation becomes

$$\left[-\frac{\hbar^2}{2M}\nabla_R^2 - \frac{\hbar^2}{2\mu}\nabla_r^2 + V(R) + U(r)\right]\Psi = E_t\Psi$$

with $M = m_e + m_h$, $\mu = \frac{m_e m_h}{m_e + m_h}$, and E_t as the total energy of the system. If we

take $\Psi = \phi(R)\varphi(r)$ and consider Coulomb interaction first, then we get

$$\begin{aligned} \left[-\frac{\hbar^2}{2M}\nabla_R^2 + V(R)\right]\phi(R) &= E_c\Psi, \\ \left[-\frac{\hbar^2}{2\mu}\nabla_r^2 + U(r)\right]\varphi(r) &= (E_t - E_c)\varphi(r) = E_{ex}\varphi(r). \end{aligned}$$

Here E_{ex} results from the inclusion of Coulomb interaction. Then we consider the confinement potential

$$V(R) = 0, R \leq a$$

$$V(R) = \infty, R > a$$

Thus, the energy is

$$E_{cn} = \frac{\hbar^2 \pi^2 n^2}{2Ma^2}, n = 1, 2, 3, \dots$$

and the absorption energy of a photon is

$$\hbar\omega_0 = E_t = E_c - E_{ex} = E_g + \frac{\hbar^2 \pi^2}{2Ma^2} - E_{ex} \quad (2-4)$$

with $M = m_e + m_h$ as the total mass of the electron and hole.

2.2.1.2 Strong confinement

The size quantization band states of the electron and hole dominates for the kinetic energies of electron and hole are larger than the electron-hole Coulomb potential, and the effect of the Coulomb attraction between the electron and hole can be treated as a perturbation. Then the Schrödinger equation becomes

$$\left(-\frac{\hbar^2}{2m_e} - \frac{\hbar^2}{2m_h}\right)\nabla^2\Psi + V_0\Psi = E\Psi.$$

The potential is defined as

$$V(r) = 0, r \leq a$$

$$V(r) = \infty, r > a$$

and the energy of a electron or hole is

$$E_{cn} = \frac{\hbar^2 \pi^2 n^2}{2m_{e,h}a^2}, n = 1, 2, 3, \dots$$

The absorption energy of a photon is

$$\hbar\omega_0 = E_g + \frac{\hbar^2\pi^2}{2a^2}\left(\frac{1}{m_e} + \frac{1}{m_h}\right) = E_g + \frac{\hbar^2\pi^2}{2a^2\mu} \quad (2-5)$$

with $\mu = \frac{m_e m_h}{m_e + m_h}$ as the reduced mass of electron and hole.

2.3.1 Density of states (DOS)

The concept of density of states (DOS) is extremely powerful. Important physical properties such as optical absorption, transport, etc., are intimately dependent upon this concept. The density of states is the number of available electronic states per unit volume per unit energy interval around an energy E. If we denote the density of states by $N(E)$, the number of states in an energy interval dE around an energy E is $N(E)dE$. To calculate the density of states, we need to know the dimensionality of the system and the energy vs. wave vector relation or the dispersion relation that the electrons obey.

2.3.2.1 Density of state for a three-dimensional system

In a three dimension system, the k-space volume between vector k and $k + dk$ is $4\pi k^2 dk$. Therefore, the number of states of electron in the region between k and $k+ dk$ are

$$\frac{4\pi k^2 dk}{8\pi^3} V = \frac{k^2 dk}{2\pi^2} V.$$

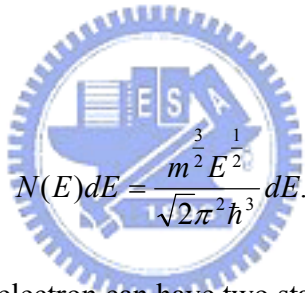
Denoting the energy and energy interval corresponding to k and dk as E and dE , we see that the number of electron states between E and $E + dE$ per unit volume is

$$N(E)dE = \frac{k^2 dk}{2\pi^2}$$

and since $E = \frac{\hbar^2 k^2}{2m}$, then the equation becomes

$$k^2 dk = \frac{\sqrt{2} m^{\frac{3}{2}} E^{\frac{1}{2}} dE}{\hbar^3},$$

which gives



$$N(E)dE = \frac{m^{\frac{3}{2}} E^{\frac{1}{2}}}{\sqrt{2}\pi^2 \hbar^3} dE.$$

We must remember that the electron can have two states for a given k -value since it can have a spin state of $s = 1/2$ or $-1/2$. Accounting for spin, the density of states is

$$N(E) = \frac{\sqrt{2} m^{\frac{3}{2}} E^{\frac{1}{2}}}{\pi^2 \hbar^3}.$$

2.3.2.2 Density of states for lower-dimensional systems

If we consider a 2-D system, a concept that has become a reality with use of quantum wells, similar arguments tell us that the density of states for a parabolic band is

$$N(E) = \frac{m}{\pi\hbar^2}.$$

Finally, in a 1-D system or “quantum wire”, the density of states is

$$N(E) = \frac{\sqrt{2m^{\frac{1}{2}}E^{-\frac{1}{2}}}}{\pi\hbar}.$$

We notice that as the dimensionality of the system changes, the energy dependence of the density of states also changes. In three-dimensional systems we have a $E^{1/2}$ -dependence. In 2-D systems there is no energy dependence, while in 1-D systems, the density of states has a peak at $E=0$. The variations related to dimensionality are extremely important and is a key driving force to lower dimensional systems.



2.4 Tight Binding Method for wurtzite structure

2.4.1 The unit cell of wurtzite structure

The wurtzite unit cell contains four atoms, two anions, and two cations, as shown in Fig. 2-9 (a). The basis vectors \vec{t}_1 , \vec{t}_2 , \vec{t}_3 , and \vec{t}_4 are $(0,0,0)$, $(a/\sqrt{3},0,c/2)$, $(a/\sqrt{3},0,c/8)$, and $(0,0,5c/8)$, where a is the length of a hexagonal side and c is the repeat distance along the z direction. The anions are at \vec{t}_1 , and \vec{t}_2 ; the cations are at \vec{t}_3 , and \vec{t}_4 . The reciprocal lattice, shown in Fig. 2-9 (b), is also hexagonal. The direct lattice vectors are defined as $\vec{a} = (\sqrt{3}a/2, -a/2, 0)$, $\vec{b} = (0, a, 0)$ and

$\vec{c} = (0,0,c)$, and the reciprocal-lattice vectors are

$$\vec{b}_a = (4\pi/\sqrt{3}a,0,0), \vec{b}_b = (2\pi/\sqrt{3}a,2\pi/a,0), \text{ and } \vec{b}_c = (0,0,2\pi/c)$$

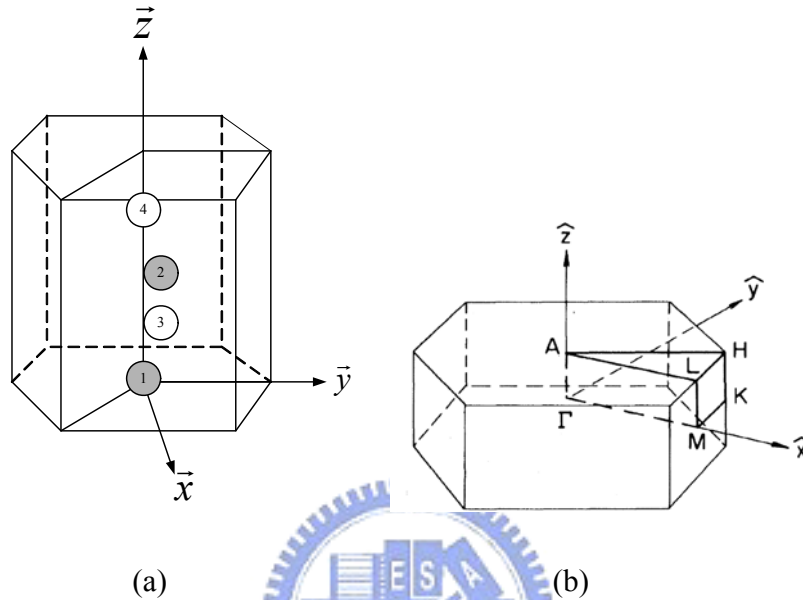


Fig. 2-9 (a) Hexagonal close-packed structure with four basis atoms, where 1 and 2 are anions, 3 and 4 are cations. (b) The reciprocal lattice. The symmetry points of the Brillouin zone are $\Gamma=(0,0,0)$, $K=(2\pi/a)$

$(1/\sqrt{3}, 1/3, 0)$, $M=(2\pi/a)(1/\sqrt{3}, 0, 0)$, $A=(2\pi/c)(0,0,1/2)$, $H=(2\pi/a)(1/\sqrt{3}, 1/3, a/2c)$, $M=(2\pi/a)(1/\sqrt{3}, 0, a/2c)$.

2.4.2 The Hamiltonian

We assume an sp^3 basis centered at each of the four atomic sites per unit cell, (namely, one s orbital and three p orbitals per site), leading to a $16N \times 16N$ Hamiltonian, where N is the number of unit cells. We limit the number of nonzero tight-binding

parameters to one-center on-site integrals and the nearest-neighbor two-center integrals, as discussed by Slater and Koster [48]. We treat the four nearest-neighbor atoms as equivalent ones, even though the crystal is not cubic (that has a negligible effect on the energy levels of localized perturbations [49]). The small crystal-field splittings which differentiate between the p_z orbital and the p_x and p_y orbitals are neglected (they are due to the second-nearest neighbors and more distant neighbors). Thus the model has nine independent parameters: the four on-site matrix elements $E(s,a)$, $E(p,a)$, $E(s,c)$, and $E(p,c)$ (where s and p refer to the basis states, and a and c refer to anion and cation), and five nearest-neighbor transfer matrix elements $V(ss\sigma)$, $V(sp\sigma)$, $V(ps\sigma)$, $V(pp\pi)$, and $V(pp\sigma)$, where the orientation of the p orbitals are denoted by σ and π , and the first (second) index refers to the anion (cation). In the development that follows, we consider the true C_{3v} symmetry, so that the simplifications can be easily relaxed, if desired.

For each wave vector \vec{k} , we construct the following Bloch-type linear combination of localized orbitals

$$|n,b,\vec{k}\rangle = N^{-1/2} \sum_{\vec{R}} \exp[i\vec{k} \cdot (\vec{R} + \vec{t}_b)] |n,b,\vec{R}\rangle, \quad (2-6)$$

where $|n,b,\vec{R}\rangle$ is a localized wave function centered at the site $\vec{R} + \vec{t}_b$ ($b=1, 2, 3, \text{ or } 4$ for the four atoms in a unit cell was shown in Fig. 2-9 (a), and $n=s, p_x, p_y, \text{ or } p_z$). The

crystal eigenstates are linear combination of the above Bloch-type basis states,

$$|\vec{k}, \lambda\rangle = \sum_{n,b} |n, b, \vec{k}\rangle \langle n, b, \vec{k} | \vec{k}, \lambda\rangle. \quad (2-7)$$

The corresponding Schrödinger equation in a Bloch-type basis can be written as

$$\sum_{m,b'} [\langle n, b, \vec{k} | H | m, b', \vec{k}\rangle - \varepsilon(\vec{k}, \lambda) \delta_{n,m} \delta_{b,b'}] \langle m, b', \vec{k} | \vec{k}, \lambda\rangle = 0, \quad (2-8)$$

where we have

$$\langle n, b, \vec{k} | H | m, b', \vec{k}\rangle = \sum_{\vec{R}} \exp[i\vec{k} \cdot (\vec{R} + \vec{t}_b - \vec{t}_{b'})] \langle n, b, \vec{0} | H | m, b', \vec{R}\rangle. \quad (2-9)$$

We have taken the overlaps of localized orbitals centered on different sites to be zero and

we will now assume that only the Hamiltonian matrix elements between orbitals centered on the same atom or between the nearest-neighbor atoms are nonzero.

In the $|n, b, \vec{k}\rangle$ basis, the perfect-crystal Hamiltonian, using the C_{3v} point-group symmetry of each site, is the 16×16 matrix

$$b \setminus b' \begin{matrix} 1 & 2 & 3 & 4 \\ \begin{pmatrix} \underline{E}_a & \underline{0} & \underline{H}_{1,3} & \underline{H}_{1,4} \\ \underline{0} & \underline{E}_a & \underline{H}_{1,4} & \underline{H}_{2,4} \\ \underline{H}_{1,3}^+ & \underline{H}_{1,4}^+ & \underline{E}_c & \underline{0} \\ \underline{H}_{1,4}^+ & \underline{H}_{2,4}^+ & \underline{0} & \underline{E}_c \end{pmatrix} \end{matrix}.$$

Each element of this matrix is a 4×4 matrix. The on-site matrix for the anions (atoms 1 and 2) is

$$\underline{E}_a = \begin{matrix} & |s,1\rangle & |p_z,1\rangle & |p_x,1\rangle & |p_y,1\rangle \\ \begin{matrix} \langle s,1| \\ \langle p_z,1| \\ \langle p_x,1| \\ \langle p_y,1| \end{matrix} & \begin{pmatrix} E(s,a) & E(s,p_z,a) & 0 & 0 \\ E(s,p_z,a) & E(p_z,a) & 0 & 0 \\ 0 & 0 & E(p_x,a) & 0 \\ 0 & 0 & 0 & E(p_y,a) \end{pmatrix} \end{matrix}$$

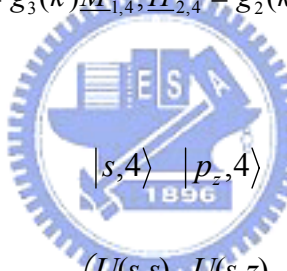
where $E(s,p_z,a)$ is taken to be zero and $E(p_z,a)=E(p_x,a)=E(p_y,a)$, in the approximation that

the local environment is tetrahedral. The on-site matrix \underline{E}_c for cation atoms **3** and **4** is

the same in form as the above matrix \underline{E}_a except that c replaces a everywhere.

The off-site matrices are $\underline{H}_{1,4} = g_3(\vec{k})\underline{M}_{1,4}$, $\underline{H}_{2,4} = g_2(\vec{k})\underline{M}_{2,4}$, and $\underline{H}_{1,3} = g_1(\vec{k})\underline{M}_{1,3}$,

where we have



$$\underline{M}_{1,4} = \begin{matrix} & |s,4\rangle & |p_z,4\rangle & |p_x,4\rangle & |p_y,4\rangle \\ \begin{matrix} \langle s,1| \\ \langle p_z,1| \\ \langle p_x,1| \\ \langle p_y,1| \end{matrix} & \begin{pmatrix} U(s,s) & U(s,z) & 0 & 0 \\ U(z,s) & U(z,z) & 0 & 0 \\ 0 & 0 & U(x,x) & 0 \\ 0 & 0 & 0 & U(x,x) \end{pmatrix} \end{matrix}$$

$$\underline{M}_{2,4} = \begin{matrix} & |s,4\rangle & |p_z,4\rangle & |p_x,4\rangle & |p_y,4\rangle \\ \begin{matrix} \langle s,2| \\ \langle p_z,2| \\ \langle p_x,2| \\ \langle p_y,2| \end{matrix} & \begin{pmatrix} f_0^*U(s,s) & f_0^*U(s,z) & -f_1^*U(s,x) & (-\sqrt{3}/2)f_1^*U(s,x) \\ f_0^*U(z,s) & f_0^*U(z,z) & -f_1^*U(z,x) & (-\sqrt{3}/2)f_1^*U(z,x) \\ -f_1^*U(x,s) & -f_1^*U(x,z) & f_1^*U(x,x)+(3/4)f_1^*[U(x,x)+U(y,y)] & (-\sqrt{3}/4)f_1^*[U(x,x)-U(y,y)] \\ (-\sqrt{3}/2)f_1^*U(x,s) & (-\sqrt{3}/2)f_1^*U(x,z) & (-\sqrt{3}/4)f_1^*[U(x,x)-U(y,y)] & f_1^*U(y,y)+(3/4)f_1^*[U(x,x)+U(y,y)] \end{pmatrix} \end{matrix}$$

$$\underline{\mathbf{M}}_{I,3} = \begin{matrix} & |s,3\rangle & |p_z,3\rangle & |p_x,3\rangle & |p_y,3\rangle \\ \begin{matrix} \langle s,1| \\ \langle p_z,1| \\ \langle p_x,1| \\ \langle p_y,1| \end{matrix} & \begin{pmatrix} f_0 U(s,s) & f_0 U(s,z) & -f_1 U(s,x) & (-\sqrt{3}/2) f_- U(s,x) \\ f_0 U(z,s) & f_0 U(z,z) & -f_1 U(z,x) & (-\sqrt{3}/2) f_- U(z,x) \\ -f_1 U(x,s) & -f_1 U(x,z) & f_1 U(x,x) + (3/4) f_+ [U(x,x) + U(y,y)] & (-\sqrt{3}/4) f_- [U(x,x) - U(y,y)] \\ (-\sqrt{3}/2) f_- U(x,s) & (-\sqrt{3}/2) f_- U(x,z) & (-\sqrt{3}/4) f_- [U(x,x) - U(y,y)] & f_1 U(y,y) + (3/4) f_+ [U(x,x) + U(y,y)] \end{pmatrix} \end{matrix}$$

and

$$g_1(\vec{k}) = \exp[i(-k_1/3 + k_2/3 + k_3/8)],$$

$$f_0(\vec{k}) = \exp(ik_1) + 1 + \exp(-ik_2),$$

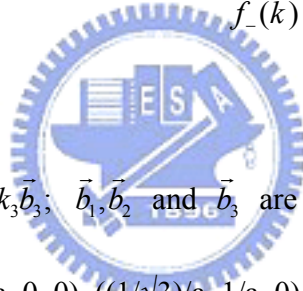
$$g_2(\vec{k}) = \exp[i(k_1/3 - k_2/3 + k_3/8)],$$

$$f_1(\vec{k}) = \exp(ik_1) - \frac{1}{2} - \left(\frac{1}{2}\right) \exp(-ik_2),$$

$$g_3(\vec{k}) = \exp(-ik_3/8),$$

$$f_+(\vec{k}) = 1 + \exp(-ik_2),$$

$$f_-(\vec{k}) = 1 - \exp(-ik_2).$$



Here we have $\vec{k} = k_1 \vec{b}_1 + k_2 \vec{b}_2 + k_3 \vec{b}_3$; \vec{b}_1, \vec{b}_2 and \vec{b}_3 are the reciprocal-lattice vectors divided by 2π , namely, $((2/\sqrt{3})/a, 0, 0)$, $((1/\sqrt{3})/a, 1/a, 0)$, and $(0, 0, 1/c)$, respectively.

The parameters used above are matrix elements of H between localized orbitals

$|n, b, \vec{R}\rangle$. For example, we have

$$E(s, a) = \langle s, 1, \vec{R} | H | s, 1, \vec{R} \rangle = \langle s, 2, \vec{R} | H | s, 2, \vec{R} \rangle,$$

$$E(s, p_z, c) = \langle s, 3, \vec{R} | H | p_z, 3, \vec{R} \rangle = \langle s, 4, \vec{R} | H | p_z, 4, \vec{R} \rangle,$$

$$U(x, x) = \langle p_x, 1, \vec{R} | H | p_x, 4, (\vec{R} - \vec{c}) \rangle,$$

and

$$U'(z, z) = \langle p_z, 1, \vec{R} | H | p_z, 3, \vec{R} \rangle,$$

Following Vogl *et al.* [50], we take the difference between the anion and cation s

and p on-site matrix elements of the Hamiltonian to be proportional to the difference in neutral free-atom Hartree-Fock orbital energies $w(s, a)$, $w(s, c)$, $w(p, a)$, and $w(p, c)$. Empirical tight-binding Hamiltonians such as this are especially useful if their matrix elements exhibit manifest chemical trends. In the present model, the differences of diagonal matrix elements are required to satisfy the rule deduced by Vogl *et al.* [50] that are proportional to the corresponding differences in atomic orbital energies,

$$E(l, a) - E(l, c) = \beta_l [w(l, a) - w(l, c)],$$

where l specifies s or p orbitals.

The remaining off-diagonal matrix elements U and U' are then expected to be nearly independent of the chemical elements in the semiconductor and to scale with bond length d according to Harrison's d^{-2} rule [51], i.e., $U \sim d^{-2}$. The expected scaling is indeed found for principal matrix elements (Fig. 2-10).

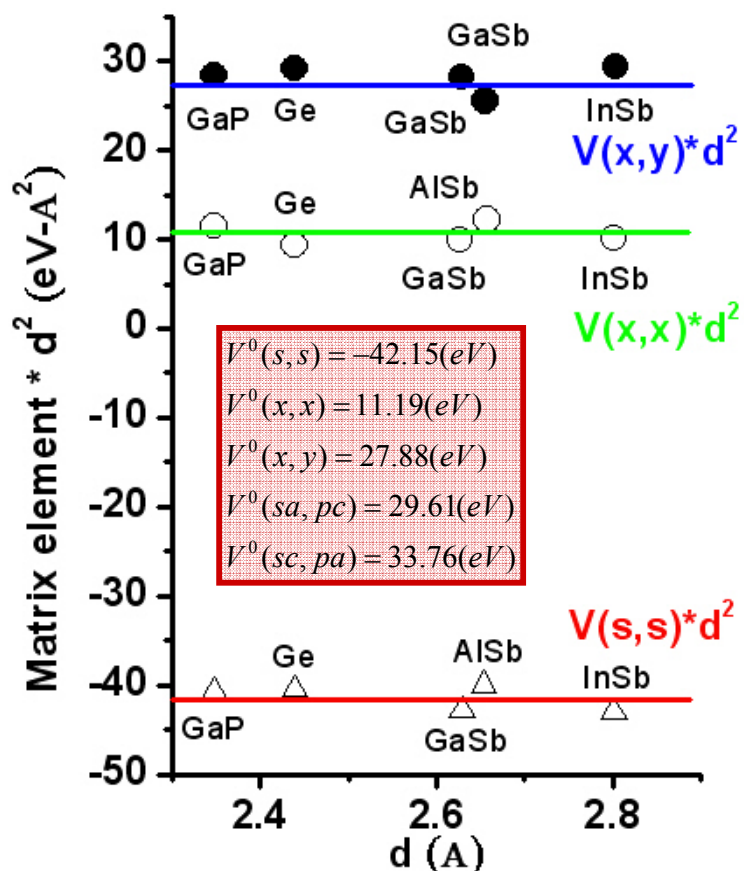


Fig. 2-10 Inter-atomic matrix elements $V(s,s)$, $V(x,x)$, and $V(x,y)$ (in eV) multiplied by the square of the bond length vs. the bond length d (in \AA).

References

1. Ü. Özgür, Ya. I. Alivov, C. Liu, A. Teke, M. A. Reshchikov, S. Doğan, V. Avrutin, S.-J. Cho, and H. Morkoç, *J. Appl. Phys.* **98**, 041301 (2005).
2. R. Loudon, *Adv. Phys.* **50**, 813 (2001).
3. M. A. Stroschio and M. Dutta, “*Phonons in Nanostructures*” (Cambridge university press, United Kingdom 2001).
4. J. F. Nye, “*Physical properties of crystals*” (Oxford: Clarendon press 1957).
5. H. Poulet and J. P. Mathieu, “*Vibration spectra and symmetry of crystal*” (Paris: Gordon and Breach 1976).
6. W. Hayes and R. Loudon, “*Scattering of light by crystals*” (John Wiley and Sons, New York 1978).
7. J. M. Calleja and M. Cardona, *Phys. Rev. B* **16**, 3753 (1997).
8. A. P. Jephcoat, R. J. Hemley, H. K. Mao, R. E. Cohen, and M. J. Mehl, *Phys. Rev. B* **37**, 4727 (1988).
9. J. Grabowska, A. Meaney, K. K. Nanda, J.-P. Mosnier, M. O. Henry, J.-R. DuclQre, and E. McGlynn, *Phys. Rev. B* **71**, 115439 (2005).
10. S. Chen, Y. Liu, C. Shao, R. Mu, Y. Lu, J. Zhang, D. Shen, and X. Fan, *Adv. Mater.* **17**, 586 (2005).

11. H. C. Hsu and W. F. Hsieh, *Solid State Commun.* **131**, 371 (2004).
12. J. Jie, G. Wang, Y. Chen, X. Han, Q. Wang, B. Xu, and J. G. Hou, *Appl. Phys. Lett.* **86**, 031909 (2005).
13. B. P. Zhang, N. T. Binh, Y. Segawa, K. Wakatsuki, and N. Usami, *Appl. Phys. Lett.* **83**, 1635 (2003).
14. B. K. Meyer, H. Alves, D. M. Hofmann, W. Kreigseis, D. Forster, F. Bertram, J. Christen, A. Hoffmann, M. Strassburg, M. Dworzak, U. Haboek, and A. V. Rodina, *Phys. Stat. Sol. B* **241**, 231 (2004).
15. A. Teke, D. EzgFr, S. Dog~an, X. Gu, H. MorkoA, B. Nemeth, J. Nause, and H. O. Everitt, *Phys. Rev. B* **70**, 195207 (2004).
16. J. Gutowski, N. Presser, and I. Broser, *Phys. Rev. B* **38**, 9746 (1988).
17. M. Strassburg, A. Rodina, M. Dworzak, U. Haboek, I. L. Krestnikov, A. Hoffmann, O. Gelhausen, M. R. Phillips, H. R. Alves, A. Zeuner, D. M. Hofmann, and B. K. Meyer, *Phys. Stat. Sol. B* **241**, 607 (2004).
18. K. Thonke, T. Gruber, N. Teofoliv, R. Schenfelder, A. Waag, and R. Sauer, *Physica B* **308**, 945 (2001).
19. D. C. Look, C. Cos · kun, B. Claflin, G. C. Farlow, *Physica B* **32**, 340 (2003).
20. A. Kobayashi, O. F. Sankey, J. D. Dow, *Phys. Rev. B* **28**, 946 (1983).

21. D. C. Look, R. L. Jones, J. R. Sizelove, N. Y. Garces, N. C. Giles, L. E. Halliburton, Phys. Stat. Sol. A **195**, 171 (2003).
22. H. J. Ko, Y. F. Chen, T. Yao, K. Miyajima, A. Yamamoto, and T. Goto, Appl. Phys. Lett. **77**, 537 (2000).
23. C. J. Pan, K. F. Lin and W. F. Hsieh, Appl. Phys. Lett. **91**, 111907 (2007).
24. Y. Harada, H. Kondo, N. Ichimura, S. Hashimoto, and J. Lumin. **405**, 87 (2000).
25. M. Haupt, A. Ladenburger, R. Sauer, K. Thonke, R. Glass, W. Roos, J. P. Spatz, H. Rauscher, S. RiethmFller, and M. Meller, J. Appl. Phys. **93**, 6252 (2003).
26. H. J. Ko, Y. Chen, S. K. Hong, and T. Yao, J. Cryst. Growth. **209**, 816 (2000).
27. Y. Gu, I. L. Kuskovsky, M. Yin, S. O'Brien, G. F. Neumark, Appl. Phys. Lett. **85**, 3833 (2004).
28. W. Gcpel, U. Lampe, Phys. Rev. B. **22**, 6447 (1980).
29. A. B. Djurisic and Y. H. Leung, small. **2**, 944 (2006).
30. A. Kobayashi, O. F. Sankey, J. D. Dow, Phys. Rev. B. **28**, 946 (1983).
31. B. Lin, Z. Fu, Y. Jia, Appl. Phys. Lett. **79**, 943 (2001).
32. M. H. Huang, Y. Wu, H. Feick, N. Tran, E. Weber, and P. Yang, Adv. Mater. **13**, 113 (2001).
33. H. T. Ng, B. Chen, J. Li, J. Han, M. Meyyappan, J. Wu, S. X. Li, and E. E. Haller,

- Appl. Phys. Lett. **82**, 2023 (2003).
34. X. Liu, X. Wu, H. Cao, R. P. H. Chang, J. Appl. Phys. **95**, 3141 (2004).
35. C. X. Xu, X.W. Sun, X. H. Zhang, L. Ke, S. J. Chua, Nanotechnology **15**, 856 (2004).
36. A. van Dijken, E. Meulenkamp, D. Vanmaekelbergh, and A. Meijerink, J. Phys. Chem. B **104**, 1715 (2000).
37. Q. X. Zhao, P. Klason, M. Willander, H. M. Zhong, W. Lu, and J. H. Yang, Appl. Phys. Lett. **87**, 211912 (2005).
38. A. B. Djurisic, W. C. H. Choy, V. A. L. Roy, Y. H. Leung, C. Y. Kwong, K.W. Cheah, T. K. Gundu Rao, W. K. Chan, H. F. Lui, and C. Surya, Adv. Funct. Mater. **14**, 856 (2004).
39. Q. X. Zhao, P. Klason, M. Willander, H. M. Zhong, W. Lu, J. H. Yang, Appl. Phys. Lett. **87**, 211912 (2005).
40. N. E. Hsu, W. K. Hung, Y. F. Chen, Appl. Phys. Lett. **96**, 4671 (2004).
41. L. E. Greene, M. Law, J. Goldberger, F. Kim, J. C. Johnson, Y. Zhang, R. J. Saykally, and P. Yang, Angew. Chem. **115**, 3030 (2003); Angew. Chem. Int. Ed. **42**, 3031 (2003).
42. D. Li, Y. H. Leung, A. B. Djurisic, Z. T. Liu, M. H. Xie, S. L. Shi, S. J. Xu, and W.

- K. Chan, Appl. Phys. Lett. 85, 1601 (2004).
43. H. J. Fan, R. Scholz, F. M. Kolb, and M. Zacharias, Appl. Phys. Lett. **85**, 4142 (2004).
44. R. B. M. Cross, M. M. De Souza, and E. M. Sankara Narayanan, Nanotechnology **16**, 2188 (2005).
45. S. M. Abrarov, Sh. U. Yuldashev, T.W. Kim, S. B. Lee, Y. H.Kwon, and T.W. Kang, Opt. Commun. **250**, 111 (2005).
46. C. F. Klingshirn, "*Semiconductor Optics*", p.169. (1997).
47. Sun-Bin Yin, "*Fabrication and Characterization of CdS and ZnSe Microcrystalline Doped Glass Thin Films by Pulsed Laser Deposition*", p.7. National Chiao Tung University Department of Photonics, (1999).
48. J. C. Slater and G. F. Koster, Phys. Rev. **94**, 1498 (1954).
49. A. Kobayashi, O. F. Sankey, and J. D. Dow, Phys. Rev. B **28**, 946 (1983).
50. P. Vogl, H. P. Hjalmarson, and J. D. Dow, J. Phys. Chem. Solids **44**, 365 (1983).
51. W. A. Harrison, Phys. Rev. B **16**, 790 (1977).

Chapter 3 Experiment details and analysis techniques

ZnO QDs have been obtained by metalorganic vapor-phase epitaxy (MOCVD) [1, 2], pulsed laser deposition [3], and vapor phase transport (VPT) deposition process [4, 5] techniques, etc. However, these methods are expensive and require high vacuum and formation controlling conditions. Compared with these methods, the sol-gel process is an attractive technique for compound semiconductors preparation because of its simplicity, low cost, and ease of composition control [6, 7]. In particular, it has the potential to produce samples with large areas and complicated forms on various substrates. In this research, the sol-gel method was used to fabricate ZnO QDs. The detailed growth mechanisms and characterization techniques of the ZnO QDs are discussed as follows.

3.1 Experiment details

3.1.1 Synthesis mechanism of sol-gel method

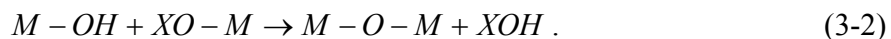
A colloid is a suspension in which the dispersed phase is so small (~1-1000nm) that the gravitation force is negligible and the interactions are dominated by the short-range forces, such as van der Waals attraction and surface charge. The precursors were mixed together and heated at high temperature. This procedure has to be repeated several

times until a homogeneous product is obtained. Then, the materials have to be transformed into the desired shape. Sol-gel synthesis has two ways to prepare solution. One way is the metal-organic route with metal alkoxides in organic solvent; the other way is the inorganic route with metal salts in aqueous solution. It is much cheaper and easier to handle than metal alkoxides, but their reactions are more difficult to control. The inorganic route is a step of polymerization reactions through hydrolysis and condensation of metal alkoxides $M(OR)^Z$, where $M = Si, Ti, Zr, Al, Sn, Ce$, and OR is an alkoxy group and Z is the valence or the oxidation state of the metal. First, hydroxylation upon the hydrolysis of alkoxy groups:



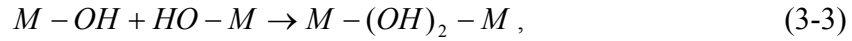
The second step, polycondensation process leads to the formation of branched oligomers and polymers with a metal oxygenation based skeleton and reactive residual hydroxyl and alkoxy groups. There are 2 competitive mechanisms:

(1) *Oxolation*-- formation of oxygen bridges:



The hydrolysis ratio ($h = H_2O/M$) decides $X=H$ ($h \gg 2$) or $X = R$ ($h < 2$).

(2) *Olation*-- formation of hydroxyl bridges when the coordination of the metallic center is not fully satisfied ($N - Z > 0$):



where X = H or R. The kinetics of ololation is usually faster than those of oxolation.

Figure 3-1 presents a schematic of the routes that one could follow within the scope of sol-gel processing [8].

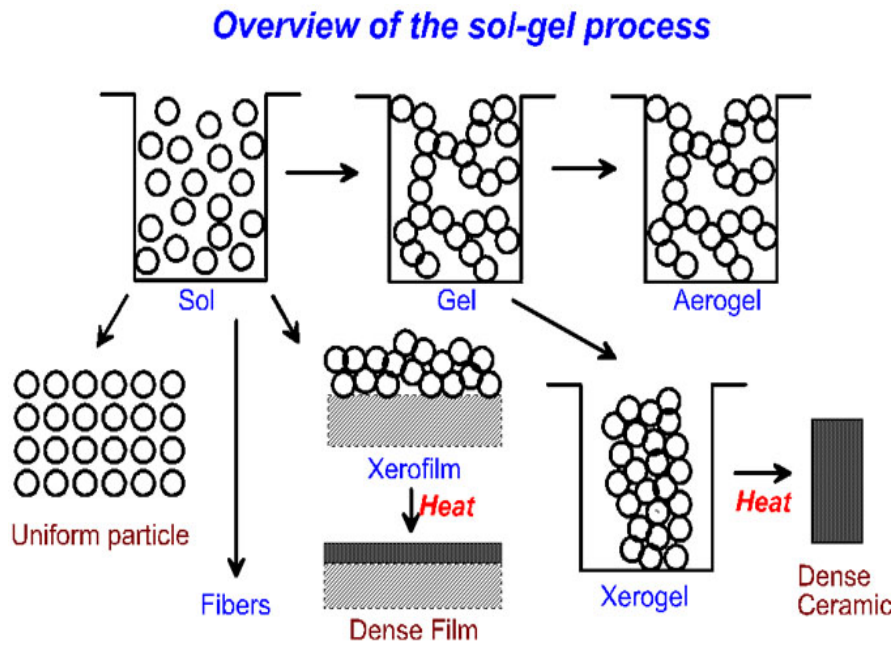


Fig. 3-1 Schematic of the routes that one could follow within the scope of sol-gel processing [8].

A sol is a colloidal suspension of solid particles in a liquid. An aerosol is a colloidal suspension of particles in a gas (the suspension may be called a fog if the particles are liquid and a smoke if they are solid) and an emulsion is a suspension of liquid droplets in another liquid. All of these types of colloids can be used to generate polymers or particles from which ceramic materials can be made. In the sol-gel process,

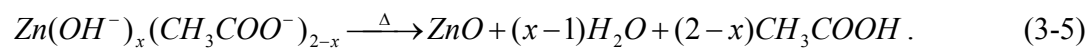
the precursors (starting compounds) for preparation of a colloid consist of a metal or metalloid element surrounded by various ligands. For example, an alkyl is a ligand formed by removing one hydrogen (proton) from an alkane molecule to produce, for example, methyl ($\cdot \text{CH}_3$) or ethyl ($\cdot \text{C}_2\text{H}_5$). An alcohol is a molecule formed by adding a hydroxyl (OH) group to an alkyl (or other) molecule, as in methanol (CH_3OH) or ethanol ($\text{C}_2\text{H}_5\text{OH}$).

Metal alkoxides are members of the family of metalorganic compounds, which have an organic ligand attracted to a metal or metalloid atom. Metal alkoxides are popular precursors because they react readily with water. The reaction is called hydrolysis, because a hydroxy ion becomes attached to the metal atom. This type of reaction can continue to build larger and larger molecules by the process of polymerization. A polymer is a huge molecule (also called a macromolecule) formed from hundreds or thousands of units called monomers. If one molecule reaches macroscopic dimensions so that it extends throughout the solution, the substance is said to be gel. The gel point is the time (or degree of reaction) when the last bound is formed that completes this giant molecule. It is generally found that the process begins with the formation of fractal aggregates that begin to impinge on one another, then those clusters link together as described by the theory of percolation. The gel point corresponds to the percolation

threshold, when a single cluster (call the spanning cluster) appears that extends throughout the sol; the spanning cluster coexists with a sol phase containing many smaller clusters, which gradually become attached to the network. Gelation can occur after a sol is cast into a mold, in which it is possible to make objects of a desired shape.

3.1.2 Sample preparation

We produce monodisperse ZnO colloidal spheres by sol-gel method. Sol-gel method was chosen due to its simple handling and narrow size distribution. The ZnO colloidal spheres were produced by an one-stage reaction process similar to that described by Seelig et al [9], and reactions were described as the following equations:



Equation (3-4) is the hydrolysis reaction for Zn(OAc)₂ to form metal complexes. We increased the temperature of reflux from RT to 160°C and maintained for aging. The zinc complexes will dehydrate and remove acetic acid to form pure ZnO as Eq. (2) during the aging time. Actually, the two reactions described above proceed simultaneously while the temperature is over 110°C.

All chemicals used in this study were reagent grade and employed without further

purification. A typical reaction was listed in Table 3-1, zinc acetate dihydrate (99.5% Zn(OAc)₂, Riedel-deHaen) was added to diethylene glycol (99.5% DEG, EDTA). The first thing we notice is that we can control the QDs size with domination concentration of zinc acetate in the solvent (DEG). This point will be examined later.

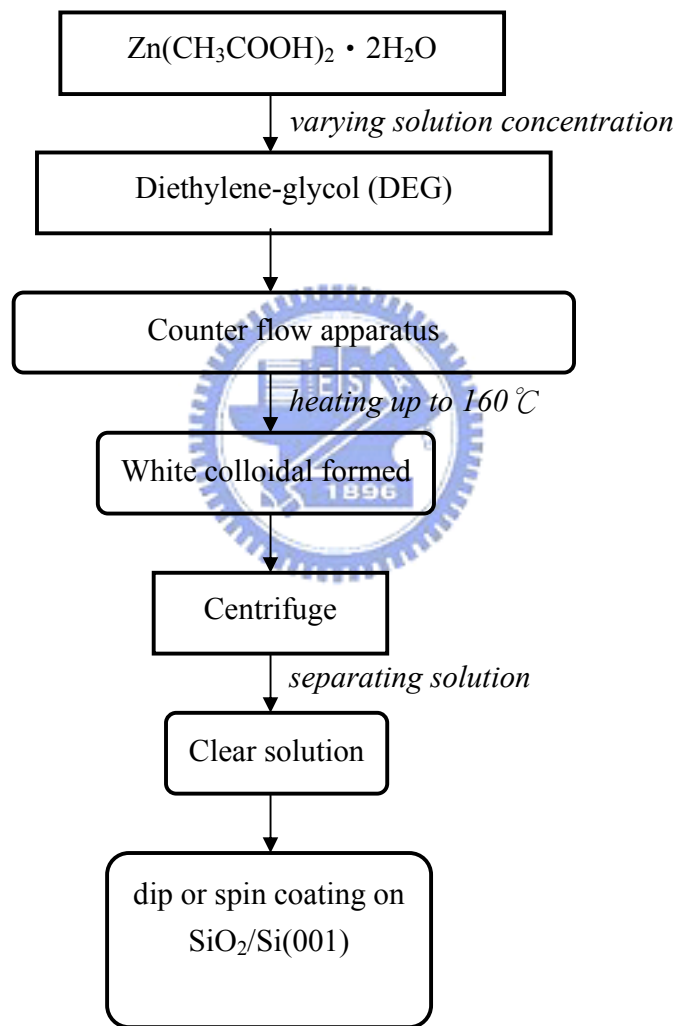
Table 3-1 Shows that chemical reagent was used with sol-gel experiment process

Chemical reagent	Molecular formula	Degree of purity	Source
Zinc acetate dehydrate	Zn(CH ₃ COOH) ₂ · 2H ₂ O	99.5%	Riedel-deHaen
Diethylene glycol	C ₄ H ₁₀ O ₃	99.5%	EDTA

Then the temperature of reaction solution was increased to 160°C and maintained for different aging time. White colloidal ZnO was formed in the solution that was employed as the primary solution. Jezequel [10] et al., reported that this method produce monodisperse ZnO powders of various sizes with changing the heat rate of the reaction solution. A primary reaction was performed as described above, and the product was placed in a centrifuge. The supernatant (DEG, dissolved reaction products, and unreacted ZnAc and water) was decanted off and saved, and the polydisperse powder was discarded. Finally, the supernatant was then dipped on substrates (SiO₂/Si (001) or

SiO₂) and dried at 150°C. A flow chart of fabricate ZnO QDs by sol-gel method was shown in Table 3-2.

Table 3.2 A flow chart of fabricate ZnO QDs by sol-gel method.



3.2 Microstructure and lattice dynamics analysis

3.2.1 X-ray diffraction

The crystal structures of the as-grown powder were inspected by Bede D1 diffractometer at Industrial Technology Research Institute, Taiwan using a CuK X-ray source ($\lambda=1.5405\text{\AA}$). We used small angle diffraction. The ω was fixed at 5° , the scanning step was 0.04° , scanning rate was 4 degree/min and count time was 1.00 second. Figure 3-2 shown XRD ω - 2θ scans geometry. The dashed lines mean the trajectory of the incident beam and the detector to be in motion.

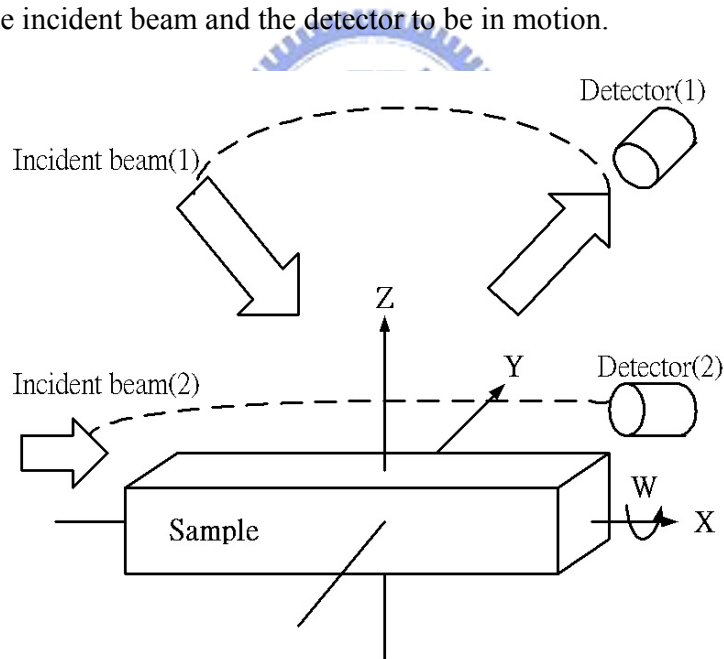


Fig. 3-2 XRD ω - 2θ scans geometry for ZnO nanoparticles.

The sizes of the nanocrystallites can be determined by X-ray diffraction using the

measurement of the full width at half maximum (FWHM) of the X-ray diffraction lines.

The average diameter is obtained by $D = \frac{0.89\lambda}{B \cos \theta}$, where D is the average diameter of the nanocrystallite, λ is the wavelength of the X-ray source, and B is the FWHM of X-ray diffraction peak at the diffraction angle θ .

3.2.2 Transmission electron microscope

The shapes and sizes of ZnO QDs were analyzed using JEOL JEM-2100F field emission transmission electron microscope (FETEM) operated at 200 KeV.



3.2.3 Raman scattering measurement

Raman scattering is a very powerful probe for investigating the vibration properties of materials. It is also influential in understanding problems as diverse as the structure of amorphous insulators, and the conduction mechanisms in ionic conductors. The experimental setup of Raman spectroscopy consists mainly of three components: a laser system serves as a powerful, monochromatic light source and a computer controlled spectrometer for wavelength analysis of the inelastically scattered light. Figure 3-3 shows the experimental setup schematically. The micro-Raman system was performed in the backscattering geometry with a confocal Olympus (BX-40) optical microscope.

The scattered light was dispersed through the triple-monochromator system and detected by a liquid-nitrogen-cooled charge coupled device (CCD). The 515 nm line of a frequency-doubled Yb^{3+} :YAG laser was used as the Raman excitation source. The best spatial resolution during Raman measurements was 1.0 μm with a spectral resolution of 0.2 cm^{-1} . Similarly, micro-Raman spectroscopy was measured with an Ar-ion laser (Coherent INNOVA 90) as an excitation source emitting at a wavelength of 488 nm. The scattered light was collected by a camera lens and imaged onto the entrance slit of the Spex 1877C. Light passes through the entrance (S1) to be collimated by M1 onto G1 where it is dispersed onto M2. After passing through S2, which acts as the filter stage to determine the pass band, the light strikes the spatial-filter mirror (M3) and passes through a fixed slit, which eliminates much of the stray light. Again the light is collimated (M4), dispersed (G2), in an opposing direction to cancel the effects of the initial dispersion, then focused (M5) onto the exit slit of the filter stage (S3) which controls the resolution of the next spectrograph stage. In this final stage, the light is again collimated (M6) and dispersed on whichever of the turreted gratings (G3, G4 and G5 as gratings of 600, 1200 and 1800 grooves/nm, respectively) is selected by the user. The camera mirror (M7) projects a flat image onto the focal plane where it is seen by CCD.

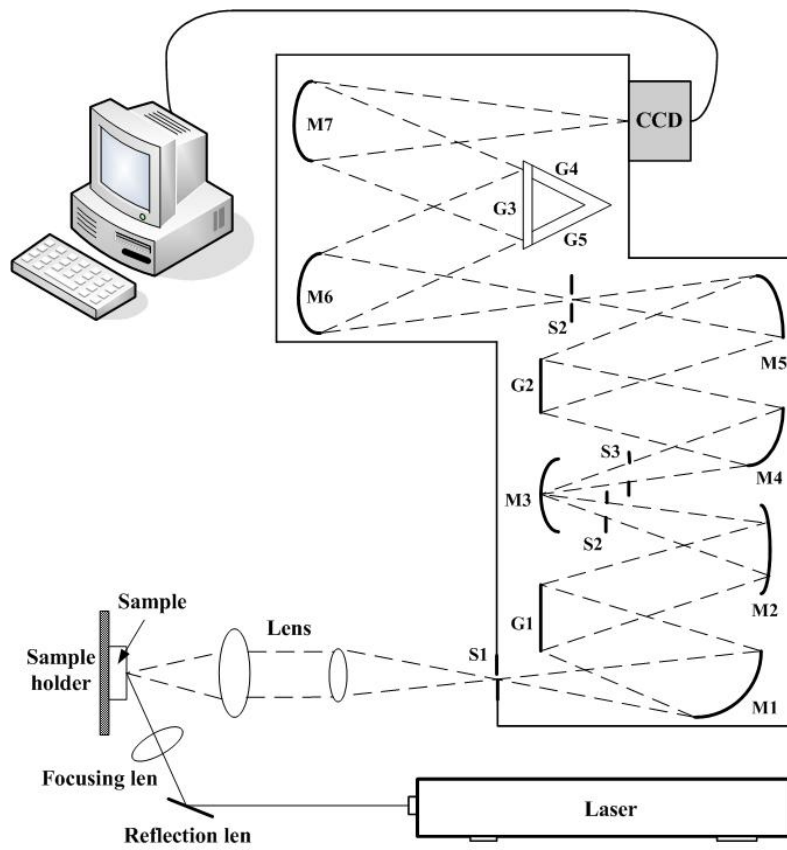


Fig. 3-3 Raman detection systems

3.3 Characterization of optical properties

3.3.1 Photoluminescence system

PL provides a non-destructive technique for the determination of certain impurities in semiconductors. The shallow-level and the deep-level of impurity states were detected by PL system. It was provided radiative recombination events dominate nonradiative recombination.

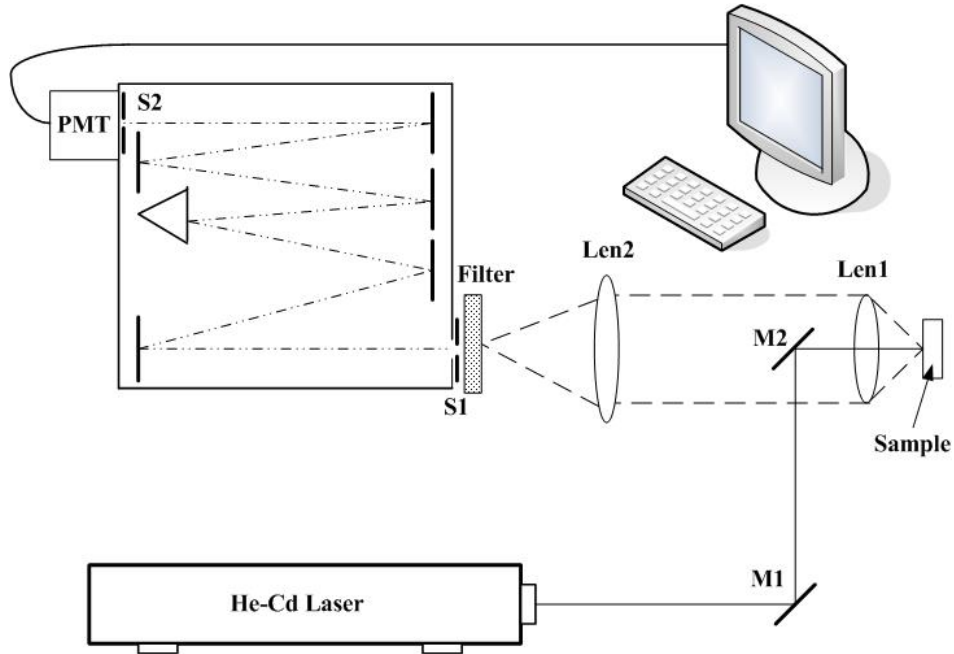


Fig. 3-4 PL detection systems

In the PL measurements, the 325 nm line from a He–Cd laser was used as the excitation light. Light emission from the samples was collected into the TRIAX 320 spectrometer and detected by a photomultiplier tube (PMT). As shown in Fig. 3-4, the diagram of PL detection system includes mirror, focusing and collecting lens, the sample holder and the cooling system. The excitation laser beam was directed normally and focused onto the sample surface with power being varied with an optical attenuator. The spot size on the sample is about 100 μm . Spontaneous and stimulated emissions were collected by a fiber bundle and coupled into a 0.32 cm focal-length monochromator (TRIAX 320) with a 1200 lines/mm grating, then detected by either an electrically cooled

CCD (CCD-3000) or a photomultiplier tube (PMT-HVPS) detector. The temperature-dependent PL measurements were carried out using a closed cycle cryogenic system. A closed cycle refrigerator was used to set the temperature anywhere between 15 K and 300 K.

3.3.2 Optical absorption system

Optical transmission or absorption measurements are routinely used by chemists to determine the constituents of chemical compounds. Optical absorption spectra were made using a deuterium lamp and the emission light was dispersed by a TRIAX-320 spectrometer and detected by a UV-sensitive PMT. Figure 3-5 is a schematic diagram showing the absorption system.

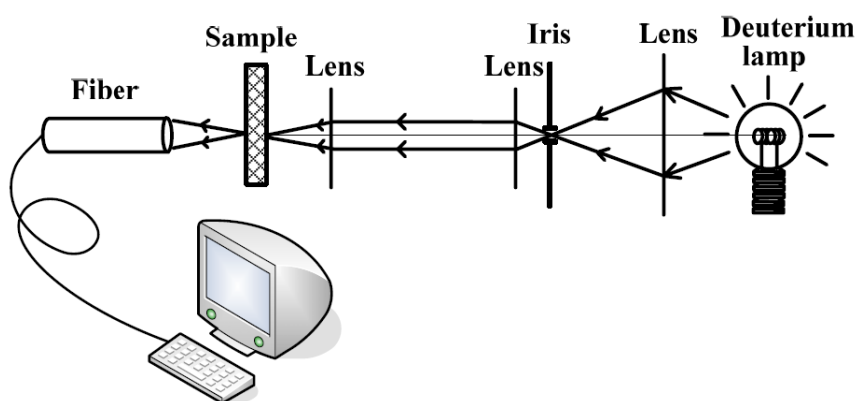


Fig. 3-5 Optical absorption systems

References

1. L. M. Yang, Z. Z. Ye, Y. J. Zeng, W. Z. Xu, L. P. Zhu and B. H. Zhao, *Solid State Commun.* **138**, 577 (2006).
2. S. T. Tan, X. W. Sun, X. H. Zhang, B. J. Chen, S. J. Chua, A. Yong, Z. L. Dong and X. Hu, *J. Crystal Growth* **290**, 518 (2006).
3. S. Barik, A. K. Srivastava, P. Misra, R. V. Nandedkar and L. M. Kukreja, *Solid State Commun.* **127**, 463 (2003).
4. J. G. Lu, Z. Z. Ye, J. Y. Huang, L. P. Zhu, B. H. Zhao, Z. L. Wang, and Sz. Fujita, *Appl. Phys. Lett.* **88**, 063110 (2006).
5. J. G. Lu, Z. Z. Ye, Y. Z. Zhang, Q. L. Liang, Sz. Fujita, and Z. L. Wang, *Appl. Phys. Lett.* **89**, 023112 (2006).
6. A. E. Jimenez-Gonzalez, J. A. Soto Urueta, and R. Suarez-Parra, *J. Cryst. Growth* **192**, 430 (1998).
7. D. Bao, H. Gu, and A. Kuang, *Thin Solid Films* **312**, 37 (1998).
8. C. J. Brinker and G. W. Scherer, *“Sol-Gel Science”*, p. 303.
9. E. W. Seelig, B. Tang, A. Yamilov, H. Cao, and R.P.H. Chang, *Mater. Chem Phys.* **80**, 257 (2003).
10. D. Jezequel, J. Guenot, N. Jouini, F. Fievet, *Mater. Sci. Forum* 152–153 (1994) 339.

Chapter 4 Crystal structures and Lattice dynamics in ZnO

quantum dots

Nanocrystals are a topic of tremendous interest in the scientific community, as properties of these systems are expected to differ radically from the bulk. These systems have a significant ratio of surface to bulk so that the surface energy and the confinement effects can significantly alter the stable crystalline structures and electronic bands. Raman spectroscopy is a powerful characterization tool, being convenient, nondestructive, and extremely sensitive to many phenomena, which include crystalline and noncrystalline phases, imperfections, surface effects, and stress. For bulk crystalline systems, the Raman spectra reflect information about the band at the Γ point ($\vec{k} \cong 0$). In contrast, because finite-sized nanocrystalline systems do not have translational symmetry, the Raman signal is not limited to sampling only the $\vec{k} \cong 0$ region of the Brillouin zone. The Raman spectra in finite-size systems are therefore comparatively broadened, asymmetric, and frequency shifted. The obvious differences between Raman spectra of bulk diamond and micro- and nanocrystalline diamonds are the shift and broadening of bands [1, 2]. Similar differences were found in microcrystalline silicon and have been interpreted using a phonon confinement model [3]. The Raman spectra always show a shift of phonon frequencies in ZnO nanostructures

[4–7]. Whether the origin of this shift is due to strain, intrinsic defects or the size of QDs is still the subject of debates. Nevertheless, by examining ZnO nanocrystals with average sizes of 8.5 and 4.0 nm, Rajalakshmi *et al.* [7] explained the shift of phonon frequency as due to optical phonon confinement in ZnO nanostructures, without considering the effects of crystallite size distribution (CSD) on the Raman spectra in ZnO nanostructures. Additionally, Demangeot *et al.* [8] have reported the resonant Raman scattering (RRS) and low-temperature PL from ZnO NPs with different particle sizes which were synthesized by a room-temperature organometallic method. However, the study showed no size effects from the aspect of either carrier or phonon. The origin of weak size dependence of longitudinal optical (LO) phonon frequency was explained by the ligands bonded to the particle surface, and no shift from the low-temperature PL measurement indicated that UV emission was most likely dominated by weakly bound localized defects, which could come from the surface-bound ionized acceptor-exciton complexes, rather than the size-dependent quantum confinement effect. It is therefore important to note that the nanocrystals synthesized by chemical methods indeed occasionally cause the product suffering the active surround, such as ligands, which could intensely transform the intrinsic properties of the core. Accordingly, the demand for surface passivation of the nanoparticles and the QDs is significant from both the

fundamental scientific research and photonic application points of view.

In this chapter, we reveal the morphology, crystal structures, and lattice dynamics in ZnO QDs.

4.1 Morphology and crystal structures

4.1.1 Morphology

Shown in Fig. 4-1(a) is a typical high-resolution transmission electron microscope (HRTEM) image of the ZnO nanoparticles. Nanoparticles aged at 160 °C for 1 h and solution concentration of 0.06M was selected for particle size determination by HRTEM. The particles shape are predominantly spherical, many also exhibit surface facet, as shown in the inset of Figure 4-1(a) where a step of one atomic layer can be seen. The nanoparticles are clearly well separated and essentially have some aggregation. Figure 4-1(b) show the size distribution of particles after aging at 160°C for 1 h (0.06 M), obtained from analysis of more than 35 particles per sample. The average diameter of the number-weighted particles obtained from a colloid aged at 160°C for 1 h (0.06 M) was determined to be 4.36 ± 0.3 nm. Presumably due to the viscosity of DEG, the solvent may have modified the Ostwald ripening kinetics such that the growth rate decreases with the size of the ZnO QDs. This would narrow the size distribution of ZnO

QDs effectively.

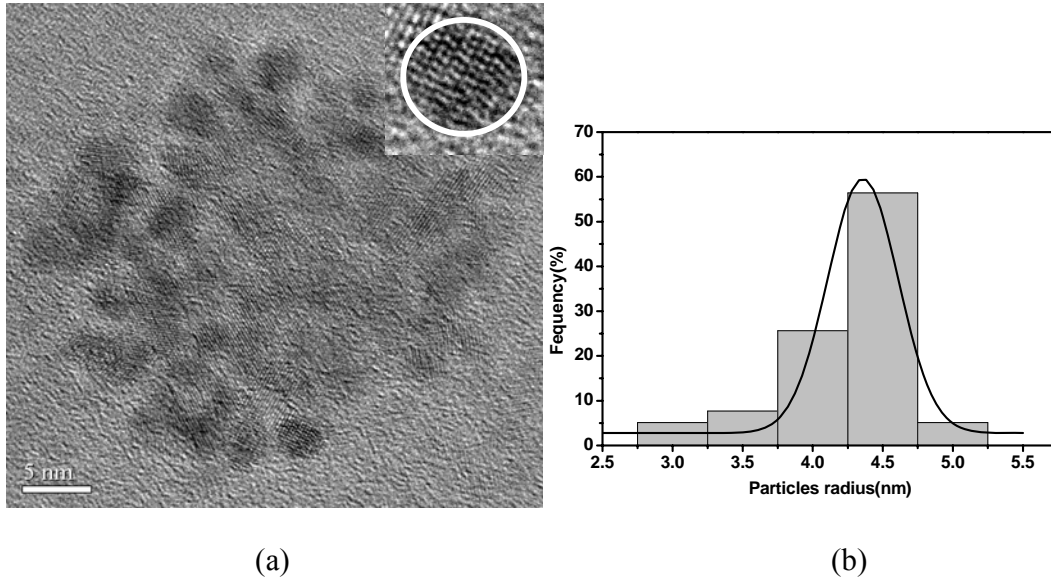


Fig. 4-1 HRTEM image (a) and size distribution (b) of the ZnO QDs fabricated using 0.06M Zn(OAc)₂.

4.1.2 X-ray diffraction measurement

The XRD patterns of the prepared sample (ZnO solution dip on SiO₂ glass) by the sol-gel process are shown in Fig. 4-2. The diffraction lines are the powder X-ray diffraction pattern of the ZnO nanoparticles prepared in a different solution concentration. The diffraction pattern and interplane spacings can be well matched to the standard diffraction pattern of wurtzite ZnO, demonstrating the formation of wurtzite ZnO nanocrystals. All of the samples present similar XRD peaks that can be indexed as the wurtzite ZnO crystal structure with lattice constants $a=3.253\text{\AA}$ and $c=5.219\text{\AA}$, which are consistent with the value in the standard card (JCPDS 36-1451).

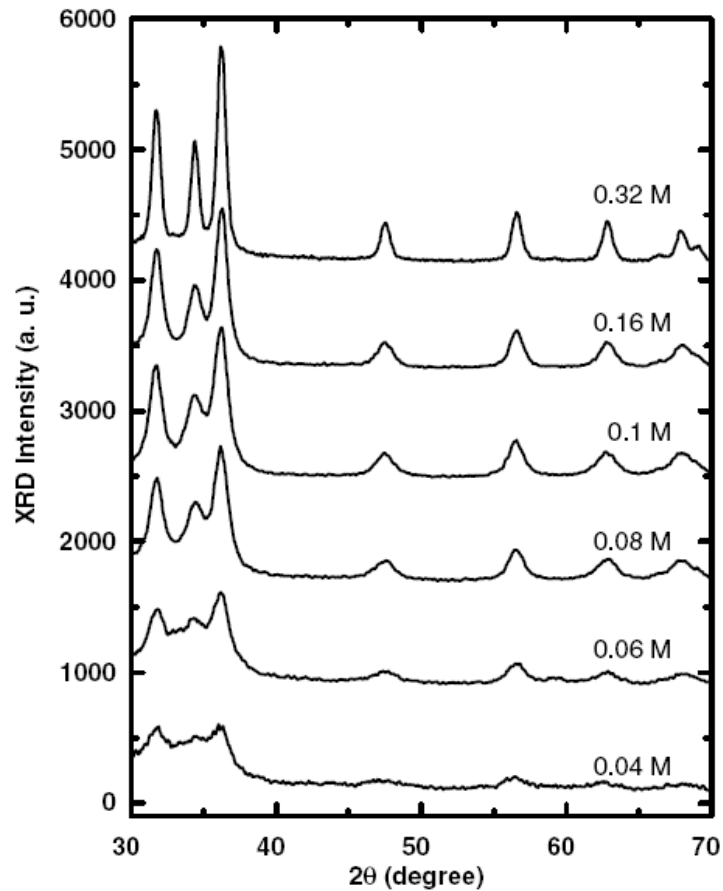


Fig. 4-2 XRD profiles of the ZnO QDs prepared with various concentration of $\text{Zn}(\text{OAc})_2$. The crystalline size can be approximately estimated to be 12, 7.4, 6.5, 5.3, 4.2 and 3.5 nm, respectively (top to bottom), for concentration 0.32, 0.16, 0.1, 0.08, 0.06 and 0.04 M.

No diffraction peaks of other species could be detected that indicates all the precursors have been completely decomposed and no other crystal products were formed. It should be noted here that the full width at half maximum (FWHM) of the diffraction peaks increase with decreasing the concentration of zinc precursor due to the size effect.

The mean diameter of the ZnO nanocrystallites is evaluated from the FWHM of the (110) peak from 3.5nm to 12nm by the Debye-Scherer formula with the range of B from 0.75° to 2.45° , $\theta = 47.56^\circ$ and λ (wavelength of incident X-ray) is 1.5406\AA . The statistical result is consistent with the observation from HRTEM.

4.2 Spatial confinement of optical phonon in ZnO quantum dots

In order to observe the optical phonon confinement effect, the measured micro-Raman spectra with different sizes of ZnO QDs are shown in Fig. 4-3 under a fixed excitation laser power of 3.1 mW.

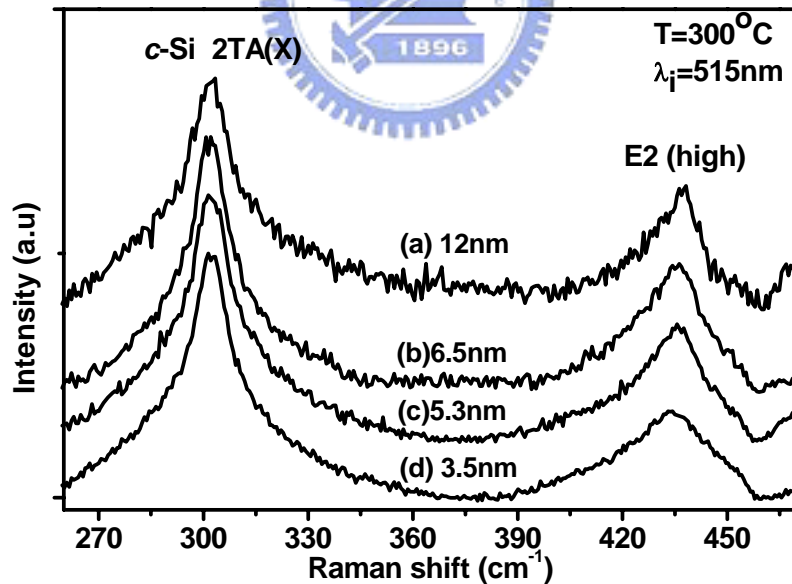


Fig. 4-3 Typical Raman spectra of different sizes of ZnO QDs: (a) 12nm, (b) 6.5nm, (c) 5.3nm, and (d) 3.5nm.

We can see that the Raman peak at 300 cm^{-1} , which comes from the Si substrate [9], stays unshifted in frequency. On the other hand, we found the spectral peak of $E2$ (high) optical phonon around 435 cm^{-1} to shift to the lower frequency as the size of ZnO QDs decreases. Compared with that of the ZnO bulk, a redshift ranging from 0.8 to 4.7 cm^{-1} and an asymmetry (Γ_a/Γ_b) from 1.36 to 1.95 were obtained as the QD size decreases from 12 to 3.5 nm . Note that Γ_a and Γ_b are, respectively, the half widths on the low- and high-energy sides of the $E2$ (high) mode. Such a pronouncing shift, broadening, and the asymmetry of the $E2$ (high) peak could result from three main mechanisms [5]: (1) phonon localization by intrinsic defects, (2) laser heating in nanostructure ensembles, and (3) the spatial confinement within the dot boundaries. The frequency shift of the phonon resulting from defects should not depend upon the size of QDs as also indicated by the small defect PL emission observed in our samples; therefore, we may exclude the defect phonon localization. Additionally, no shift to the $E2$ (high) peak was observed in all ZnO QDs as the laser power has been varied almost an order of magnitude from 1.5 to 12 mW with a fixed laser spot size of about $2\ \mu\text{m}^2$. It is therefore concluded that the Raman shift is mainly due to the spatial confinement of the optical phonon.

The phonon eigenstates are plane waves with infinite correlation lengths in an ideal crystal, therefore, the Raman scattering can only be observed with phonons around the

Brillouin zone center ($q=0$) due to the momentum conservation law. As the crystallite is reduced to nanoscale sizes, the momentum conservation law associated with the Raman scattering can be relaxed and that leads to the spectral shift, broadening, and asymmetry of the Raman modes. The Raman shift and broadening of ZnMnO nanoparticles [10] had been evaluated based on the spatial correlation (SC) model [3]. Because the phonon wave function is partially confined to the volume of the crystallite and if a spherical shape of finite size ZnO QDs is assumed, the first-order Raman spectrum $I(\omega)$ can be described by the following equation [3]:

$$I(\omega) \propto \int_0^1 \frac{4\pi q^2 \exp(-q^2 L^2 / 4) dq}{[\omega - \omega(q)]^2 + (\Gamma / 2)^2} \quad (4-1)$$

where q is expressed in unit of $2\pi/a$, a is the lattice constant, $\omega(q)$ is the phonon dispersion relation, Γ is the linewidth of E_2 (high) phonon of the ZnO bulk, and L is spatial correlation length corresponding to grain size. Furthermore, Islam et al. [11, 12] reported on the influence of crystallite size distribution (CSD) on the shifts in Raman scattering frequencies and line shapes in silicon nanostructures. They modified the Raman intensity expression, $I(\omega)$ of Eq. (4-1), to $I(\omega, L_0, \sigma)$ by using Gaussian CSD of an ensemble of spherical crystallites with mean crystallite size L_0 and standard deviation σ . After integrating the results over the crystallite sizes L under $L_0 > 3\sigma$, the total Raman

intensity expression for the whole ensemble of nanocrystallites becomes

$$I(\omega) \propto \int_0^1 \frac{f(q)q^2 \exp(-q^2 L_0^2 / 4) dq}{[\omega - \omega(q)]^2 + (\Gamma / 2)^2} \quad (4-2)$$

where $f(q) = 1/\sqrt{1+q^2\sigma^2/2}$ is the characteristics of the CSD. The calculated normalization Raman profiles from an ensemble of ZnO QDs having a mean crystallite size $L_0=6.5$ nm with varying σ to illustrate the effect of σ on the Raman line shape are plotted in Fig. 4-4.

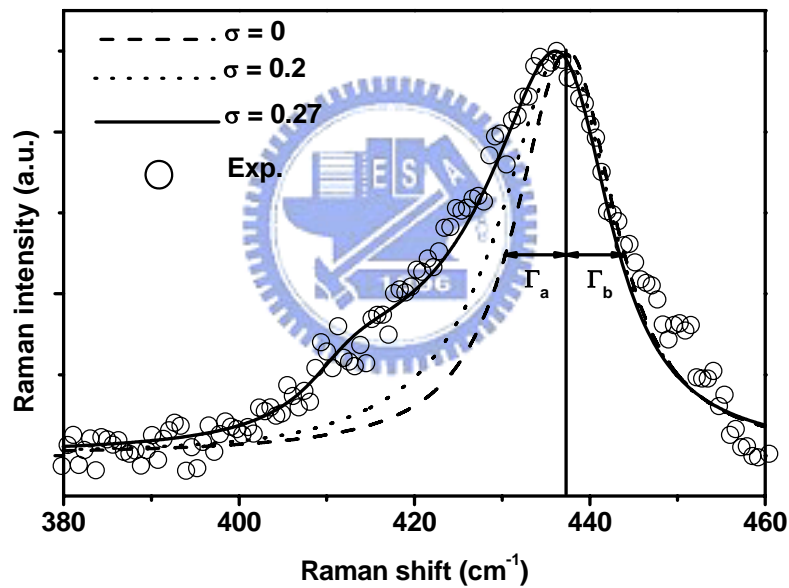


Fig. 4-4 Fitting of the modified spatial correlation model with $\sigma=0$, 0.2 , and 0.27 , respectively to the measured result for average size of 6.5 nm ZnO QDs.

It is clear that a single-crystalline component with $\sigma=0.27$ describes the Raman spectra of 6.5 nm ZnO QDs quite well. Additionally, the CSD of all samples were about 27% , which agrees with the TEM result, e.g., the obtained crystal size $4.3 \text{ nm} \pm 1.1 \text{ nm}$.

The frequency shift $\Delta\omega$ and the asymmetry, Γ_a/Γ_b , of $E2(\text{high})$ mode from the ZnO bulk (439cm^{-1}) as a function of diameter or correlation length with $\sigma = 0.27$ were plotted in Fig. 4-5, in which the solid curves the calculated results of the modified SC model and hollow circles for the experimental. We found the measured frequency shift and asymmetry agrees very well with the calculated ones by the modified SC model and the mean values of crystallite sizes obtained from our fitting are also in good agreement with the XRD results.

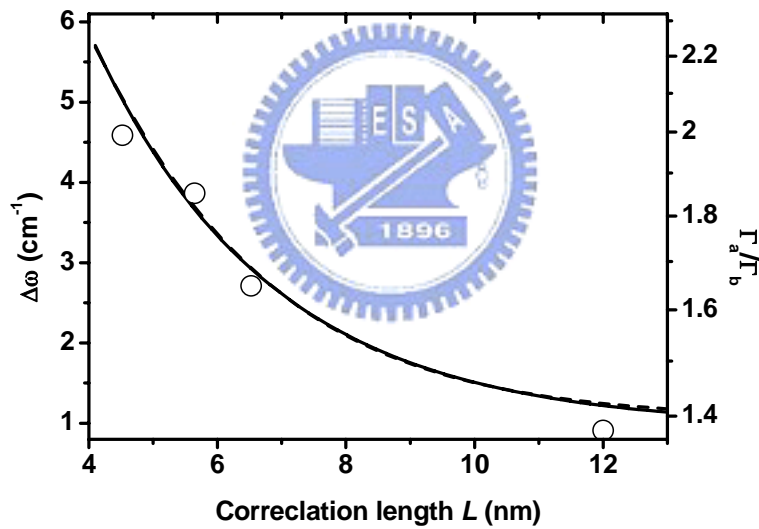


Fig. 4-5 Raman shift $\Delta\omega$ (solid curve) and asymmetric broadening Γ_a/Γ_b (dashed curve) of $E2(\text{high})$ phonon as a function of correlation length L or average size of nanocrystal.

4.3 Electron-phonon coupling in ZnO quantum dots

The electron-phonon interaction could be straightly probed by the RRS when the exciting photon energy is resonant with the electronic interband transition energy of the wurtzite ZnO. The polar symmetry makes the A_1 (LO) and E_1 (LO) modes the dominant ones, while the nonpolar E_2 phonon is not visible. An intense multiphonon scattering of the ZnO QDs with various sizes was observed in the resonant Raman spectra of Fig. 4-6 with background subtracted, where three major bands were observed to result mainly from the polar symmetry modes A_1 (LO) and E_1 (LO) and their overtones.

Multi-phonon scattering processes that have been previously reported for one-dimensional (1D), two-dimensional (2D), and three-dimensional (3D) ZnO systems [13-17], in particular, have been recently reported intensely for zero-dimensional (0D) systems [6, 8].

It is remarkable that the intensities of the first-order Raman modes and their overtones are enhanced while the size of ZnO QDs decreases. The reason can be explained using the total Raman cross section for an n -phonon process as a result of the energy of the incoming or the scattered photon that matches real electronic states in the material to enhance the Raman scattering cross section.

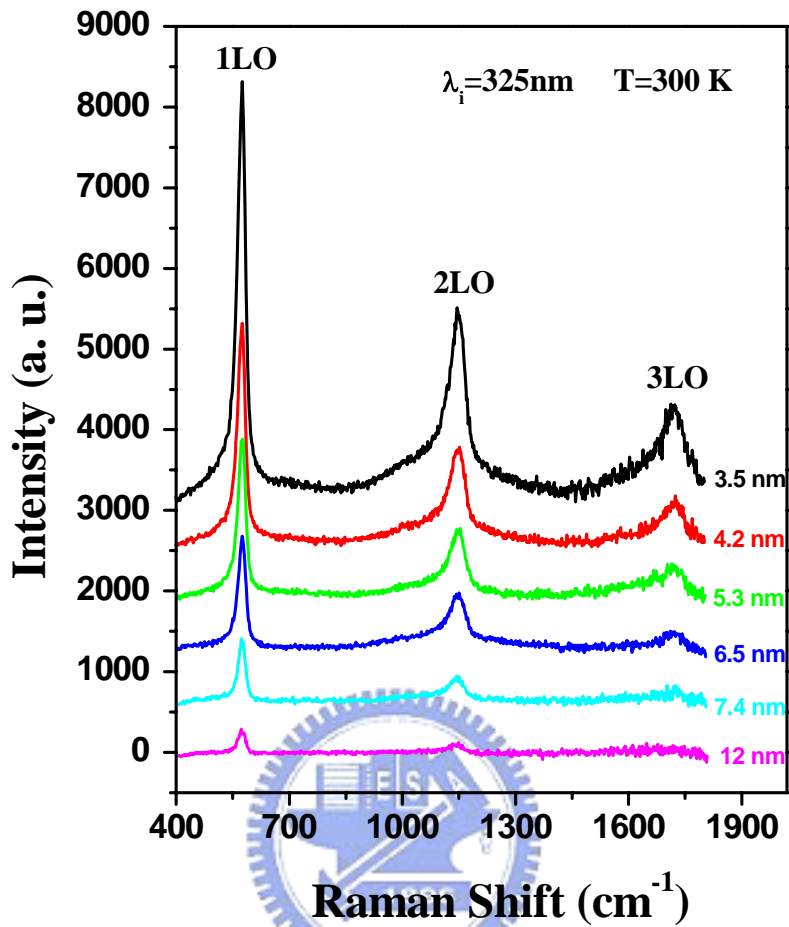


Fig. 4-6 Resonant Raman scatterings of ZnO QDs with various particle sizes measured at room temperature using a He–Cd laser ($\lambda = 325$ nm).

The band gap of the present ZnO QDs certainly tends to approach the excitation laser energy as decreasing its size because of the quantumconfined effect mentioned above. Alim *et al.* [6] have shown that the large redshifts in the RRS spectra from 20 nm ZnO QDs are most likely due to the local heating by UV laser excitation. In the present RRS spectra, the 1LO frequencies were all located at ~ 575 cm^{-1} (within ± 2 cm^{-1}

fluctuation) for the ZnO QDs of different sizes. The heating effect coming from the inspection of micro-Raman seems to be negligible, because we used the laser power of only 0.8 mW at the spot size about $100 \mu\text{m}^2$.

Beyond the phonon frequency shift, by observing the size dependence of intensity ratio between the second- and the first-order LO Raman scatterings, one can evaluate the coupling strength of the electron-phonon interaction. Within the Franck-Condon approximation [18], the electronic oscillation strength distribution over n th phonon mode is defined as $I \sim S^n e^{-S} / n!$, in which S is Huang-Rhys parameter, and also can be used to express the coupling strength of the electron to the LO phonon. The ratio between the second- and the first-order Raman scattering cross sections was found to increase remarkably from 0.4 to 3.1 while an increase of the ZnO crystallite size was from 3.5 to 33 nm, as shown in Fig. 4-7. The electron phonon coupling is generally determined by two mechanisms: the deformation potential and the Fröhlich potential.

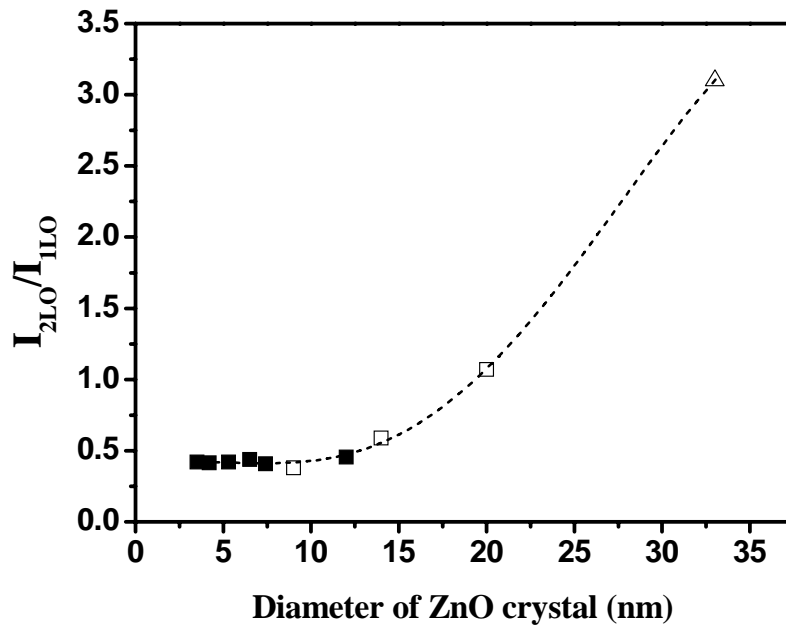


Fig. 4-7 Ratio between the second- and the first-order Raman scattering cross section as a function of ZnO diameter. The experimental values of ZnO QDs in this work (squares) compared with ZnO NPs of Ref. 18 (empty squares) and nanocrystalline ZnO thin films of Ref. 19 (empty triangle). The dashed line joining the data points is just a guide for the eyes.

On the one hand, following Loudon [20] and Kaminow [21], the transverse optical (TO) Raman scattering cross section is determined by the deformation potential that involves the short-range interaction between the lattice displacement and the electrons, and on the other, the LO Raman scattering cross section includes contributions from both the the deformation potential and Fröhlich potential that involves the long-range interaction generated by the macroscopic electric field associated with the LO

phonons. We found that under the resonant conditions the intensity of TO phonon in ZnO QDs is almost insensitive, while that of LO phonon is greatly enhanced. Therefore, we believe that the electron-phonon coupling as decreasing the nanocrystal size is mainly associated with the Fröhlich interaction. Although the complex origin of coupling is not well understood, the result in this study is extremely consistent with reports in other low-dimensional ZnO nano-systems [22, 23].

4.4 Summary

In this work, we have demonstrated successfully the ZnO QDs synthesized by a simple sol-gel method and the average size of ZnO QDs can be tailored under well-controlled concentration of zinc precursor. We have observed the spectral shift, broadening, and asymmetry of the optical phonons for different sizes of ZnO QDs and clarified the origin of these effects is spatial confinement of phonon in ZnO QDs. Using the modified spatial correlation model to analyze the broadening and asymmetry of the first-order E_2 (high) phonon mode, we further confirmed the phonon confinement based on the finite correlation length of a propagating phonon. Additionally, from the resonant Raman scattering (RRS), the coupling strength between electron and longitudinal optical phonon, deduced from the ratio of the second- to the first-order Raman scattering

intensity, diminishes with reducing the ZnO QD diameter. The size dependence of electron-phonon coupling is principally a result of the Fröhlich interaction.

We have investigated the influence of finite size on the lattice dynamics of ZnO and found that the spatial phonon confinement and electron-phonon coupling played the critical part in ZnO QDs. Nevertheless, we have not revealed the effect of finite size on the electronic and optical properties in ZnO QDs. The prospects of emergence of novel physical phenomena and their potential use in designing new and more efficient microelectronic devices constitute the most important motivations of the strong ongoing interest in these low-dimensional systems. Particularly, the exciton-optical phonon interaction has a significant effect on their optical properties. For instance, the exciton binding energies and their oscillator strengths are modified considerably by the exciton-optical phonon interaction. This interaction is also expected to play an important role in determining the optical properties of QDs. Since, in the following chapter we will concentrate on these aspects. The detailed information on interactions between excitons-LO phonons will be extracted from the relevant optical spectra under various temperature.

References

1. M. Yoshikawa, Y. Mori, M. Maegawa, G. Katagiri, H. Ishida, and A. Ishitani, Appl. Phys. Lett. **62**, 3114 (1993).
2. P. K. Bachmann, H. D. Bausen, H. Lade, D. Leers, D. U. Wiechert, N. Herres, R. Kohl, and P. Koidl, Diam. Relat. Mater. **3**, 1308 (1994).
3. H. Richter, Z. P. Wang, and L. Ley, Solid State Commun. **39**, 625 (1981).
4. L. Bergman, X. B. Chen, J. L. Morrison, and J. Huso, J. Appl. Phys. **96**, 675 (2004).
5. K. A. Alim, V. A. Fonoberov, and A. A. Balandin, Appl. Phys. Lett. **86**, 053013 (2005).
6. K. A. Alim, V. A. Fonoberov, M. Shamsa, and A. A. Balandin, J. Appl. Phys. **97**, 124313 (2005).
7. M. Rajalakshmi, A. K. Arora, B. S. Bendre, and S. Mahamuni, J. Appl. Phys. **87**, 2445 (2000).
8. F. Demangeot, V. Paillard, P. M. Chassaing, C. Pagès, M. L. Kahn, A. Maisonnat, and B. Chaudret, Appl. Phys. Lett. **88**, 071921 (2006).
9. R. P. Wang, G. W. Zhou, Y. L. Liu, S. H. Pan, H. Z. Zhang, and D. P. Yu, Phys. Rev. B **61**, 16 827 (2000).
10. J. B. Wang, H. M. Zhong, Z. F. Li, and Wei Lu, J. Appl. Phys. **97**, 086105 (2005).

11. Md. N. Islam and S. Kumar, *Appl. Phys. Lett.* **78**, 715 (2001).
12. Md. N. Islam, A. Pradhan, and S. Kumar, *J. Appl. Phys.* **98**, 024309 (2005).
13. J. F. Scott, *Phys. Rev. B* **2**, 1209 (1970).
14. X. T. Zhang, Y. C. Liu, Z. Z. Zhi, J. Y. Zhang, Y. M. Lu, D. Z. Shen, W. Xu, G. Z. Zhong, X. W. Fan, and X. G. Kong, *J. Phys. D* **34**, 3430 (2001).
15. V. V. Ursaki, I. M. Tiginyanu, V. V. Zalamai, V. M. Masalov, E. N. Samarov, G. A. Emelchenko, and F. J. Briones, *J. Appl. Phys.* **96**, 1001 (2004).
16. H. T. Ng, B. Chen, J. Li, J. Han, M. Meyyappan, J. Wu, S. X. Li, and E. E. Haller, *Appl. Phys. Lett.* **82**, 2023 (2003).
17. H. M. Cheng, H. C. Hsu, Y. K. Tseng, L. J. Lin, and W. F. Hsieh, *J. Phys. Chem. B* **109**, 8749 (2005).
18. K. Huang and A. Rhys, *Proc. R. Soc. London, Ser. A* **204**, 406 (1950).
19. V. V. Ursaki, I. M. Tiginyanu, V. V. Zalamai, V. M. Masalov, E. N. Samarov, G. A. Emelchenko, and F. J. Briones, *J. Appl. Phys.* **96**, 1001 (2004).
20. R. Loudon, *Adv. Phys.* **13**, 23 (1964).
21. I. P. Kaminow and W. D. Johnston, *Phys. Rev.* **160**, 19 (1967).
22. T. Makino, K. Tamura, C. H. Chia, Y. Segawa, M. Kawasaki, A. Ohtomo, and H. Koinuma, *Phys. Rev. B* **66**, 233305 (2002).

23. R. P. Wang, G. Xu, and P. Jin, Phys. Rev. B **69**, 113303 (2004).



Chapter 5 Reducing exciton-longitudinal-optical phonon interaction with shrinking ZnO quantum dots

Optical and physical properties of semiconductor QDs have also devoted considerable efforts to study due to their potential applications to light-emitting diodes [1], optically pumped lasers [2] and other electronic devices [3]. Although large numbers of researches on II-VI QDs and III-V QDs have been published [4, 5], the properties of ZnO QDs have not been studied as completely as other materials.

The interaction between exciton and longitudinal-optical (LO) phonon has a great influence on the optical properties of polar semiconductors. Ramvall, *et al.* [6] reported a diminishing temperature-dependent shift of the PL energy with decreasing GaN QD size caused by a reduction of the LO-phonon coupling. Chang, *et al.* [7] theoretically reported that the exciton LO-phonon interaction energy $|E_{\text{ex-ph}}|$ evaluated as functions of electric field strength and the size of the QDs. The field enhanced by reducing the separation between electron and hole would increase $|E_{\text{ex-ph}}|$; whereas, the decrease of dot size leads to delocalize the wave functions of both electron and hole in turn decreases $|E_{\text{ex-ph}}|$. However, the size dependence of exciton-LO-phonon coupling is a complicated problem to be investigated.

5.1 Band gap variation of size-controlled ZnO quantum dots

Figure 5-1 shows typical PL and absorption spectra of the samples with different average QD sizes at room temperature. The UV emission represents a relaxed state of exciton near the band edge in the ZnO QDs. The nature of the UV-PL from ZnO QDs itself is still a matter of controversy.

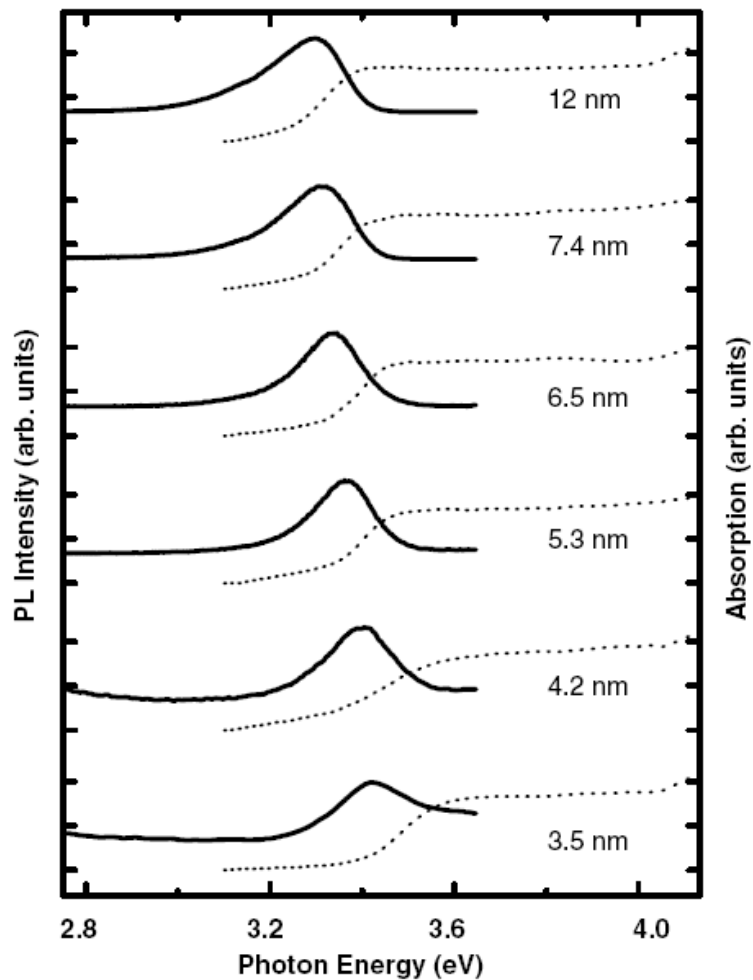


Fig. 5-1 PL (solid line) and absorption (dashed line) spectra near the band edge of various ZnO QD size.

Some authors attributed the UV-PL to the recombination of confined excitons [8], while others argued that the emission comes from surface impurities or defects [9]. Aforementioned Demangeot *et al.* [10] have reported that ligands coordinated at the surface of the nanoparticles may induce some changes in ZnO bonds, leading to some modifications of either their mechanical or dielectric properties. The UV-PL came from surface-bound ionized acceptor-exciton complexes revealed no significant energy shift with varying size of ZnO NPs; furthermore, the weak bound emission vanished at the measured temperature higher than 15K. In our case, high efficient UV emission near band edge is attributed to confined exciton emission, with high density of states which shifts to the higher energies from 3.30 to 3.43 eV as the size of QDs decreases from 12 to 3.5 nm which are comparable or smaller than the diameter 4.68 nm of exciton (Bohr radius of bulk ZnO is 2.34 nm [11]), the Coulomb interaction should be relatively small as compared to the kinetic energy resulting from confinement in our samples and the ZnO QDs are in the moderate to strong confinement regime. In general, quantum confinement shifts the energy levels of the conduction and valence bands apart, giving rise to a blue shift in the transition energy as the particle size decreases. Such phenomenon is also revealed in the absorption spectra, although the faint excitonic absorption peaks due to the moderate size distribution of ZnO QDs. However, from this

figure, it can clearly be seen that the absorption onset exhibits a progressive blue shift from 3.43 to 3.65 eV as the size of ZnO QD decreases. Similar observations of such size dependence upon optical properties have been made previously for other semiconductor QDs [12-14]. Moreover, the discernible broad green band (2.1-2.8 eV) was observed only when the size of ZnO QDs is smaller than 4.2 nm as shown in Fig. 5-2, the surface-located complex emission reasonably be enhanced while the surface volume of QDs were increased as decreasing the particle size. The relatively weak visible emission indicated that the ZnO QDs contain less intrinsic defects at the surface.

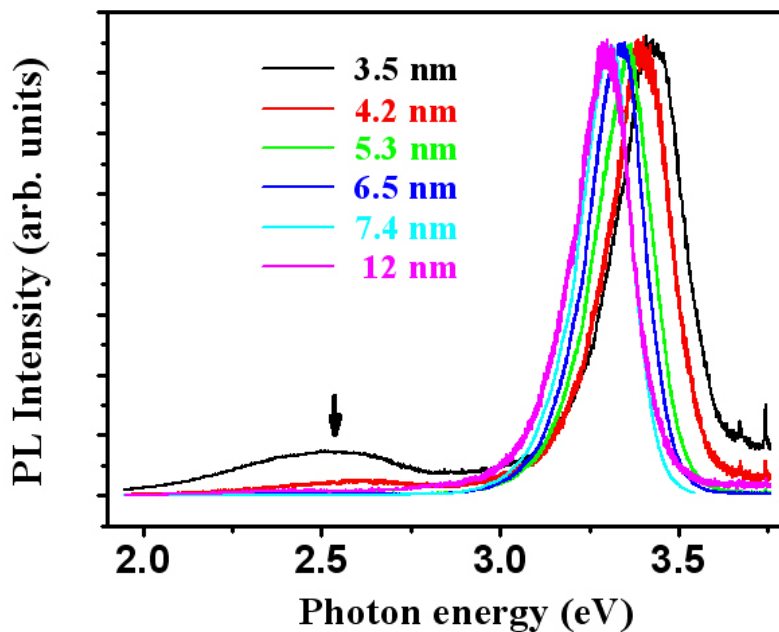


Fig. 5-2 Room temperature PL spectra of ZnO QDs with various sizes

To circumvent other probabilities, we operated the PL measurements at different

power. The unchanged energies of the UV emission peaks, as shown in Fig. 5-3, exhibit no considerable local heating effect in ZnO QDs, and the obtained exponent value about 1.3 of power law confirmed our assignment that the observed UV emission bands are due to excitonic transition. In addition, the XRD peaks reveal no significant shift, confirming that the ZnO QDs completely are strain-free.

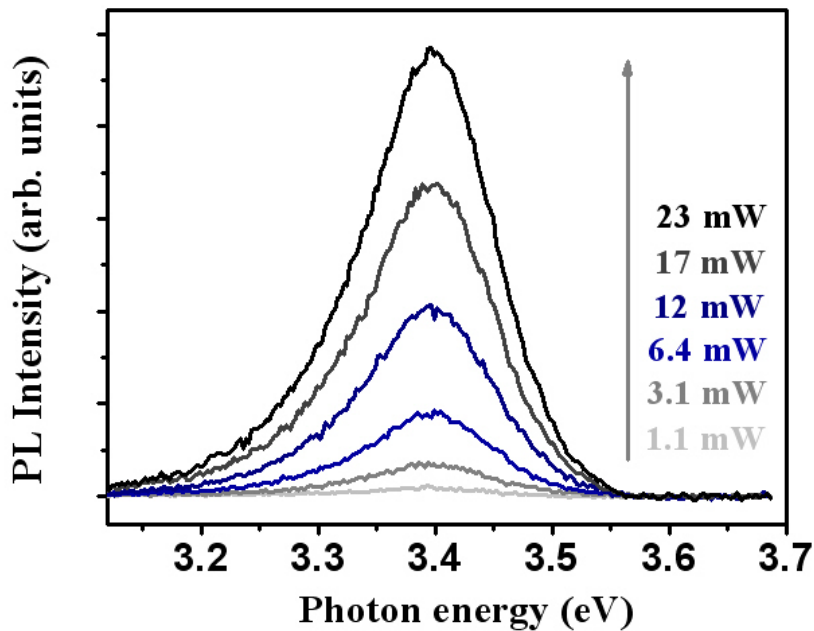


Fig. 5-3 PL spectra of ZnO QDs (4.2 nm in diameter) as a function of excitation laser intensity (from 1.1mW to 23mW), the exponent γ of power law $I \sim L^\gamma$ lies about 1.3.

The relationship between band gap and size of QD can be obtained using a number of models [15-18]. Using the effective mass model for spherical particles with a Coulomb interaction term [15], the band gap E_g^* [eV] can be approximately written as:

$$E_g^*(r) \cong E_g^{bulk} + \frac{\hbar^2 \pi^2}{2er^2} \left(\frac{1}{m_e} + \frac{1}{m_h} \right) - \frac{1.8e^2}{4\pi\epsilon\epsilon_0 r} \quad (5-1)$$

where E_g^{bulk} is the bulk energy gap, r is the particle radius, m_e is the effective mass of the electrons, m_h is the effective mass of the holes, ϵ is the relative permittivity, ϵ_0 is the permittivity of free space, \hbar is Planck's constant divided by 2π , and e is the charge of the electron. The polarization term included in this model is usually negligible.

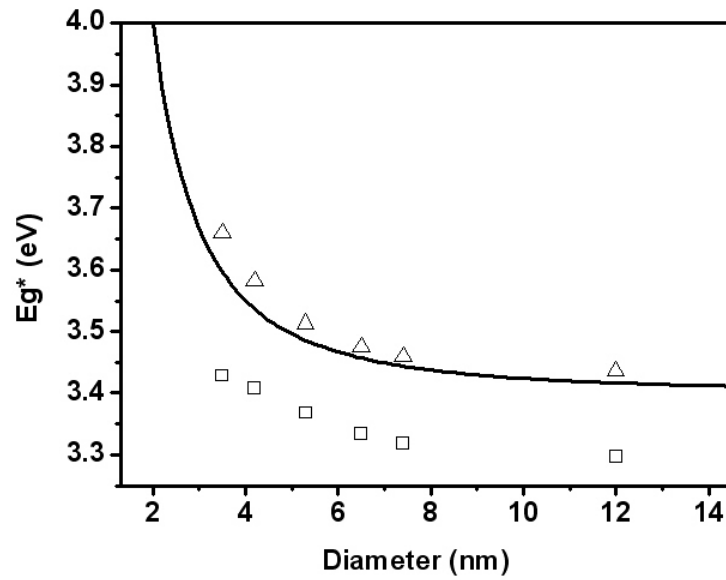


Fig. 5-4 The dependence of the band gap enlargement versus the ZnO QDs diameter as calculated from the effective mass model and the corresponding experimental data of PL peak maximum (□) and the absorption onset (Δ).

Figure 5-4 shows both the UV emission peaks, absorption onsets and the dependence of the band gap enlargement on the ZnO QD diameter as calculated from the

effective mass model (Eq. 2) with $E_g^{bulk}=3.35$ eV, $m_e=0.24 m_0$, $m_h=0.45 m_0$, and $\varepsilon = 3.7$, where m_0 is the free electron mass [19]. Enlargement effects are expected to be predominant when the QD size is less than 6 nm, meanwhile PL data and absorption data of the same tendency indicates effective mass theories accurately, which predict the size dependent energy gap. We note here that the absorption data closely coincides with the curve calculated from the effective mass model. However, the PL data is not fixed since it represents the emission from a relaxed state and the exciton binding energy should be considered.



5.2 Influence of exciton-longitudinal phonon interaction with shrinking ZnO quantum dots

Figure 5-5 shows the PL spectrum of different ZnO sizes at 13 K. The spectrum of ZnO powders consists of the free exciton (FX) and the donor-bound exciton (D^0X) emission peaks along with three obvious LO-phonon replicas. The FX emission of ZnO powders is 3.377eV which behaves as ZnO bulk. The energy shift (dash line) from 3.377 eV to 3.475 eV due to quantum confinement effect (QCE) can be observed. The full width at half maximum (FWHM) which increases as the dot size decreases may be caused by the contribution of surface-optical phonon [20], surface-bound acceptor

exciton complexes [21], and size distribution. Accordingly, we observed that LO-phonon replicas are obvious in ZnO powders but are unapparent in other QD-samples.

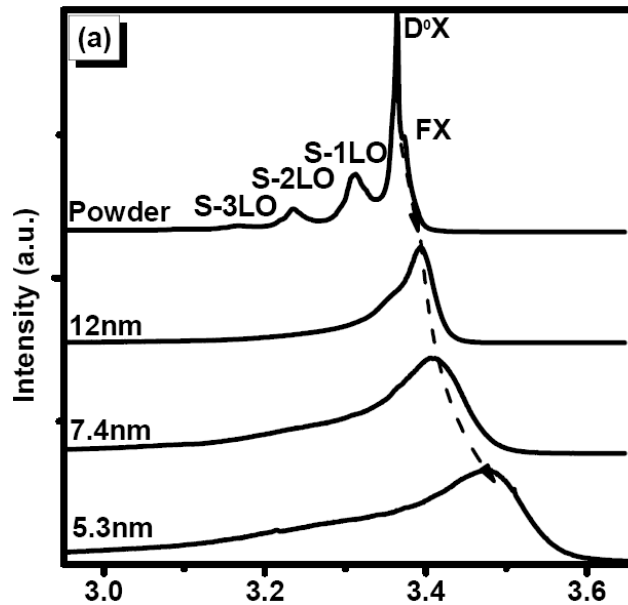


Fig. 5-5 PL spectra of different ZnO particle sizes at 13K. The dashed line indicates the free exciton peak energy shift.

Duke *et al.* [22] interpreted the intensities of LO-phonon replicas depend strongly on their exciton-phonon coupling strengths.

Figure 5-6 displays the temperature-dependent PL of 7.4-nm QDs, it reveals only single one band for $T = 300$ K. Due to small binding energy of D^0X , it will be ionized as $T > 100$ K, so we can easily attribute the single band to the FX emission. We also

find that the peak energy difference of FX between 13 K and 300 K is ~ 25 meV that is smaller than 65 meV of the ZnO powders. It is known that the main contribution to the energy shift is the Fröhlich interaction [23], a result of Coulomb interaction.

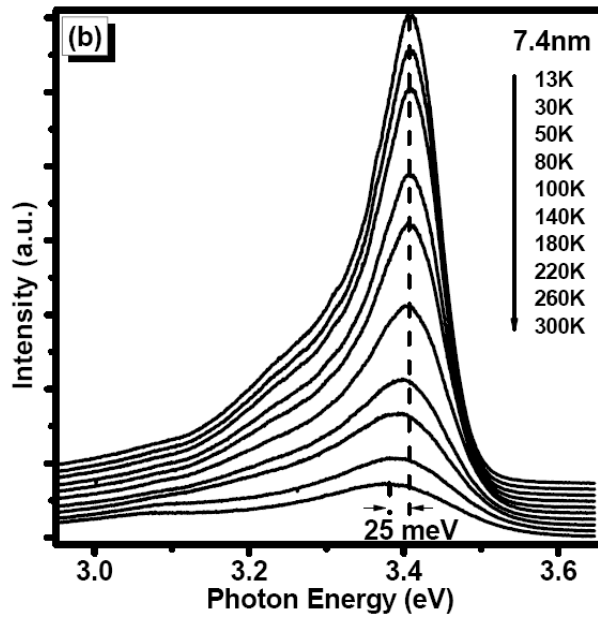


Fig. 5-6 Temperature-dependence PL spectra of 7.4 nm of ZnO QDs in the range 13-300K. The dashed lines marked the peak energies of 13 and 300K. Their energy difference is 25 meV.

From the temperature-dependence PL, we can obtain the exciton binding energy (E_b),

from the following relation [24]:

$$I(T) = \frac{I(0)}{1 + A \exp(-E_b / k_B T)} \quad (5-2)$$

where $I(T)$ is the integrated intensity of the peak at specific temperature, $I(0)$ is the

integrated intensity at absolute zero, A is a constant, and k_B is Boltzmann constant. The fitting results are shown in Fig. 5-7, E_b of the ZnO powder is 60 meV, which is close to that of ZnO Bulk. We obtained $E_b = 67, 87$ and 132 meV, respectively, for 12, 7.4, and 5.3 nm QDs. The decreasing particle size would raise the electron-hole interaction as a result of the compressing boundary to cause increasing Coulomb energy. Therefore, the binding energy increases as the particle size decreases.

In order to quantitatively investigate the relation between the quantum confinement size and the exciton-LO phonon interaction, we introduced the temperature-dependent exciton energy [25]:

$$E_{ex}(T) = E_{ex}(0) - \sum_i \frac{\alpha_{0i}}{\exp(\hbar\omega_i/k_B T) - 1} \quad (5-3)$$

where $E_{ex}(T)$ is the exciton energy at a specific temperature T, $E_{ex}(0)$ is the exciton energy at 0 K, and α_{0i} represents the coupling strength with the optical phonon with energy $\hbar\omega_i$.

Our previous RRS and PL results indicate the most promising LO-phonon involved in RRS and PL is the one having energy of 72 meV, we therefore take only a single one of the summation terms with $\hbar\omega = 72$ meV into account to discuss exciton-LO phonon coupling. Then the α_0 represents the weighting of exciton-LO-phonon coupling. The fitting results are shown in Fig. 5-7 and $\alpha_0 = 0.59, 0.40, 0.21,$ and 0.19 for powders, 12 nm, 7.4 nm, and 5.3 nm QDs, respectively. These results are in consistent with the

observations of PL spectra, weakening coupling strength of exciton-LO phonon as decreasing the particle sizes.

The increasing E_b gives an indication for reduction of exciton-LO phonon interaction. The enhancement of E_b or Coulomb potential indicates a reduction of a_B . It makes the exciton less polar capable for efficiently interacting with LO-phonon through the Fröhlich interaction [26].

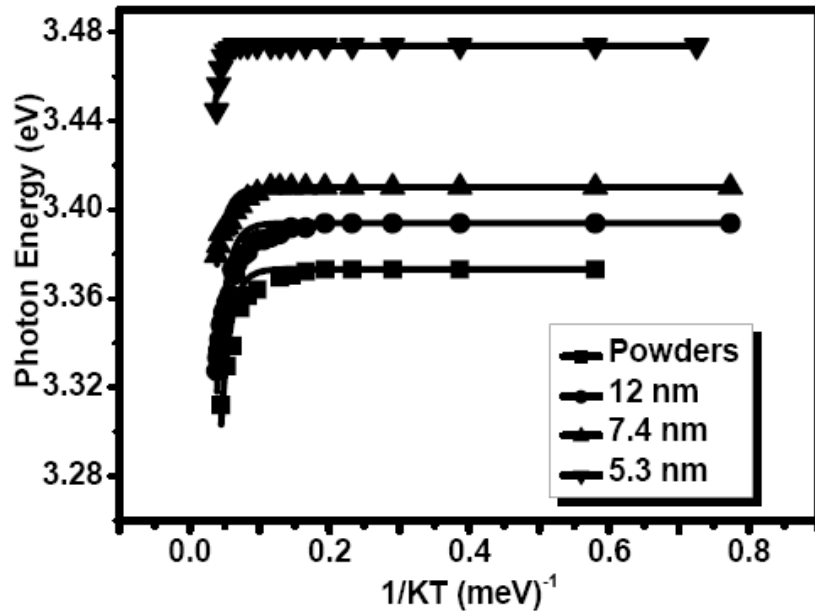


Fig. 5-7 Experimental and calculated (solid line) exciton energies plotted against inverse temperature for different ZnO particle sizes.

To find out the relation between a_B and α_0 , we calculated a_B from our PL spectra including the FX emission energy and E_b for different dot sizes based on the weak

confinement model [15] as Eq.(5-1), and $a_B^2 = \hbar^2/(2\mu^*E_b)$ [27]. The calculated exciton Bohr radii a_B -QD for 5.3 nm, 7.4 nm and 12 nm QDs are 0.977 nm, 1.038 nm and 1.328 nm. The ratios of a_B QD to the exciton Bohr radius for bulk ZnO of a_B bulk = 2.34 nm are 0.42, 0.46 and 0.57, respectively, which agree well with 0.42, 0.49 and 0.59 obtained by Senger, *et al* [11].

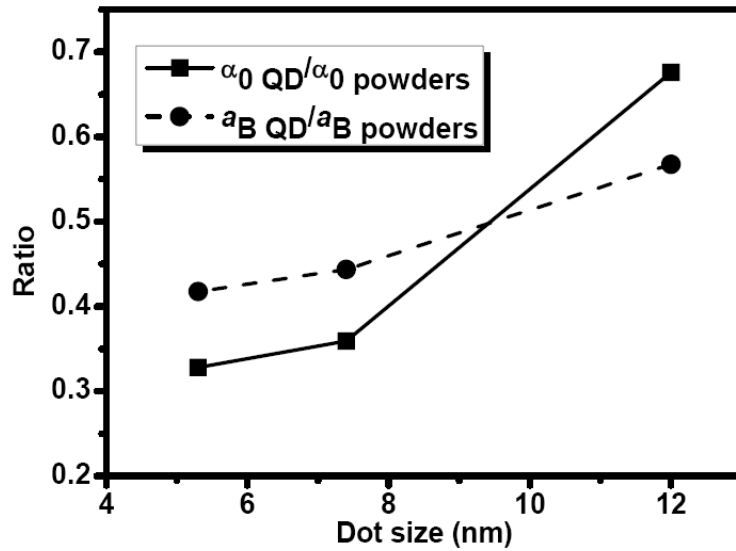


Fig. 5-8 The relation of $\alpha_0 \text{ QD} / \alpha_0 \text{ Powders}$ and $a_B \text{ QD} / a_B \text{ Powders}$ with different dot sizes.

Figure 5-8 shows similar trends of $\alpha_0 \text{ QD} / \alpha_0 \text{ Powders}$ and $a_B \text{ QD} / a_B \text{ bulk}$ against the dot size. It represents that the exciton formation is attained by Coulomb interaction, as the particle sizes decrease, the quantum confinement effect causes increase of E_b and decrease of a_B . The electric dipole, which is proportional to the distance of electron-hole pair, is then reduced. The exciton formation thus becomes less polar so that reducing the coupling strength with the polar lattice via the Fröhlich interaction. Consequently,

we demonstrated the reduction of exciton-LO phonon interaction occurs in ZnO-QD system.

5.3 Summary

In this chapter, size-dependence of efficient UV PL and absorption spectra of various QD sizes give evidence for the quantum confinement effect. We exhibit no considerable local heating effect in ZnO QDs, and the obtained exponent value about 1.3 of power law confirmed our assignment that the observed UV emission bands are due to excitonic transition. Band gap enlargement is also in agreement with the theoretical calculation based on the effective mass model. Furthermore, we presented temperature-dependent PL of different sizes of ZnO particles. The unobvious LO-phonon replicas of FX were observed when the ZnO particle sizes were under 12 nm in diameter. The FX emission energy difference of 13-300 K decreases as the particle size decreases. The increasing exciton E_b with the decreasing quantum dot size can be obtained from temperature-dependent PL. From the temperature-dependent change of FX emission energy, the exciton-LO phonon coupling strength reduces as the particle size decreases. The reduced a_B with particle size obtained from E_b and PL spectrum confirms that the exciton becomes less polar in turn reducing the Fröhlich interaction and the exciton-LO

phonon interaction is reduced with decreasing ZnO QDs.

Although we have studied the physical properties and optical properties of ZnO finite crystallites, we have not investigated the influence of finite size on the electronic behavior of ZnO. Particularly, the effective-mass approximation apparently gives a good understanding of the blue shift of the optical absorption threshold. However, this approach fails for the smallest crystallite sizes because of the oversimplified description of the crystal potential as a spherical well of infinite depth. This can be understood from the band structure scheme. In the effective-mass approximation the highest valence band and the lowest conduction band are assimilated closer to their extrema (at $k = 0$) to parabolic curves of the form $\hbar^2 k^2 / 2m^*$, where k is the amplitude of the wave vector. As k increases, this expression varies more steeply than the true dispersion relation. The ground state of the spherical well is given by this dispersion relation with $|k| = 2\pi/d$ (quantum size effect). Thus, the first term in effective-mass approximation is the difference between the gap of small crystallites and that of infinite semiconductors. Its value and consequently the exciton peak position will be overestimated in comparison with the true value for the small diameters. A better description of the band structure can be obtained from a tight-binding framework. Since the atomic structure is implicitly considered, this method is more adequate for small crystallites. Since, in the following

chapter we will concentrate on electronic structure and optical properties in ZnO from bulk to finite crystallites using tight-binding framework.



References

1. C. Y. Lee, Y. T. Huang, W. F. Su, and C. F. Lin, *Appl. Phys. Lett.* **89**, 231116 (2006).
2. K. Tachibana, T. Someya, Y. Arakawa, R. Werner, A. Forchel, *Appl. Phys. Lett.* **75**, 2605 (2005).
3. G. Yusa, H. Sakaki, *Superlattices and Microstructures* **25**, 247 (1999).
4. A. Murayama, T. Furuta, K. Hyomi, I. Souma, Y. Oka, D. Dagnelund, I. A. Buyanova, and W. M. Chen, *Phys. Rev. B* **75**, 195308 (2007).
5. Y. H. Cho, H. S. Kwack, B. J. Kwon, J. Barjon, J. Brault, B. Daudin, and L. S. Dang, *Appl. Phys. Lett.* **89**, 251914 (2006).
6. P. Ramvall, P. Riblet, S. Nomura, and Y. Aoyagi, *J. Appl. Phys.* **87**, 3883 (2000).
7. R. Chang, and S. H. Lin, *Phys. Rev. B* **68**, 045326 (2003).
8. D. W. Bahnemann, C. Kormann, and M. R. Hoffmann, *J. Phys. Chem.* **91**, 3789 (1987).
9. L. Guo, S. Yang, C. Yang, P. Yu, J. Wang, W. Ge, G. K. L. Wong, *Appl. Phys. Lett.* **76**, 2901 (2000).
10. F. Demangeot, V. Paillard, P. M. Chassaing, C. Pagès, M. L. Kahn, A. Maisonnat, and B. Chaudret, *Appl. Phys. Lett.* **88**, 071921 (2006).
11. R. T. Senger and K. K. Bajaj, *Phys. Rev. B* **68**, 045313 (2003).

12. D. J. Norris, Al. L. Efros, M. Rosen, and M. G. Bawendi, Phys. Rev. B **53**, 16338 (1996).
13. C. A. Smith, H. W. H. Lee, V. J. Leppert, S. H. Risbud, Appl. Phys. Lett., **75**, 1688 (1999).
14. H. Zhang, L. P. Wang, H. M. Xiong, L. H. Hu, B. Yang , W. Li, Adv. Mater. **15**, 1712 (2003).
15. L. E. Brus, J. Chem. Phys. **80**, 4403 (1984).
16. M. S. Hyberstsen, Phys. Rev. Lett. **72**, 1514 (1994).
17. A. L. Efros, M. Rosen, Annu. Rev. Mater. Res. **30**, 475 (2000).
18. K. E. Andersen, C. Y. Fong, W. E. Pickett, J. Non. Cryst. Solids **299**, 1105 (2002).
19. S. A. Studenikin, N. Golego, M. Cocivera, J. Appl. Phys. **84**, 2287 (1998).
20. Z. D. Fu, Y. S. Cui, S. Y. Zhang, J. Chen, D. P. Yu, S. L. Zhang, L. Niu and J. Z. Jiang, Appl. Phys. Lett. **90**, 263113 (2007).
21. V. A. Fonoberov and A. A. Balandin, Appl. Phys. Lett. **85**, 5971 (2004).
22. C. B. Duke and G. D. Mahan, Phys. Rev. **139**, 1965 (1965).
23. S. J. Sheih, K. T. Tsen, D. K. Ferry, A. Botchkarev, B. Sverdlov, A. Salvador, and H. Morkoc, Appl. Phys. Lett. **67**, 1757 (1995).
24. D. S. Jiang, H. Jung, and K. Ploog, J. Appl. Phys. **64**, 1371 (1988).

25. L. Vinã, S. Logothetidis, and M. Cardona, Phys. Rev. B **30**, 1979 (1984).
26. J. J. Shiang, S. H. Risbud, and A. P. Alivisatos, J. Chem. Phys. **98**, 8432 (1993).
27. N. Zettili, Quantum Mechanics, Concepts and Applications (2004).



Chapter 6 Calculation of electronic structure and density of states in the wurtzite structure of $Zn_{1-x}Mg_xO$ alloys using sp^3 semi-empirical tight-binding model

In the past decade, the advantageous technologies of light-emitting diodes (LED) and semiconductor lasers realize full-color display systems which have prompted the research for devices operating in the blue-ultraviolet (UV) [1-3]. Zinc-oxide (ZnO) materials have drawn considerable attention for the application in UV optoelectronics because of their excitonic transition energy (~ 3.37 eV) and large exciton binding energy (~ 60 meV). The band gap becomes even larger if Zn atoms are substituted by magnesium (Mg) atoms, which have a similar ionic radius, allowing for quantum-well structures and superlattices [4-6]. The change of band gap of the $Zn_{1-x}Mg_xO$ (ZMO) layers grown on sapphire [21] with $0.1 < x < 0.3$ and powders [20] with $0 < x < 0.05$ have been reported; and in the Al doped ZMO alloys with a preferential c-axis orientation, Lu et al. [23] experimentally showed that the electron effective masses increase with increasing Mg concentration. However, it is still lack of theoretical confirmation of bandgap and electron effective mass as increasing Mg incorporation.

In the wurtzite $Zn_{1-x}Mg_xO$ (ZMO) alloys, Malashevich [28] et al. investigated the polarization-related properties based on density-functional-theory calculation under the

local-density approximation and the Berry-phase approach to calculate electric polarization. Li and Wei [25] used the first-principle band-structure method to show that if Mg atoms substitute Zn atoms to reduce the anion and cation kinetic p-d repulsion, the acceptor transition energy of $N_{O-nZn_{Zn}}$ can be reduced. Whereas, the application of the first-principles calculation to study electronic band structure of disordered alloys and solid solutions generally requires using very large supercell in order to mimic the distribution of local chemical environments. It is very computationally demanded. On the other hand, the tight-binding (TB) theory is a versatile and simple method to calculate the electronic properties of solids. Additionally, due to the transferability of the TB parameters, the method has been readily applied to systems with broken translational invariance such as low-dimensional structures, clusters and alloys. Using the TB approach, among the quantities that are successfully calculated are elastic constants [7], phonon spectra [8], vacancy-formation energies, and surface energies [9, 10], as well as cluster-formation [11] energies and magnetic moments. Particularly, the electronic structure of semiconductor compounds is well calculated in the complete Brillouin zone [12, 13]. Nevertheless, there were few theoretical calculations of the electronic structure in the $Zn_{1-x}Mg_xO$ alloy system. Particularly, for electronic devices, knowledge of the effective masses is especially important for analyzing the device properties,

especially the current transport characteristics.

In this chapter, we present the electronic band structure and total density of states (DOS) of ZnO and ZMO alloy crystallization using the nearest- and the next-nearest-neighbor SETB approach sp^3 model [14].

6.1 Theoretical details

We present the electronic band structure and total DOS of ZnO and ZMO alloy crystallization using the nearest- and the next-nearest-neighbor SETB approach sp^3 model [14]. The virtual-crystal approximation (VCA) [12] was used by taking weighted averages of the diagonal matrix elements for the band structures of the alloys, namely, we write the SETB parameters of the binary compounds,

$$E_b(\text{Zn}_{1-x}\text{Mg}_x\text{O}) = (1-x)E_b^{\text{ZnO}} + xE_b^{\text{MgO}}, \quad b = s, p_x, p_y, p_z, \quad (6-1)$$

where $E_b^{\text{ZnO, MgO}}$ are the binding energies of corresponding orbitals of Zn and Mg bound to O2p and O2s orbitals and x is the incorporation concentration of Mg. The off-diagonal matrix elements, multiplied by the square of the bond length, are also averaged this way (Harrison's rules) [15] with the bond length obtained from Vegard's law [16],

$$d(\text{Zn}_{1-x}\text{Mg}_x\text{O}) = (1-x)d_{\text{ZnO}} + xd_{\text{MgO}} \quad (6-2)$$

Thus, we assume that virtually all of the Zn and Mg atoms occupy cation sites, while

anion sites are overwhelmingly occupied by O. The VCA treats an alloy as a perfectly periodic crystal, assuming its symmetry identical to the symmetry of the constituents; therefore, regarding the question of crystal structure and stability, we considered that the wurtzite ZMO alloy is stable with respect to the corresponding rocksalt alloy for $x < 0.375$ [17, 18].

6.2 Band structures of $\text{Zn}_{1-x}\text{Mg}_x\text{O}$

The resultant band structures for ZnO and $\text{Zn}_{0.7}\text{Mg}_{0.3}\text{O}$ were given in Fig. 6-1. The deepest and lowest valence band of ZnO crystal (Fig. 6-1(a)) near -20 eV corresponds to an atomic-like O2s state, and the upper valence bands are mainly composed of the O2p state and Zn4s and 4p states. The lowest conduction band is contributed by Zn4s state, and the uppermost conduction bands are primarily caused by Zn4p character. The ZMO is direct band gap semiconductor for all stable wurtzite structure and has band gap (at 0K) ranging from 3.429 eV for ZnO to 4.153 eV for $\text{Zn}_{0.7}\text{Mg}_{0.3}\text{O}$. In addition, we also estimate the p doubly degeneracy in valence bands with renormalized atomic spin-orbital (SO) splitting of the anion and cation p states [19]. For ZnO we got 15 meV for SO energy (Δ_0), offering a good agreement with experimental results [20], while the modification of SO energy was not conspicuously observed in $\text{Zn}_{1-x}\text{Mg}_x\text{O}$ alloy.

However, we perceived that the band gap at Γ point increase as Mg concentration increases.

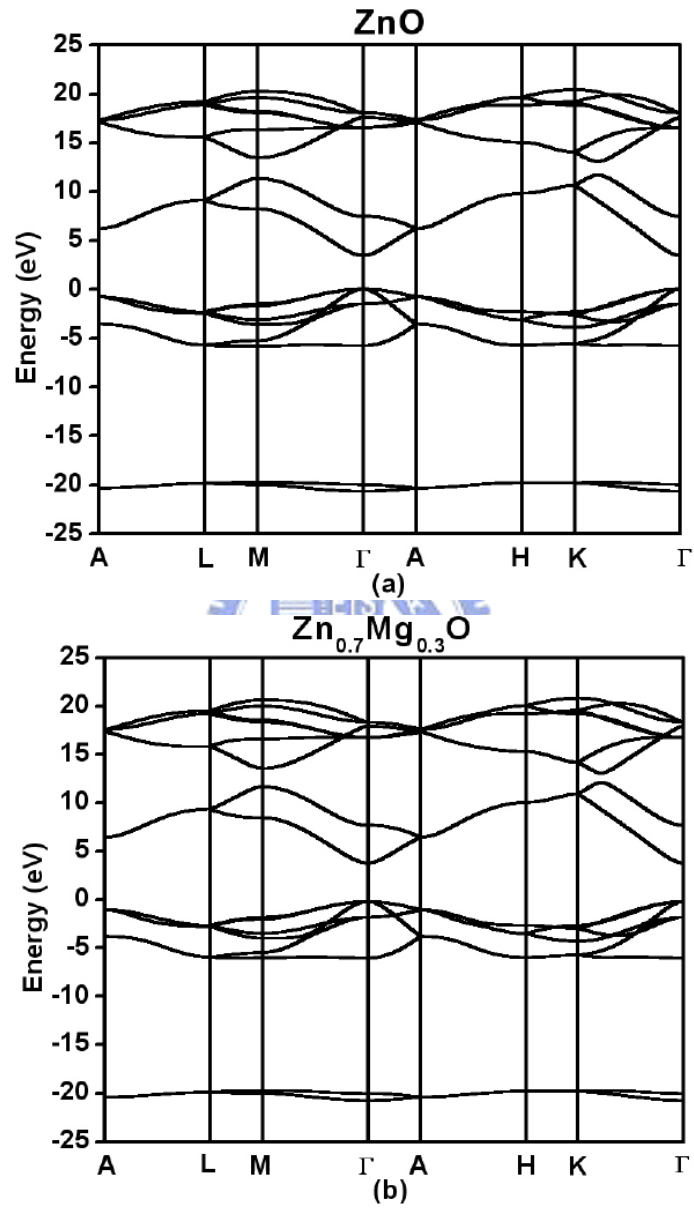


Fig. 6-1 Calculated band structure of (a) ZnO and (b) Zn_{0.7}Mg_{0.3}O using semi-empirical tight-binding model.

The deepest and lowest valence band of ZnO crystal (Fig. 6-1(a)) near -20 eV corresponds to an atomic-like $O2s$ state, and the upper valence bands are mainly composed of the $O2p$ state and $Zn4s$ and $4p$ states. The lowest conduction band is contributed by $Zn4s$ state, and the uppermost conduction bands are primarily caused by $Zn4p$ character. The ZMO is direct band gap semiconductor for all stable wurtzite structure and has band gap (at 0K) ranging from 3.429 eV for ZnO to 4.153 eV for $Zn_{0.7}Mg_{0.3}O$. In addition, we also estimate the p doubly degeneracy in valence bands with renormalized atomic spin-orbital (SO) splitting of the anion and cation p states [19]. For ZnO we got 15 meV for SO energy (Δ_0), offering a good agreement with experimental results [20], while the modification of SO energy was not conspicuously observed in $Zn_{1-x}Mg_xO$ alloy. However, we perceived that the band gap at Γ point increase as Mg concentration increases.

6.3 Energy gaps and effective masses

In Fig. 6-2 we plotted the change of the band gaps at Γ points of ZMO alloys as a function of the Mg mole fraction x along with the experimental results from the ZMO layers grown on sapphire (solid circle point) [21] and powders (hollow circle point) [20] in the range $0 < x < 0.30$. It shows very good agreement of our calculated curve with the experimental results that the band gap increases with increasing Mg concentration.

The curves can be fitted by the polynomials

$$E_g^\Gamma = 3.429 + 2.377x + 0.1349x^2 (eV), \quad (6-3)$$

although the quadratic term is referred as the band-gap bowing factor being 0.1349, which depends on the substrate on which the layer was grown [22].

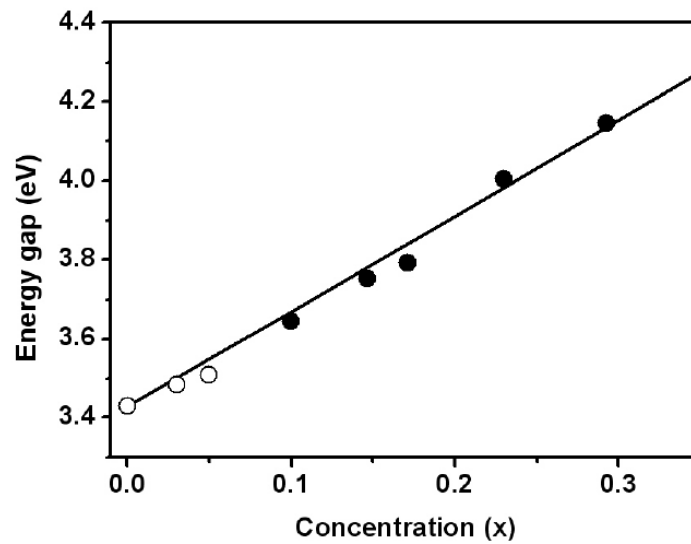


Fig. 6-2 The energy gaps of wurtzite $Zn_{1-x}Mg_xO$ alloys as a function of Mg mole fraction x . The hollow circles and solid circles show experimental data from Ref.s 20 and 21.

The effective mass is given by the curvature of the dispersion relation $E(\mathbf{k})$

according to $\left(\frac{1}{m^*}\right)_{\mu\nu} = \frac{1}{\hbar^2} \frac{d^2 E(k)}{dk_\mu dk_\nu}$, where \mathbf{k} is the wave vector of electron in the crystal,

μ and ν are Cartesian coordinates. Figure 6-3 shows the calculated effective masses for

the alloys ZMO as function of Mg concentration x . We found the electron effective mass increases when the Mg concentration increases. In ZnO wurtzite structure ($x = 0$), the electron effective masses of the lowest conduction band for parallel and perpendicular to the c -axis are $m_e^{\parallel} = 0.278m_0$ and $m_e^{\perp} = 0.202m_0$, respectively. These values agree well with experimental data of Button et al. [26] determined from the cyclotron resonance measurements.

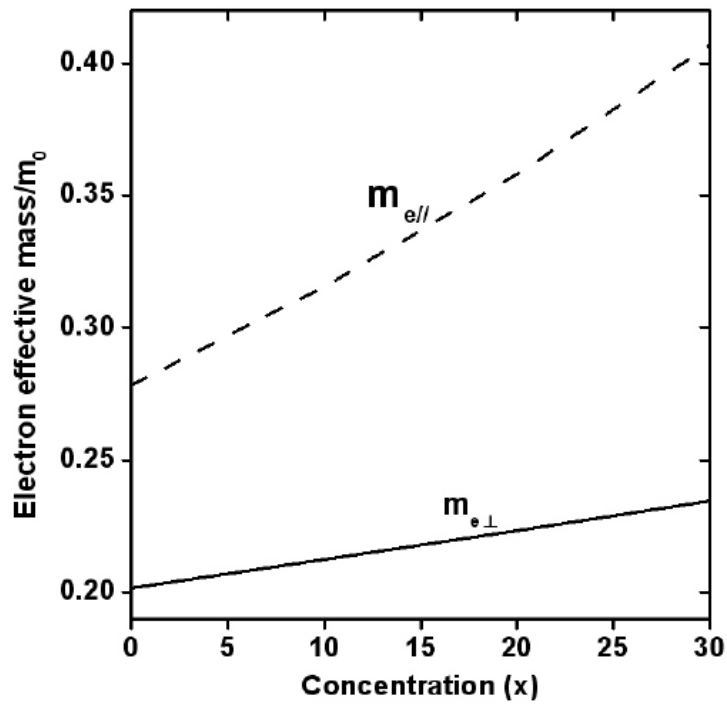


Fig. 6-3 Composition dependence of the electron effective masses. The dash line shows the electron effective mass parallel to the c -axis and the solid line is for perpendicular to the c -axis.

As aforementioned, the lowest conduction band is mainly caused by $Zn4s$ state; the electron effective masses are mainly determined by the overlapping wavefunctions of s -orbital among cation sites. Lu et al. [23] also observed the same results from the modified Burstein-Moss model in the Al doped ZMO alloys with a preferential c -axis orientation. They indicated that the electron effective masses increase with increasing Mg concentration, while the carrier mobility and electron concentration decrease. Furthermore, we note that variation of electron effective masses is more obvious for m_e^{\parallel} than for m_e^{\perp} in the ZMO alloys. Since the ZnO has wurtzite structure and the MgO is cubic, the lattice along c -axis changes more dramatically than that along a -axis as more Mg atoms substituting Zn atoms.



6.4 Density of states

We calculated the total DOS of ZMO alloys by summation over all bands using a Gaussian function with a broadening parameter of 0.01 eV, e.g., due to temperature broadening around 77K. Shown in Fig. 6-4, we obtained the similar DOS for the concentration ranging from 0 to 10%, while the DOS of upper valence bands were slightly broadened and decreased as increasing Mg incorporation (dash line). Imai et al. [24] used the first-principle pseudopotential method to show that the bond of Zn-O is

more ionic than Zn-S due to the probability of electron lingering between Zn and O is much smaller than between Zn and S. Similar to those obtained by Li et al. [25] using the first-principle calculation, the increasing probability of electron lingering between cation and anion with increasing Mg composition suggest that in the ZMO alloys the electrons from O2p orbital are less localized around the oxygen atom to cause reduction of electronegative characteristic of oxygen and ionization energy of acceptors.

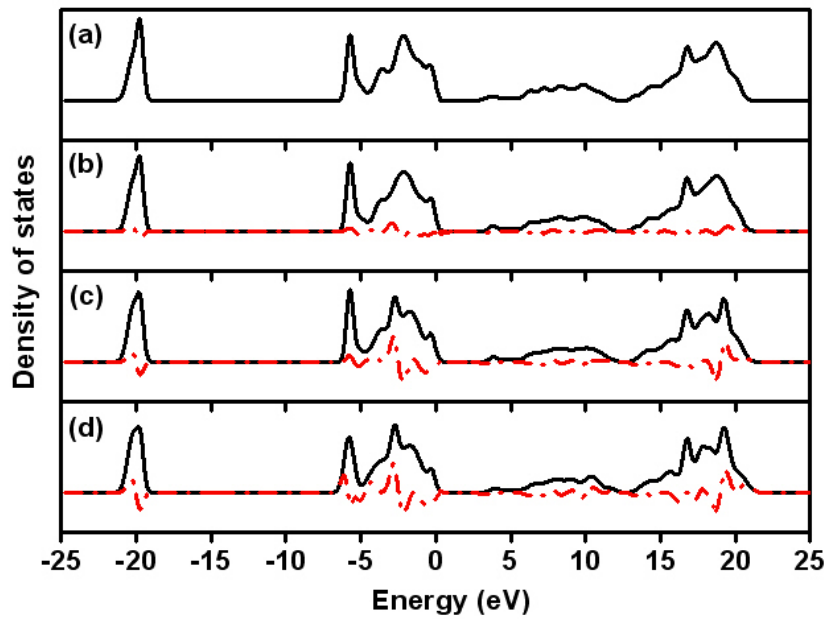


Fig. 6-4 Total density of states of various Mg concentrations in the wurtzite $Zn_{1-x}Mg_xO$ alloys: (a) 0%, (b) 10%, (c) 20%, and (d) 30%. The dash line presented discrepancy between ZnO and $Zn_{1-x}Mg_xO$ alloys structure.

Shown in Figs. 6-4(c) and 6-4(d), we found both the DOS of the upper valence band near - 2.7 eV and the uppermost conduction bands near 19 eV increase as Mg composition increases. Because the weighting of Mg's atomic orbital increases with increasing Mg concentration in the VCA method, we believe that the Mg3s orbital mainly contributes extra density of modes to the upper valence band and the Mg3p orbitals principally contribute extra density of modes to the uppermost conduction bands. We also shown the anion-atom *p-orbitals* wave function for top valence band and cation-atom *s-orbitals* wave function for lowest conduction band at Γ point in Table 6-1 and Table 6-2, respectively. Additionally, the DOS of the near lowest conduction band increases with more localized wavefunction as increasing Mg incorporation. Consequently, the more overlap of wavefunctions of the neighboring cation atoms results in narrowing the width of conduction band so that the larger effective mass. The wavefunction overlapping determines the rate of quantum tunneling of an electron from one ion to another so that the electrons hop slower from one ion to an adjacent one in the lattice with increasing Mg concentration that shows the larger effective electron mass.

Table 6-1 Anion-atom *p-orbitals* wave function for top valence band at Γ point

Mg incorporation (%)	0	10	20	30
<i>p-orbitals</i> wave function weight	0.61208	0.6108	0.60964	0.60844

Table 6-2 Cation-atom *s-orbitals* wave function for lowest conduction band at Γ point

Mg incorporation (%)	0	10	20	30
<i>s-orbitals</i> wave function weight	0.68285	0.68296	0.68304	0.68312

6.5 Summary

In conclusion, using sp^3 semi-empirical tight-binding model under virtual-crystal approximation, we have calculated the electronic band structure and the total density of states for the wurtzite structure of $Zn_{1-x}Mg_xO$ alloys semiconductor. We observed enlarging band gap and increasing electron effective mass that agree with the experimental results as increasing Mg composition up to $x = 0.3$. From the calculated total density of states, due to extra density of modes coming from $Mg3s$ and $Mg3p$ orbitals as introducing more Mg composition, the increasing electron effective mass is a result of more orbital overlap of cation sites. In addition, the $O2p$ is less localized around the oxygen atom to cause reducing electronegative characteristic of oxygen.

References

1. H. D. Sun, T. Makino, Y. Segawa, M. Kawasaki, A. Ohtomom, K. Tamura, and H. Koinuma, *J. Appl. Phys.* **91**, 1993 (2002).
2. C. J. Pan, K. F. Lin, and W. F. Hsieh, *Appl. Phys. Lett.* **91**, 111907 (2007).
3. D. B. Yao, Y. F. Chan, N. Wang, *Appl. Phys. Lett.* **81**, 757 (2002).
4. E. S. Jang, J. Y. Bae, J. Yoo, W. I. Park, D. W. Kim, G. C. Yi, T. Yatsui, and M. Ohtsu, *Appl. Phys. Lett.* **88**, 023102 (2006).
5. T. Makino, C. H. Chia, N. T. Tuan, H. D. Sun, Y. Segawa, M. Kawasaki, A. Ohtomom, K. Tamura, and H. Koinuma, *Appl. Phys. Lett.* **77**, 975 (2000).
6. P. Misra, T. K. Sharma, S. Porwal, and L. M. Kukreja, *Appl. Phys. Lett.* **89**, 161912 (2000).
7. Qingzhong Zhao, Marco Buongiorno Nardelli, and J. Bernholc, *Phys. Rev. B* **65**, 144105 (2002).
8. Fabrizio Cleri and Vittorio Rosato, *Phys. Rev. B* **48**, 22 (1993).
9. I. Shalish, H. Temkin, and V. Narayanamurti, *Phys. Rev. B* **69**, 245401 (2004).
10. T. Akiyama, K. Nakamura, and T. Ito, *Phys. Rev. B* **73**, 235308 (2006).
11. Sameer Sapra and D. D. Sarma, *Phys. Rev. B* **69**, 125304 (2004).
12. D. W. Jenkins and J. D. Dow, *Phys. Rev. B* **39**, 3317 (1989).

13. H. H. Coccoletzi, D. A. Contreras, and J. Arriaga, *Appl. Phys. A* **81**, 1029 (2005).
14. A. Kobayashi, O. F. Sankey, S. M. Volz, and J. D. Dow, *Phys. Rev. B* **28**, 935 (1983).
15. W. A. Harrison, *Electronic Structure and the Properties of Solids* (Freeman, San Francisco, 1980), p. 47.
16. L. Vegard, *Z. Phys.* **5**, 17 (1921).
17. Y.-S. Kim, E.-C. Lee, and K. J. Chang, *J. Korean Phys. Soc.* **39**, S92 (2001).
18. M. Sanati, G. L. W. Hart, and A. Zunger, *Phys. Rev. B* **68**, 155210 (2003).
19. D. J. Chadi, *Phys. Rev. B* **16**, 790 (1977).
20. C. J. Pan, K. F. Lin and W. F. Hsieh, *J. Appl. Phys.* **102**, 123504 (2007).
21. R. Schmidt, B. Rheinländer, M. Schubert, D. Spemann, T. Butz, J. Lenzner, E. M. Kaidashev, M. Lorenz, A. Rahm, H. C. Semmelhack, and M. Grundmann, *Appl. Phys. Lett.* **82**, 2260 (2003).
22. A.F. Wright, J.S. Nelson, *Appl. Phys. Lett.* **66**, 3051 (1995).
23. J. G. Lu, S. Fujita, T. Kawaharamura, H. Nishinaka, Y. Kamada, and T. Ohshima, *Appl. Phys. Lett.* **89**, 262107 (2006).
24. Y. Imai, A. Watanabe, and I. Shimono, *J. mater. sci., Mater. Electron.* **14**, 149 (2003).
25. J. Li, S. H. Wei, S. S. Li and J. B. Xia, *Phys. Rev. B* **74**, 081201 (2006).

26. K. J. Button, D. R. Cohm, M. von Ortenverger, B. Lax, E. Mollwo, and R. Helbig,
Phys. Rev. Lett. **28**, 1637 (1972).
27. E. Chementi and C. Roetti, Atomic Data and Nuclear Table **14**, 177 (1972).
28. A. Malashevich and D. Vanderbilt, Phys. Rev. B. **75**, 045106 (2007).



Chapter 7 Electronic band structures and surface states of ZnO finite well structures

Zinc oxide (ZnO) is a promising material due to its large direct band gap (3.4 eV at 5K) and large exciton binding energy of 60 meV [1], all of which are advantageous for short-wavelength light-emitting diode [2,3] and low-threshold laser [4, 5] applications at room temperature. It is known that the optical properties and the performance of photonic devices are mainly determined by their electronic density of states (DOS), which can be modified by the quantum confinement effects. ZnO nanostructures have superior optical properties over its bulk crystal, for instance, the low-dimensional ZnO nanostructures, such as QDs [6-8], nanoparticles [9, 10], nanobelts [11], nanowires [12, 13], and quantum wells [14, 15], have been widely investigated. In particular, the quantum confinement [16-19] causes the band gap and the effective masses of electron and hole having strong dependence on the size. Another difference was found that the intensity of the below-band-gap emission relative to that of the band edge emission increases as reducing the crystalline size. Recently, Shaish *et al.* [20] showed that intensity ratio of below-band-gap (surface state) and band-edge luminescence in ZnO nanowires depend on the wire radius. The weight of this surface luminescence increases as the wire radius decreases at the expense of the band-edge emission. Pan *et al.* [21]

also predicated a significant increase in the intensity ratio of the deep level to the near band edge emission with ever-increasing nanorod surface-aspect ratio. Thus, in quantum-size nanostructures, the surface-recombination may entirely quench band-to-band recombination, presenting an efficient sink for charge carriers that unless deactivated may be detrimental for electronic devices. Nevertheless, it is still lack of theoretical study on the influences of the crystalline size on electronic structure and surface states in ZnO.

In comparison of simulation methods for nanostructures, the application of the *ab initio* calculation, a self-consistent method such as using local density approximation (LDA), to study electronic band structures of nanostructures or disordered alloys generally requires using very large supercells in order to mimic the distribution of local chemical environments. It is very computationally demanded. On the other hand, the tight-binding (TB) theory is a versatile and simple method to calculate the electronic properties of solids. Additionally, due to the transferability of the TB parameters, the method has been readily applied to systems with broken translational invariance such as low-dimensional structures [29, 30], clusters [31, 32] and alloys [24, 33]. Accordingly, in this chapter, we used TB method to investigate the electronic structure and surface states of ZnO finite well structures considering non-relaxed and non-reconstructed

surfaces along $\langle 0001 \rangle$ and $\langle 1-100 \rangle$ growth directions.

7.1 Computation method details and parameters

ZnO has the wurtzite structure semiconductors which are the layered materials, in which cation and anion layers alternate on the $\{0001\}$ planes. The unit cell of wurtzites built on the unit vectors $\vec{a}_1 = (\sqrt{3}a/2, -a/2, 0)$, $\vec{a}_2 = (0, a, 0)$ and $\vec{c} = (0, 0, c)$, consisting of two cations and two anions. We used a SETB method with a sp^3 basis set [22-24], which has been proven suitable for bulk wurtzite crystals. In the present calculations, the four nearest neighbor atoms are considered equivalent, even though the crystal is not cubic. The small crystal-field splittings which differentiate the p_z orbital from the $p_{x,y}$ orbitals are neglected. Under such an approximation, on-site coupling between s and p_z orbitals can also be neglected. Thus, the model has nine independent parameters including four on-site matrix elements $E(s, a)$, $E(p, a)$, $E(s, c)$, and $E(p, c)$ (where s and p refer to the basis states, and a and c refer to anion and cation) and five nearest-neighbor transfer matrix elements $V(ss\sigma)$, $V(sp\sigma)$, $V(ps\sigma)$, $V(pp\pi)$, and $V(pp\sigma)$, where the first and second indices refer to anion and cation with σ and π bondings. We used the tight-binding parameters from Refs. 22 in our numerical calculation which along with the lattice parameters a and c are listed in Table I.

Table 7.1 Tight-binding parameters (in eV) and lattice parameters (in Å) for bulk ZnO.

$E(s, a)$	$E(p, a)$	$E(s, c)$	$E(p, c)$	$V(ss\sigma)$	$V(sp\sigma)$	$V(ps\sigma)$	$V(pp\pi)$	$V(pp\sigma)$	a	c
-19.046	4.142	1.666	12.368	-6.043	7.157	10.578	4.703	8.634	3.249	5.21

Let us first consider the finite well structures grown along $\langle 0001 \rangle$ direction or called the [0001] slab, the atoms in each of the layers are arranged in a hexagonal lattice with the unit cell defined by vectors \vec{a}_1 and \vec{a}_2 . We assume that the layer is infinitely large and its structure being perfect (no reconstruction and relaxation on the end surfaces). We can see from Fig. 7-1(a) that the distance between the identical successive layers in such a structure is equal to c , so that the unit cell consists of four sublayers: two cation layers and two anion layers. Since, The wave function should be written as a superposition of the localized cation, ϕ_α^{ci} , and anion, ϕ_α^{ai} , atomic orbitals $\alpha=s, p_x, p_y, p_z$ in each sublayer:

$$\Psi(\vec{r}) = \frac{1}{\sqrt{N}} \sum_{\alpha, \vec{R}, l} e^{i\vec{k} \cdot \vec{R}} [A_{\alpha, l} \phi_\alpha^{c1}(\vec{r} - \vec{R}) + B_{\alpha, l} \phi_\alpha^{a1}(\vec{r} - \vec{R}) + C_{\alpha, l} \phi_\alpha^{c2}(\vec{r} - \vec{R}) + D_{\alpha, l} \phi_\alpha^{a2}(\vec{r} - \vec{R})] \quad (7-1)$$

Here $A_{\alpha, l}, B_{\alpha, l}, C_{\alpha, l}$, and $D_{\alpha, l}$ describe the amplitude of the atomic orbitals in each sublayer of the l th unit cell; N is the number of unit cells in each sublayer; $\vec{R} = n_1 \vec{a}_1 + n_2 \vec{a}_2$ ($n_{1,2}$ are integers) is the lattice vector in the plane of each sublayer; \vec{k} is the momentum lying

in the hexagonal surface Brillouin zone defined by reciprocal vectors $\vec{b}_1 = 2\pi/a(2/\sqrt{3},0)$

and $\vec{b}_2 = 2\pi/a(1/\sqrt{3},1)$.

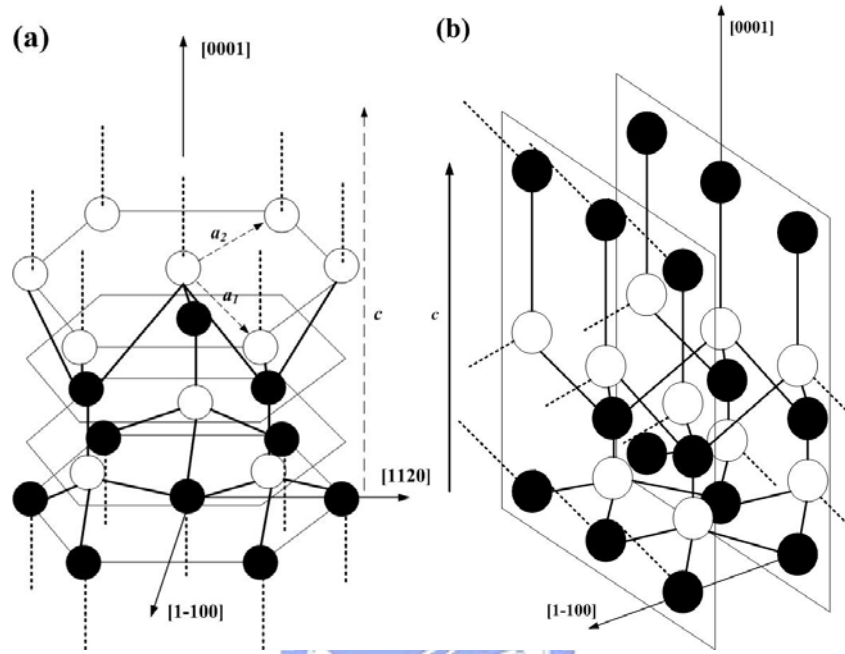


Fig. 7-1 Finite well structures of wurtzite material. (a) The slab of one layer grown along the [0001]

direction. (b) The slab of two layers grown along the [1-100] direction. a_1 , a_2 , and c are the unit vectors in

a unit cell; dashed lines represents for dangling bonds on surfaces; open and closed circles show the cation

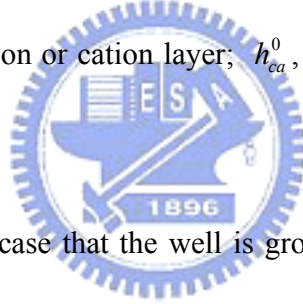
and anion atoms, respectively.

In the nearest-neighbor approximation, the band structure of such a layered structure is

determined by the following matrix equation:

$$\begin{pmatrix} h_c^0 - EI & h_{ca}^+ & 0 & 0 & 0 & \cdots & 0 & 0 \\ h_{ca} & h_a^0 - EI & h_{ac} & 0 & 0 & \cdots & 0 & 0 \\ 0 & h_{ac}^+ & h_c^0 - EI & h_{ca}^{0+} & 0 & \cdots & 0 & 0 \\ 0 & 0 & h_{ca}^0 & h_a^0 - EI & h_{ac} & \cdots & 0 & 0 \\ \vdots & \vdots & \vdots & \vdots & \vdots & \vdots & \vdots & \vdots \\ \vdots & \vdots & \vdots & \vdots & \vdots & \vdots & \vdots & \vdots \\ 0 & 0 & 0 & 0 & \cdots & h_{ac}^+ & h_c^0 - EI & h_{ca}^{0+} \\ 0 & 0 & 0 & 0 & \cdots & 0 & h_{ca}^0 & h_a^0 - EI \end{pmatrix} \begin{pmatrix} A_l \\ B_l \\ C_l \\ D_l \\ \vdots \\ C_L \\ D_L \end{pmatrix} \quad (7-2)$$

In the tight-binding basis used each block h represents a 4×4 matrix, I is the identity matrix, and A_l , B_l , C_l , and D_l are the column vectors of size 4. The coupling matrices h are determined by the empirical parameters of the model and the wave vector \vec{k} . $h_{c,a}^0$ describe on-site coupling in anion or cation layer; h_{ca}^0 , h_{ac} , and h_{ca} describe interlayer coupling.



We also consider another case that the well is grown along $\langle 1-100 \rangle$ and represent the structure of a wurtzite crystal as the $[1-100]$ slab. Each surface atom forms one dangling bond tilted to the end surface as shown in Fig. 7-1(b). The separation between the equivalent layers in such a structure is equal to $\sqrt{3}a/2$, so that the unit cell includes two sublayers. In turn, the atoms in each sublayer are arranged in rectangular lattice with a unit cell defined by the vectors $\vec{a}_1 + \vec{a}_2$ and \vec{c} . The surface unit cell includes two atoms one cation and one anion, which are shifted with respect to each other by the vector $\vec{\tau} = (3/8)\vec{c}$. Therefore, in terms of the nearest neighbors, the $[1-100]$ surface

can be represented as cation-anion dimmers directed along the $\langle 0001 \rangle$ axis. Thus, the wave function of the wurtzite structure perpendicular to the axis $\langle 1-100 \rangle$ should be written as a superposition of the localized cation and anion atomic orbitals in the l -th layer including two sublayers:

$$\begin{aligned} \Psi(\vec{r}) = & \frac{1}{\sqrt{N}} \sum_{\alpha, \vec{R}, l} e^{i\vec{k} \cdot \vec{R}} [A_{\alpha, l}^c \phi_{\alpha}^{c1}(\vec{r} - \vec{R}) + A_{\alpha, l}^a e^{i\vec{k} \cdot \vec{\tau}} \phi_{\alpha}^{a1}(\vec{r} - \vec{R} - \vec{\tau}) \\ & + B_{\alpha, l}^c \phi_{\alpha}^{c2}(\vec{r} - \vec{R}) + B_{\alpha, l}^a e^{i\vec{k} \cdot \vec{\tau}} \phi_{\alpha}^{a1}(\vec{r} - \vec{R} - \vec{\tau})] \end{aligned} \quad (7-3)$$

where the vector $\vec{R} = n_1(\vec{a}_1 + \vec{a}_2) + n_2\vec{c}$ runs over the lattice sites in each sublayer, the momentum \vec{k} lies in the rectangular surface Brillouin zone built on the reciprocal vectors $\vec{b}_1 = 2\pi/a(1,0)$ and $\vec{b}_2 = 2\pi/c(0,1)$; and the indices c and a in the amplitudes A and B refer to cation and anion atoms in each sublayer, respectively. The formal eigenvalue problem for such an infinitely long layered structure is reduced to

$$\begin{pmatrix} H_0 - EI & H_{01} & 0 & 0 & 0 & \dots & 0 & 0 & 0 \\ H_{01}^+ & H_0 - EI & H_{10}^+ & 0 & 0 & \dots & 0 & 0 & 0 \\ 0 & H_{01} & H_0 - EI & H_{01} & 0 & \dots & 0 & 0 & 0 \\ 0 & 0 & H_{01}^+ & H_0 - EI & H_{10}^+ & \dots & 0 & 0 & 0 \\ \vdots & \vdots & \vdots & \vdots & \vdots & \ddots & \vdots & \vdots & \vdots \\ 0 & 0 & 0 & 0 & 0 & \dots & H_{01} & H_0 - EI & H_{01} \\ 0 & 0 & 0 & 0 & 0 & \dots & 0 & H_{01}^+ & H_0 - EI \end{pmatrix} \begin{pmatrix} A_1 \\ B_1 \\ A_2 \\ B_2 \\ \vdots \\ A_L \\ B_L \end{pmatrix} \quad (7-4)$$

Here we defined 8×8 H matrices as

$$H_0 = \begin{pmatrix} h_c^0 & h_{ca}^0 \\ h_{ca}^{0+} & h_a^0 \end{pmatrix}, \quad H_{01} = \begin{pmatrix} 0 & h_{ca} \\ h_{ac} & 0 \end{pmatrix}, \quad H_{01} = \begin{pmatrix} 0 & \tilde{h}_{ca} \\ \tilde{h}_{ac} & 0 \end{pmatrix}. \quad (7-5)$$

The matrices h depend on the surface wave vector \vec{k} , which lies in the rectangular surface

Brillouin zone in this case. Hence, the coupling matrices h are not identical to the h matrices for the [0001] surface in Eq. (2). $h_{c,a}^0$ describe on-site coupling in anion or cation layer; h_{ca}^0 , h_{ac} , and h_{ca} describe inter-sub-layer coupling in one layer; \tilde{h}_{ac} , and \tilde{h}_{ca} describe the inter-sub-layer coupling between two layers.

7.2 Transfer matrix technique and surface states

We analyze the surface states of semi-infinite wurtzites in terms of the transfer-matrix technique [25]. The basic concept of this approach is that wave functions are matched from layer to layer through a transfer matrix. We represent the crystal as a sequence of layers parallel to the surface in above question. The next problem is to construct the transfer matrix. Knowing the transfer matrix we can immediately find the wave function on each layer. Finally, by setting relevant boundary conditions, the surface state spectrum can be calculated. Let us first consider the surfaces of polar surfaces [0001] and [000-1]. We can see from Eq. (7-2) that the adjacent identical layers are linked through the so-called transfer matrix T :

$$\begin{pmatrix} A_{l+1} \\ B_{l+1} \\ C_{l+1} \\ D_{l+1} \end{pmatrix} = \begin{pmatrix} T_{AB} & 0 \\ 0 & T_{CD} \end{pmatrix} \begin{pmatrix} A_l \\ B_l \\ C_l \\ D_l \end{pmatrix} \quad (7-6)$$

The matrix T_{AB} is defined as

$$T_{AB} = \begin{pmatrix} 0 & h_{ac} \\ h_{ca}^{0+} & (h_c^0 - EI) \end{pmatrix}^{-1} \begin{pmatrix} (h_a^0 - EI) & h_{ca} \\ h_{ac}^+ & 0 \end{pmatrix} \begin{pmatrix} 0 & h_{ac} \\ h_{ca}^+ & (h_c^0 - EI) \end{pmatrix}^{-1} \begin{pmatrix} (h_a^0 - EI) & h_{ca}^0 \\ h_{ac}^+ & 0 \end{pmatrix} \quad (7-7)$$

The expression for T_{CD} can be obtained from T_{AB} by two cyclic permutations of the matrix blocks in (7-2). For the eigenvalues $|\lambda| \leq 1$, the solution of the problem

$$\begin{pmatrix} T_{AB} & 0 \\ 0 & T_{CD} \end{pmatrix} \begin{pmatrix} A_0 \\ B_0 \\ C_0 \\ D_0 \end{pmatrix} = \lambda \begin{pmatrix} A_0 \\ B_0 \\ C_0 \\ D_0 \end{pmatrix} \quad (7-8)$$

defines the band structure projected on the surface and the wave function in the 0th unit cell. By inserting then the recursion relation (7-6) into Eq. (7-1) we can formally define the wave function in the whole crystal.

From Fig. 7-1(a) we can see that there are two ways to terminate the crystal perpendicular to the axis $\langle 0001 \rangle$: by a cation layer (surface $[0001]$) or an anion layer (surface $[000-1]$). Then, applying the relevant boundary conditions, we get the dispersion relation for the case of a cation-terminated surface

$$(h_c^0 - EI)D_0 + h_{ca}^+ C_0 = 0 \quad (7-9)$$

and for the case of an anion-terminated surface

$$(h_a^0 - EI)A_0 + h_{ca}^0 B_0 = 0 \quad (7-10)$$

The solution of these equations completely determines the surface spectrum both for the

surface states and for the surface wave functions.

In Fig. 7-2 we present the surface spectrum for the [0001] and [000-1] surfaces of ZnO. The shaded region demonstrates the projected band structure in the surface Brillouin zone (see inset). The dots and stars show the surface bands for the cation- and anion-terminated surfaces, respectively.

We can see that the dangling bonds of the cations (Zn) result in a surface band close to the bottom of the conduction band, while the dangling bonds of the anions (O) give rise to a surface band near the top of the valence band. This is in agreement with the origin of the conduction (valence) band mostly from the cation (anion) atomic orbitals.

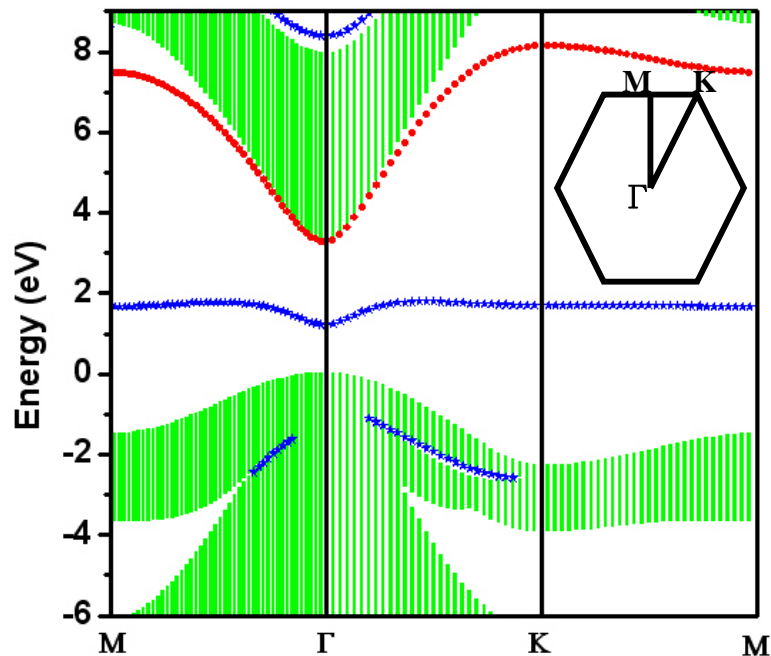


Fig. 7-2 (Color online) Projected band structure of the ideal [0001] and [000-1] surfaces of ZnO. The

dashed region shows the continuum in the surface Brillouin zone illustrated in the inset. The dots and stars show the localized surface states for the cation- and anion-terminated surfaces, respectively.

We consider next the surface [1-100] and represent the structure of a wurtzite crystal as layers perpendicular to [1-100]. The transfer matrix T , which connects the wave functions in the consecutive layers, can be found from Eq. (7-4) as follows:

$$T = \begin{pmatrix} -H_{01}^{-1}(H_0 - EI) & -H_{01}^{-1}H_{10} \\ I & 0 \end{pmatrix} \begin{pmatrix} -(H_{01}^+)^{-1}(H_0 - EI) & -(H_{01}^+)^{-1}H_{10} \\ I & 0 \end{pmatrix} \quad (7-11)$$

By solving the eigenvalue problem for the T matrix,

$$(T - \lambda I) \begin{pmatrix} A_0 \\ B_0 \end{pmatrix} = 0, \quad (7-12)$$

we get, for $|\lambda| \leq 1$, the projected band spectrum in the surface Brillouin zone and the wave function (A_0 and B_0) in the $0th$ unit cell. Then by setting the boundary condition $B_{-1}=0$, we find the dispersion relation for the surface states:

$$(H_0 - EI)A_0 + H_{01}B_0 = 0 \quad (7-13)$$

Using the transfer matrices Eq. (7-11) for the surfaces [1-100] and relevant dispersion equations (7-13), we showed the projected band structure and surface states for the ideal surface [1-100] of ZnO in Fig. 7-3.

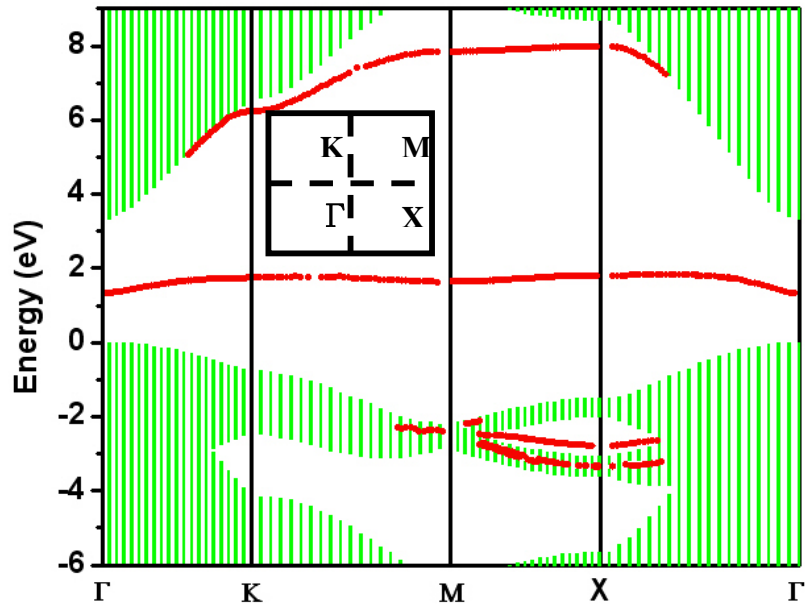


Fig. 7-3 (Color online) Projected band structure of the ideal surfaces [1-100] of ZnO. The dashed region shows the continuum in the surface Brillouin zone illustrated in the inset. The markers show the surface bands.



We can see that each dangling bond per surface unit cell results in one surface state inside the band gap. Therefore, we found two surface bands inside the band gap for the surface [1-100] in Fig. 7-3. These states are more strongly localized at the surface the deeper they fall inside the band gap. The strength of the localization is determined by the decay length d . In terms of the transfer-matrix model, the decay length is [25,26]:

$$d = \frac{-1}{\ln|\lambda|} \quad (7-14)$$

Here λ is the eigenvalue corresponding to the surface state, which should be found

from the condition $\det(T - \lambda D) = 0$. For example, for the surface [1-100], the surface state $E_s = 5.06$ eV, at the near the conduction band, has the decay length $d = 5.66\sqrt{3}a/2$ (in unit of separation between layers), while for the state $E_s = 1.3$ eV at point Γ , which lies deeper inside the band gap, $d = 12.7\sqrt{3}a/2$.

7.3 Surface states of nanowire with identical lateral facets

We have analyzed the surface spectrum of the semiinfinite wurtzite crystal. Now we want to understand how the spectrum will change on the surface of a nanowire. Let us consider a wurtzite nanowire surrounded by the identical lateral facets [1-100]. First of all, we note that the surface spectrum and the wave function of each equivalent facet should be identical. The cross section of the nanowire under investigation is hexagonal, we can assume that the cation-anion dimers wrap the nanowire along the lateral surface of a hexagonal prism, which is encircled by a cylinder of radius R equal to that of the nanowire as shown in Fig. 7-4.

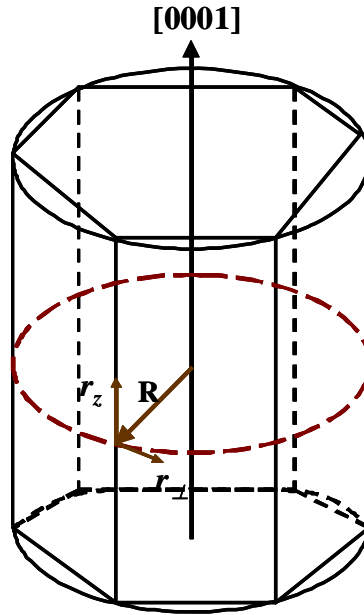
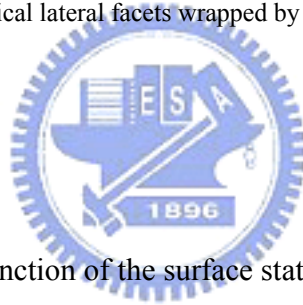


Fig. 7-4 Wurtzite nanowire with identical lateral facets wrapped by a cylinder of radius R equal to the radius of nanowire.



By definition (7-3), the wave function of the surface state is a Bloch function

$$\Psi(r_{\perp}, r_z) = u_k(\vec{r}) e^{i(k_{\perp} r_{\perp} + k_z r_z)} \quad (7-15)$$

What is important is that this wave function depends on the surface vector $\vec{r} = \vec{r}_{\perp} + \vec{r}_z$ with the components \vec{r}_{\perp} (perpendicular) and \vec{r}_z (parallel) to the nanowire axis as shown in Fig. 7-4. Accordingly, the momentum $\vec{k} = \vec{k}_{\perp} + \vec{k}_z$ should be decomposed into the components $\vec{k}_{\perp} \parallel \Gamma X$ and $\vec{k}_z \parallel \Gamma K$ see inset in Fig. 7-3. The periodic function $u_k(\vec{r})$ is defined by

$$u_k(\vec{r}) = \frac{1}{\sqrt{N}} \sum_{\alpha, \vec{R}} e^{i\vec{k} \cdot (\vec{R} - \vec{r})} [A_{\alpha,0}^c \phi_{\alpha}^{c1}(\vec{r} - \vec{R}) + A_{\alpha,0}^a e^{i\vec{k} \cdot \vec{\tau}} \phi_{\alpha}^{a1}(\vec{r} - \vec{R} - \vec{\tau}) + B_{\alpha,0}^c \phi_{\alpha}^{c2}(\vec{r} - \vec{R}) + B_{\alpha,0}^a e^{i\vec{k} \cdot \vec{\tau}} \phi_{\alpha}^{a1}(\vec{r} - \vec{R} - \vec{\tau})] \quad (7-16)$$

In the case of the semi-infinite crystal, the lattice vector \vec{R} runs over N sites of the one [1-100] surface, while in the case of the nanowire, \vec{R} runs over N sites of the six identical [1-100] surfaces. On the surface of a nanowire with hexagonal cross section, the wave function (7-15) must satisfy the cyclic boundary conditions

$$\Psi(r_{\perp} + 6R, r_z) = u_k(r_{\perp} + 6R, r_z) e^{i[k_{\perp}(r_{\perp} + 6R) + k_z r_z]} = u_k(r_{\perp}, r_z) e^{i(k_{\perp} r_{\perp} + k_z r_z)} \quad (7-17)$$

Taking into account the periodicity of the function $u_k(\vec{r})$, we obtain that this boundary condition can be satisfied only at discrete values of the wave vector perpendicular to the axis of the nanowire:

$$k_{\perp} R = \frac{n\pi}{3} \quad \text{for any } n=1,2,3,\dots \quad (7-18)$$

As a result the dispersion equation (7-13) will be reduced to

$$\left[H_0 \left(k_{\perp} R = \frac{n\pi}{3}, k_z \right) - EI \right] A_0 + H_{01} \left(k_{\perp} R = \frac{n\pi}{3}, k_z \right) B_0 = 0 \quad (7-19)$$

Fig. 7-5 demonstrates the dispersion of quantized levels of the surface bands through the Brillouin zone of the nanowire, $\vec{k}_z = [0, \pi/c]$, with the vector k_z being parallel to the Γ \mathbb{K} direction of the surface Brillouin zone. We present here the data for the two surface bands close to the conduction (Figs. 7-5 (a) and 7-5 (b)) and valence bands (Figs. 7-5 (c) and 7-5 (d)) for ZnO nanowires with radius equal to $20a$ (~80 nm) and $10a$ (~40 nm) in

Figs. 7-5 (a) and 7-5 (c) and in Figs. 7-5 (b) and 7-5 (d), respectively.

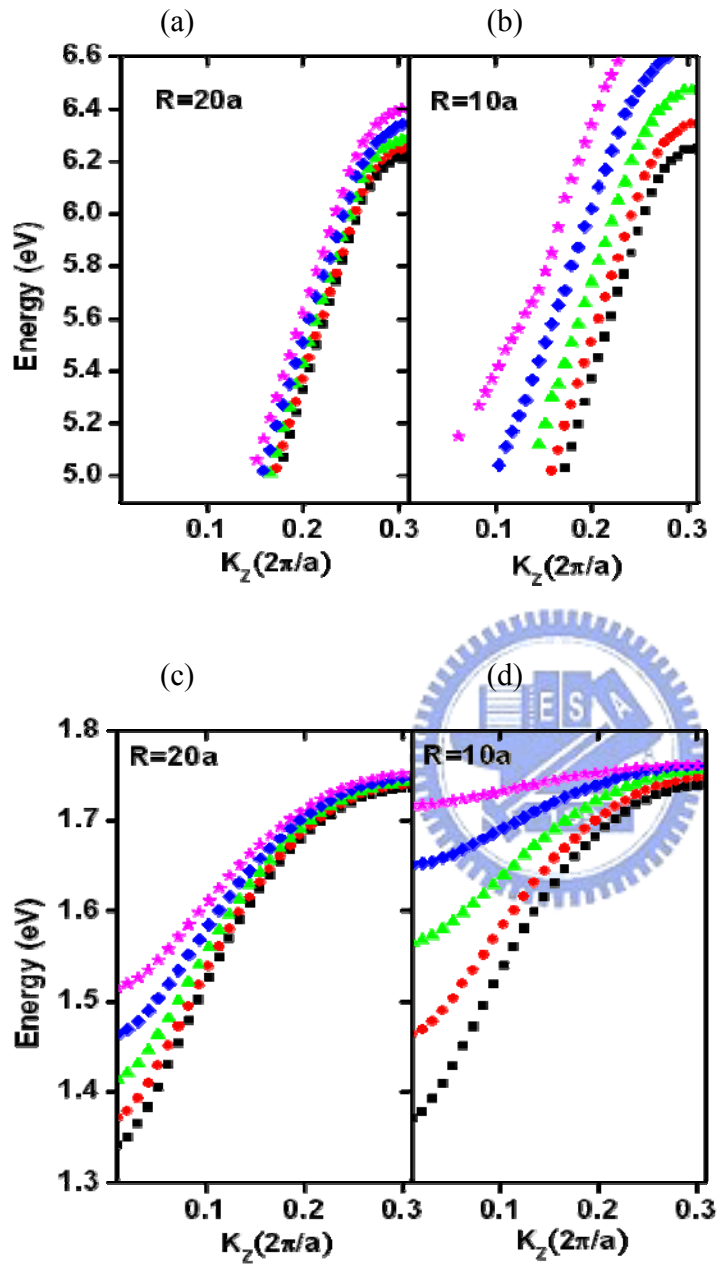


Fig. 7-5 (Color online) Surface spectrum of GaN nanowire surrounded by identical [1-100] lateral facets with radius $R=20$ u.c. (a), (c) and 10 u.c. (b), (d). The two surface bands close to the conduction (a), (b) and valence bands (c), (d) are shown.

We note that, at room temperature, because of temperature broadening, the quantized surface spectrum can be distinguished only for the surface band close to the conduction band (Figs. 7-5 (a) and 7-5 (b)). As we see from Figs. 7-5 (c) and 7-5 (d), the quantized levels of surface band close to the valence band can be distinguished only at low temperature. At room temperature the spectrum of this band can be considered as quasicontinuous.

7.4 Band structures for polar and nonpolar surface layers

In this section, we solved eigenvalue problem of Eq. (7-2) and Eq. (7-4) to obtain electronic behavior for ZnO finite well structures for different direction. In Figs. 7-6(a) and 7-6(b), we overlaid the band structures (solid curves) of the five-layers [0001] and [1-100] ZnO slabs, respectively, on the projected band structures (shaded regions) of bulk crystal using the approach described in above. The extrema of the conduction and the valence bands of the bulk ZnO are found to be $E_c = 3.36$ eV and $E_v = 0$ eV, respectively. In the above calculation, we used the transfer matrix method to prove that the dangling bonds of the cations (Zn) result in a surface band as a solid curve close to the bottom of the conduction band in Fig. 7-6(a), while the dangling bonds of the anions (O) give rise to the surface bands near the middle of the band gap (around 1.3 eV). This is in agreement

with the origin of the conduction (valence) band mostly from the cation (anion) atomic orbitals [22, 24]. We also perceived that there are energy dips at the midst of band gap for the oxide-settled surface bands at the Γ point. The depth of energy dip is function of slab thickness that may be caused by coupling between the O- and Zn-terminated surfaces. Further study to clarify this problem is required and is under the way. In Fig. 7-6 (b), we can see that the band gap of the slab is formed by four bands, which include two bands slightly above the bottom of conduction band and other two bands in the middle of the band gap at the Γ point. Particularly, we observed the splitting of these bands around the neighborhood of the Γ point and the difference between the near-conduction bands and the middle-gap bands decrease with increase in the slab thickness. On the other hand, there is strong coupling between the surface states with the allowed bands especially at the Γ point. In order to eliminate these coupling effects, we calculated the wave functions for the parallel (to the layers of the well) wave vector, $k_{//}$, away from the Γ point for ensuring accurately characterizing the properties of surface states.

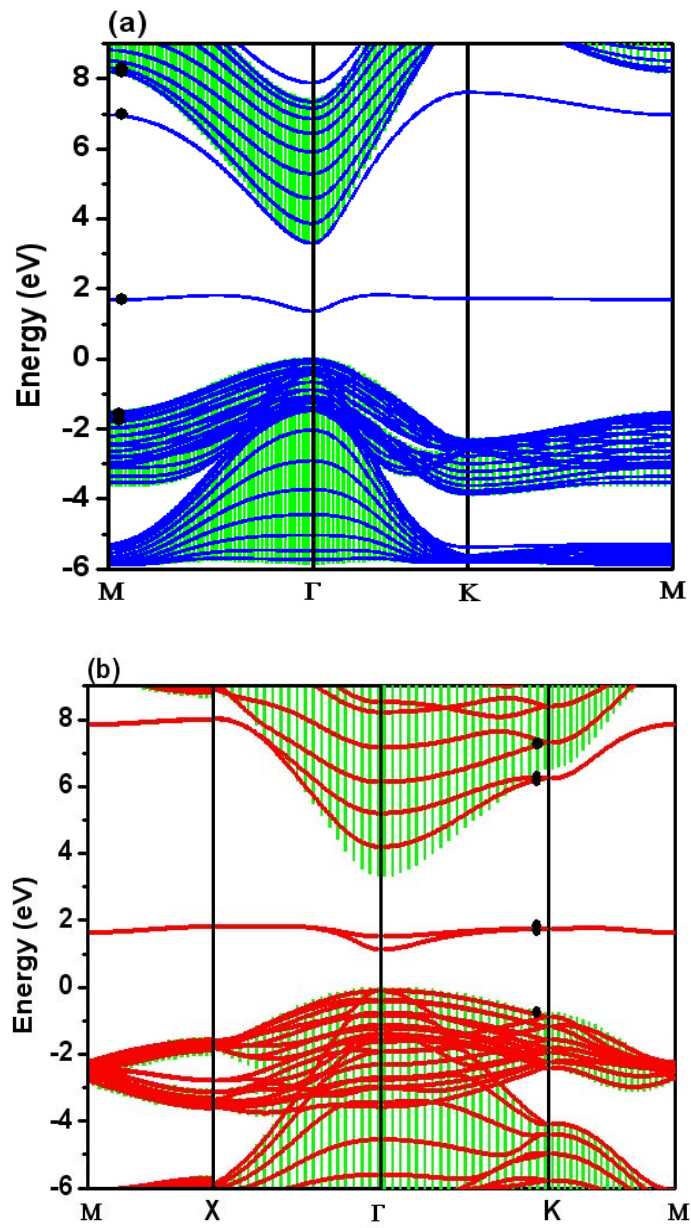


Fig. 7-6 The band structures of the ZnO slabs with five layers along (a) polar and (b) nonpolar surface layers. The solid curves are the surface states and the shaded regions show the projected band structure of the bulk.

7.5 Wave function and quantum effect for ZnO finite well

The wave functions $|\Psi|$ of the six bands for the [0001] slab of 5 layers close to the M point being labeled in Fig. 7-6(a) are shown in ascending energy order in Fig. 7-7(b). And the wave functions with the same $k_{//}$ for the 2 and 10 layers slabs were also plotted in Fig. 7-7(a) and 7-7(c), respectively. Analyzing the wave functions across the [0001] slabs in Fig. 7-7(a)-(c), we can see that the bands (the first and second bands) near the conduction band edge are mainly contributed by cation layers with high $|\Psi|$ being located at the cation sites, and the upper valence bands (the fifth and sixth bands) are mainly contributed by the anion layers with high $|\Psi|$ being located at the anion sites.

Observably, the wave function (the third curve) of the closest (surface) band to the conduction band edge is localized in the top cation-terminated layer and the surface band at the midgap (~ 1.3 eV) is localized in the bottom anion-terminated layer. Our calculations are consistent with the results of Kresse *et al.* [27] which calculated Zn-terminated surface and O-terminated surface using the density-functional theory.

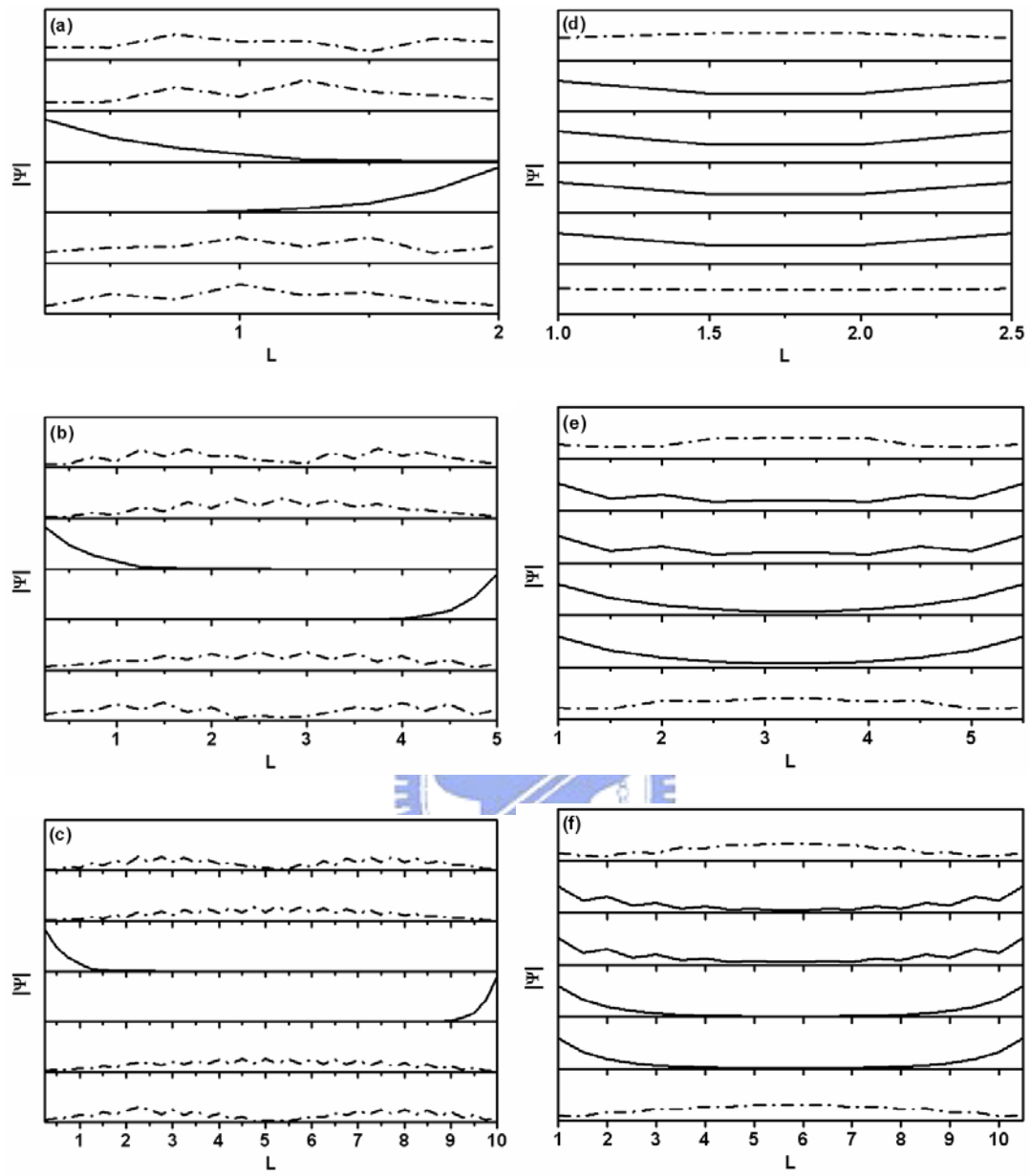


Fig. 7-7 The wave functions of the six bands closest to the middle of the band gap away from Γ point for the slabs of two, five, and ten layers along $[0001]$ (a)-(c) and along $[1-100]$ (d)-(f).

Similarly, in order to eliminate the strong coupling between the surface states with the allowed bands close to the Γ point we plotted the wavefunctions of the [1-100] slabs with thickness $L = 2, 5,$ and 10 layers near the K point in Fig. 7-7(d)-(f). We can see that besides the wavefunctions of these two midgap bands (the second and the third) there are other two bands (the fourth curves the fifth curves) show a tendency toward surface localization. Theoretically [28], these four bands should be considered as surface bands induced by the dangling bonds, in contrast to the allowed bands induced by the atoms in the interior layers (the first and the sixth bands).

The surface state is induced by each dangling bond in a unit cell of the end-surface. The coupling of the degenerate surface states on the periodic surface generates a surface band in the surface Brillouin zone. Furthermore, the coupling between these two identical end-surfaces sandwiching the slab causes their degenerate bands to split into symmetrical and antisymmetrical bands. The larger overlap of the wave functions of the degenerate bands will cause the larger energy-splitting. As a result, the splitting of the degenerate surface bands increases with decrease in the thickness of the slab. However, the energy-splitting will not be perceived for the [0001] slabs, since the polar end-surfaces are not identical. Another important consequence is that the splitting at the Γ point is the largest in comparison with that at the other Brillouin-zone boundaries. As

in Fig. 7-6 (b) of the five layers [1-100] slab, the two higher surface bands near the Γ point embedded themselves in the conduction band of the bulk. These bands as expected shift toward the conduction band edge of the bulk with increasing L . In general, a localization length of surface state is inversely proportional to its energy separation from the related allowed band [28]. Since the surface bands more closely approach the allowed conduction and valence bands near the Γ point, their localization length must be longer at the Γ point than at the other $k_{//}$ in the Brillouin zone. The larger localization length at the Γ point results in the larger overlap between the degenerate surface states, which explains the largest splitting of the bands at the Γ point. Additionally, we also noted in Fig. 7-8 that the edges of conduction and valence bands shift towards each other so as the band gap decreases with increasing L . As a matter of fact, this is a direct evidence of the quantum size effect. Obviously, the enhancing the band gap have more effective carrier confinement in c-axis rather than in other direction. And both the band structure of the slab and the surface bands become similar to those of semi-infinite crystal with increase in the number of layers and the bands finally bundle to form the band spectrum of the bulk.

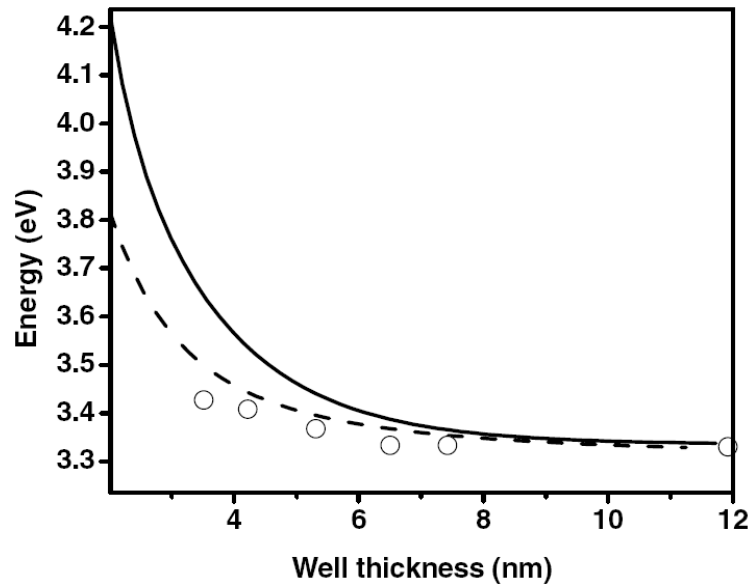


Fig. 7-8 Variations of the band gap as a function of the thickness for ZnO well along [0 0 0 1] (solid curve), [1-1 0 0] (dashed curve) directions and experiment data (hollow circle point).

7.6 Summary

In summary, using tight binding representation of the layered systems grown along $\langle 0001 \rangle$ and $\langle 1-100 \rangle$ directions, we calculated the band structures and wave functions for various ZnO slab layers with non-relaxed and non-reconstructed surfaces. We first calculate the surface spectrum of a semi-infinite crystal using the transfer-matrix technique. Then, using cyclic boundary conditions, we calculate the quantized spectrum of the surface states in nanowires. We find that the spectrum of the nanowire surfaces consists of a number of quantized levels inside the band gap. We show that dangling bonds on the two end-surfaces cause surface bands for different direction grown slabs.

Analyzing the wave functions across the layers, the surface states show a tendency toward surface localization. Particularly, the splitting of the degenerate surface bands increase due to increasing overlap between their wave functions, which are localized on two nonpolar [1-100] end-surfaces, while it is not present for the [0001] finite well with polar end-surfaces. Finally, we also found that the enhancing the band gap along [0001] polar due to more effective carrier confinement in c-axis.



References

1. K. Hümmer, Phys. Status Solidi B. **56**, 249 (1973).
2. A. Nadarajah, R. C. Word, J. Meiss, R. Konenkamp, Nano Lett. **8**, 534 (2008).
3. H. Sun, Q. Zhang, J. Zhang, T. Deng, J. Wu, Appl. Phys. B. **90**, 543 (2008).
4. G. A. Emel'chenko, A. N. Gruzintsev, A. B. Kulakov, E. N. Samarov, I. A. Karpov, A. N. Red'kin, E. E. Yakimov, C. Barthou, Semiconductors **41**, 176 (2007).
5. C. Bouvy, E. Chelnokov, R. Zhao, W. Marine, R. Sporcken, B. L. Su, Nanotechnology **19**, 105710 (2008).
6. V. A. Fonoberov and A. Balandin, Appl. Phys. Lett. **85**, 5971 (2004).
7. H. M. Cheng, K. F. Lin, H. C. Hsu, and W. F. Hsieh, Appl. Phys. Lett. **88**, 261909 (2006).
8. K. F. Lin, H. M. Cheng, H. C. Hsu, and W. F. Hsieh, Appl. Phys. Lett. **88**, 263117 (2006).
9. C. J. Pan, K. F. Lin, W. T. Hsu, and W. F. Hsieh, J. Appl. Phys. **102**, 123504 (2007).
10. C. J. Pan, K. F. Lin, and W. F. Hsieh, Appl. Phys. Lett. **91**, 111907 (2007).
11. Z. W. Pan, Z. R. Dai, and Z. L. Wang, Science **291**, 1947 (2001).
12. M. H. Huang, S. Mao, H. Feick, H. Yan, Y. Wu, H. Kind, E. Weber, R. Russo, and P. Yang, Science **292**, 1897 (2001).

13. H. C. Hsu, C. Y. Wu, and W. F. Hsieh, *J. Appl. Phys.* **97**, 064315 (2006).
14. J. H. Lim, C. K. Kang, K. K. Kim, I. K. Park, D. K. Hwang, and S. J. Park, *Adv. Mater.* **18**, 2720 (2006).
15. J. Y. Bae, J. Yoo, and G. C. Yi, *Appl. Phys. Lett.* **89**, 173114 (2006).
16. M. S. Gudiksen, J. Wang, C. M. Lieber, *J. Phys. Chem. B* **106**, 4036 (2002).
17. K. F. Lin, H. M. Cheng, H. C. Hsu, L. J. Lin, and W. F. Hsieh, *Chem. Phys. Lett.* **409**, 208 (2005).
18. A. V. Maslov and C. Z. Ning, *Phys. Rev. B* **72**, 125319 (2005).
19. W. T. Hsu, K. F. Lin, and W. F. Hsieh, *Appl. Phys. Lett.* **91**, 181913 (2007).
20. I. Shalish, H. Temkin, and V. Narayanamurti, *Phys. Rev. B* **69**, 245401 (2004).
21. N. Pan, X. Wang, M. Li, F. Li, and J. G. Hou, *J. Phys. Chem. C* **111**, 17265 (2007).
22. A. Kobayashi, O. F. Sankey, S. M. Volz, and J. D. Dow, *Phys. Rev. B* **28**, 935 (1983).
23. D. W. Jenkins and J. D. Dow, *Phys. Rev. B* **39**, 3317 (1989).
24. K. F. Lin, C. J. Pan, and W. F. Hsieh, *Appl. Phys. A* (submitted).
25. D. H. Lee and J. D. Joannopoulos, *Phys. Rev. B* **23**, 4988 (1981).
26. N. Malkova and C. Z. Ning, *Phys. Rev. B* **74**, 155308 (2006).
27. G. Kresse, O. Dulub, and U. Diebold, *Phys. Rev. B* **68**, 245409 (2003).
28. A. Many, Y. Goldstein, and N. B. Grover, *Semiconductor Surfaces* (North-Holland,

Amsterdam, 1965).

29. G. Allan and C. Delerue, Phys. Rev. B **70**, 245321 (2004).

30. K. Leung, S. Pokrant, and K. B. Whaley, Phys. Rev. B **57**, 12291 (1998).

31. S. Schulz and G. Czycholl, Phys. Rev. B. **72**, 165317 (2005).

32. S. Schulz, S. Schumacher, and G. Czycholl, Phys. Rev. B. **73**, 245327 (2006).

33. D. W. Jenkins and J. D. Dow, Phys. Rev. B **39**, 3317 (1989).



Chapter 8 Conclusions and Prospective

8.1 Conclusions

ZnO QDs were synthesized successfully via a simple sol-gel method. The average size of QDs can be tailored using well-controlled concentration of zinc precursor. The size of QDs was estimated by X-ray diffraction consistent with the results of high-resolution transmission electron microscope (HRTEM) image. Furthermore, the measured Raman spectral shift and asymmetry for the E_2 (high) mode caused by localization of optical phonons agree well with that calculated by using the modified spatial correlation model. From the resonant Raman scattering, the coupling strength between electron and longitudinal optical phonon, deduced from the ratio of the second- to the first-order Raman scattering intensity, diminishes with reducing the ZnO QD diameter. The size dependence of electron-phonon coupling is principally a result of the Fröhlich interaction.

We also analyzed the exciton's behavior in ZnO QDs. Size-dependent blue shifts of PL and absorption spectra revealed the quantum confinement effect. The band gap enlargement is in agreement with the theoretical calculation based on the effective mass model. Moreover, the exciton longitudinal-optical-phonon (LO-phonon) interaction was observed to decrease with reducing ZnO particle size to its exciton Bohr radius (a_B).

The unapparent LO-phonon replicas of free exciton (FX) emission and the smaller FX energy difference between 13 and 300 K reveal decreasing weighting of exciton-LO phonon coupling strength. The diminished Fröhlich interaction mainly results from the reducing a_B with size due to the quantum confinement effect that makes the exciton less polar.

In theoretical study, we first calculated the electronic structure and the density of states in the wurtzite structure of $Zn_{1-x}Mg_xO$ (ZMO) alloys using sp^3 semi-empirical tight-binding model, we observed increases of both band gap and electron effective mass that agree with the experimental results as increasing Mg composition up to $x = 0.3$. From the calculated total density of states, the increasing electron effective mass is a result of less orbital overlap of cation sites due to extra density of modes coming from Mg3s and Mg3p orbitals as introducing more Mg composition. Additionally, reducing electronegative characteristic of oxygen was caused by the O2p was less localized around the oxygen atom. In additionally, we theoretically studied the surface states in wurtzite semiconductor nanowires with identical lateral facets. Using the transfer-matrix technique, we first calculated the surface states for surfaces [0001] and [1-100] of the semi-infinite wurtzite semiconductor. We then used the cyclic boundary condition for the surface wave function in order to find the quantized spectrum for a nanowire.

Electronic band structures and surface states were investigated for ZnO finite wells or slabs grown along $\langle 0001 \rangle$ and $\langle 1-100 \rangle$ directions using tight binding representation. The dangling bonds on two end-surfaces caused surface bands for different directions grown slabs, of which the wavefunctions tend to localize at the end surfaces. The increasing splitting of the degenerate surface bands at the Γ point was observed decreasing with the thickness of the nonpolar $[1-100]$ slab. And, the quantum confinement effect is distinctively enhanced by the extra electron-field induced in the $\langle 0001 \rangle$ grown finite well with the polar end-surfaces.

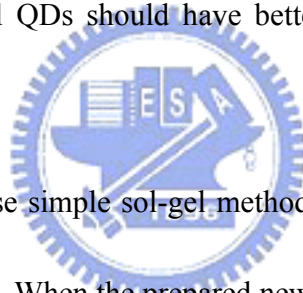


8.2 Prospective

In the next-generation optoelectronic devices, the nanometer-scale materials promise to be important due to numerous unique properties expected in the low-dimensional system. Low-dimensional ZnO nanostructures, such as QDs, nanoparticles (NPs), nanobelts, nanowires, and quantum wells, have been widely investigated for the feasible requirement. In particular, ZnO QDs and NPs are of great interest because of the three-dimensional confinement of carrier and phonon leads not only continuous tuning of the optoelectronic properties but also improvement in device performance. Nevertheless, the surface of QDs is usually composed of uncoordinated

atoms, which make the QDs highly active and quench the PL emission. Since, the modification of surface of ZnO QDs becomes imperative issue for next generation of optoelectronic devices.

In experiment, in order to combine the advantages of QDs and Mg-doped ZnO, ZnO-MgO core-shell structure is the most interesting topic for our works. That can overcome the effect of surface defects in ZnO, especially in QDs system which has large surface-volume ratio. Because the band gap energy of MgO is much larger than that of ZnO, the ZnO-MgO core shell QDs should have better emission efficiency than ZnO QDs.



We will suggest to also use simple sol-gel method to add $\text{Mg}(\text{OAc})_2 \cdot 4\text{H}_2\text{O}$ in ZnO QDs solution then stir at 40°C . When the prepared new solution drops on Si then take to be annealed for 300°C to 700°C . The primary results of the low temperature PL spectra of samples annealed at various temperatures that we observed a broaden emission from MgZnO alloy and two sharp emission from ZnO. We also found that the defect emission has been diminished from sample 300°C to 700°C . To further investigate more characteristic of ZnO-MgO core-shell QDs, the temperature dependent PL and time-resolved PL should proceed.

In other way, according to above experiment data, the effective-mass approximation

apparently gives a good understanding of the blue shift of the optical absorption threshold. However, this approach fails for the smallest crystallite sizes because of the oversimplified description of the crystal potential as a spherical well of infinite depth. A better description of the band structure can be obtained from a tight-binding (TB) framework. Since the atomic structure is implicitly considered, this method is more adequate for small crystallites. In the future, I will calculate the electronic structure and optical properties of ZnO QDs using TB approximation. Once the tight-binding parameters are known, we can calculate the eigenvalues of Hamiltonian H . This matrix is formed by 4×4 block matrices describing the interactions on the same atom (intra-atomic) or between two first-nearest neighbors (interatomic). If N is the number of atoms in the crystallite, the dimension of H is $4N$ and a direct diagonalization becomes impossible for several hundred atoms. To circumvent this problem we will use the recursion method or symmetry basis method. Such large matrices can be diagonalized with the help of group theory; partial diagonalization is effected by using the projection operators of the point group to form-basis states. Thus, computation time is reduced based on symmetry-TB method.

林國峰簡歷 (Vita)

基本資料

姓名：林 國 峰 (Kuo-Feng Lin)

性別：男

出生年月日：1977 年 10 月 18 日

籍貫：花蓮縣

永久通訊處：花蓮縣豐濱鄉大港口村 9 鄰 50 號

Email: xial17.eo92g@nctu.edu.tw

xial17.eo94g@nctu.edu.tw

學歷：

2001.9 - 2003.6 國立台北科技大學光電科技系 學士

2003.9 - 2005.6 國立交通大學光電工程研究所 碩士

2005.9 - 2008.10 國立交通大學光電工程研究所 博士

博士論文題目：

實驗及理論探討奈米結構之氧化鋅光學性質研究

Experimental and theoretical study on the influence of
finite crystallize optical properties in ZnO
nanostructures

Publication list

I. Refereed Journal Publications:

1. **Kuo-Feng Lin**, Hsin-Ming Cheng, Hsu-Cheng Hsu, Li-Jiaun Lin, Wen-Feng Hsieh, “*Band gap variation of size-controlled ZnO quantum dots synthesized by sol–gel method*,” Chemical Physics Letters 409, 208 (2005).
2. Hsin-Ming Cheng, **Kuo-Feng Lin**, Hsu-Cheng Hsu, Chih-Jen Lin, Li-Jiaun Lin, and Wen-Feng Hsieh, “*Enhanced Resonant Raman Scattering and Electron-Phonon Coupling from Self-Assembled Secondary ZnO Nanoparticles*,” Journal of Physical Chemistry B 109, 18385 (2005).
3. **Kuo-Feng Lin**, Hsin-Ming Cheng, Hsu-Cheng Hsu, and Wen-Feng Hsieh, “*Band gap engineering and spatial confinement of optical phonon in ZnO quantum dots*,” Appl. Phys. Lett. 88, 263117 (2006).
4. Hsin-Ming Cheng, **Kuo-Feng Lin**, Hsu-Cheng Hsu, and Wen-Feng Hsieh, “*Size dependence of photoluminescence and resonant Raman scattering from ZnO quantum dots*,” Appl. Phys. Lett. 88, 261909 (2006).
5. Ching-Ju Pan, **Kuo-Feng Lin**, Wei-Tse Hsu and Wen-Feng Hsieh, “*Raman study on alloy potential fluctuations in $Mg_xZn_{1-x}O$ nanopowders*,” J. Phys.: Condens. Matter 19, 186201 (2007).
6. Ching-Ju Pan, **Kuo-Feng Lin** and Wen-Feng Hsieh, “*Acoustic and optical phonon assisted formation of biexcitons*,” Appl. Phys. Lett. 91, 111907 (2007).
7. Ching-Ju Pan, **Kuo-Feng Lin**, Wei-Tse Hsu and Wen-Feng Hsieh, “*Reducing exciton-LO phonon coupling with increasing Mg incorporation in $MgZnO$ powders*,” J. Appl. Phys. 102, 123504 (2007).
8. Wei-Tse Hsu, **Kuo-Feng Lin**, and Wen-Feng Hsieh, “*Reducing exciton-longitudinal-optical phonon interaction with shrinking ZnO quantum dots*,” Appl. Phys. Lett. 91, 181913 (2007).
9. S. C. Ray, Y. Low, H. M. Tsai, C. W. Pao, J. W. Chiou, S. C. Yang, F. Z. Chien and W. F. Pong, **K. F. Lin**, H. M. Cheng and W. F. Hsieh, “*Size dependence of the electronic structures and electron-phonon coupling in ZnO quantum dots*,” Appl. Phys. Lett. 91, 262101 (2007).
10. **Kuo-Feng Lin**, Ching-Ju Pan, and Wen-Feng Hsieh, “*Calculations of electronic structure and density of states in the wurtzite structure of $Zn_{1-x}Mg_xO$ alloys using sp^3 semi-empirical tight-binding model*,” Appl. Phys. A. (2008).
11. **Kuo-Feng Lin** and Wen-Feng Hsieh, “*Electronic band structures and surface states of ZnO finite well structures*,” J. Phys. D: Appl. Phys. 41, 215307 (2008).

II. Conference:

1. Kuo-Feng Lin, Hsu-Cheng Hsu, Hsin-Ming Cheng, and Wen-Feng Hsieh, ***“Influence of crystal size on the photoluminescence of ZnO quantum dots grown by sol-gel technique,”*** 2004 OPT 光電年會.
2. Ming-Rung Tsai, Kuo-Feng Lin, Hsu-Cheng Hsu, Hsin-Ming Cheng (and Wen-Feng Hsieh), ***“以溶膠凝膠法製備MgxZn1-xO粉末之發光特性研究”*** 2004 OPT 光電年會.
3. Yi-Ching Lin, Kuo-Feng Lin, Chun-Yi Wu, Song Yang, Hsu-Cheng Hsu, and Wen-Feng Hsieh, ***“Nanowire-based dye-sensitized solar cell with ZNO nanowires manufactured by thermal vapor deposition,”*** 2005 OPT 光電年會.
4. W. F. Hsieh, H. M. Cheng, K. F. Lin, and H. C. Hsu, ***“Size Dependence of Band Gap Variation and Electron-phonon Coupling in ZnO Quantum Dots,”*** IQEC/CLEO-PR, Tokyo, Japan, 2005/11/07.
5. Wen-Feng Hsieh, Kuo-Feng Lin, Hsin-Ming Cheng, and Hsu-Cheng Hsu, ***“Spatial confinement of optical phonon in ZnO quantum dots,”*** Materials Research Society 2006 Spring Meeting, San Francisco, Ca., USA.
6. Wen-Feng Hsieh, Wei-Tse Hsu and Kuo-Feng Lin, ***“Reducing exciton-LO phonon interaction with shrinking ZnO quantum dots,”*** IEEE-LEOS 2008 Winter Meeting, Sorrento, Italy.
7. Kuo-Feng Lin, Ching-Ju Pan, and Wen-Feng Hsieh, ***“Electronic structure and surface states in the wurtzite structure of ZnO system using sp^3 semi-empirical tight-binding model,”*** Materials Research Society 2008, Chongqing, China.